Master's Thesis – Master Energy Science

Designing a Safe and Optimal Heat Storage System in Salt Caverns for Maximum Thermal Efficiency and Heat Output

Authors
Mohamad Alameh – 0546070 - m.alameh@students.uu.nl

University Supervisor : Dr. Wen Liu

Company Supervisor: Dorien Dinkelman

Utrecht University

Energy Science
Faculty of Geosciences

16th of august 2024

Contents

Abstract

This thesis addresses the central research question: "How can operational and structural parameters be optimized within salt caverns to enhance thermal efficiency and safety for heat storage?" Focusing on the Twente region, this study employs COMSOL Multiphysics and DIANA FEA software for a comprehensive analysis. COMSOL is used to evaluate the influence of operational parameters such as temperature differentials (ΔT), initial temperatures, and the impact of cavern shape and aspect ratios on the thermal performance and efficiency of salt caverns used for energy storage. DIANA FEA conducts geomechanical analyses to assess the structural safety and stability of these caverns.

Simulation results from COMSOL indicate that higher ΔTs and initial temperatures enhance rapid heat absorption, which may lead to quicker energy depletion, suggesting a balance is crucial between heat retention and extraction. Adjustments in cavern shape and aspect ratios were found to significantly influence thermal efficiency, highlighting the potential for geometric optimization in storage effectiveness.

The geomechanical analysis via DIANA FEA provides essential insights into managing subsidence and internal pressures, critical for ensuring the structural safety of these storage systems. This contributes to advancing theoretical knowledge and offering practical strategies for efficient and safe thermal energy storage implementations .

Given the scarcity of research on utilizing salt caverns for thermal energy storage, this study not only fills a significant gap in the literature but also demonstrates the potential for further detailed investigation. The findings suggest promising avenues for enhancing the efficiency and safety of these storage systems, thereby contributing to the diversification and sustainability of energy storage solution.

1. Introduction

1.1. Societal background

The world's goal for a sustainable future relies on the global energy sector's capacity to reach net zero CO_2 emissions by 2050, as specified in the Net Zero Emissions by 2050 Scenario (NZE Scenario). This ambitious pathway aims to limit global temperature rise to 1.5 °C, with advanced economies spearheading the transition (Energy Agency, 2021). As of 2022, global heat consumption reached 220,000 PJ, with modern renewables contributing 11.6% to the heat supply. In the European Union, heat consumption was 21,500 PJ, with modern renewables accounting for a more significant share of 23.2% (IEA, 2022). Notably, the heating and cooling sector constitutes half of Europe's energy consumption, underscoring the urgent need for innovative energy solutions.

Achieving the 2030 climate targets necessitates a substantial increase in sustainability measures. This project aims to reduce CO_2 emissions in the built environment by 3.4 million tons by 2030, relative to baseline scenarios (Hague, 2019). In the Netherlands, the built environment contributed 13% of total greenhouse gas emissions in 2020, with natural gas accounting for 71% of domestic heating (CBS, 2022). Given the Dutch government's target of net zero greenhouse gas emissions by 2050, it is crucial to explore sustainable energy alternatives, such as subsurface heat storage.

Underground Thermal Energy Storage (UTES) technologies, including aquifer thermal energy storage (ATES), borehole thermal energy storage (BTES), and pit thermal energy storage (PTES), are pivotal in managing seasonal heat demand variations (Erik Nielsen *et al.*, n.d.). Implementing these low-carbon systems in buildings requires tailored approaches considering local climates, existing structures, and available heating supplies (OECD, 2023). Consequently, local governments play a crucial and active role in driving this energy transition, as demonstrated by the Dutch Climate Agreement 2019, which mandated each municipality to develop and submit a Heat Transition Vision detailing their approach to achieving gas-free and sustainable heating systems (RVO, 2019).

In the eastern and south-eastern regions of the Netherlands, implementing an ATES system encounters difficulties because of the limited availability of appropriate aquifers, (Dinkelman *et al.*, 2020). As a result, alternative storage methods must be explored.

Ennatuurlijk, a Dutch energy company specializing in sustainable heating and cooling solutions, manages multiple district heating networks in the Twente region. They proposed utilizing salt caverns for thermal energy storage, leveraging their potential and abundance in the eastern Netherlands.

Rock salt, a type of sedimentary rock, has unique properties due to its deposition and mineral composition. Unlike most sedimentary rocks, it exhibits visco-elasto-plastic behavior, allowing it to creep under constant load rather than breaking abruptly. While brittle rocks deform minimally until failure, rock salt deforms progressively under increasing stress without fracturing. It has very low porosity (0.1 to 1%), permeability (0.0001 to 0.01 millidarcy), and a consistent density of around 2.2 x 10^3 kg/m^3, unaffected by depth. Rock salt's thermal conductivity, the highest among sedimentary rocks, decreases with temperature, from 4 W/m·K at 70 °C to 2 W/m·K at 300°C (Forbes Inskip & Ougier-Simonin, 2021).

Due to rock salt's abundance and favorable petrophysical properties, utilizing salt caverns for thermal energy storage is a promising idea worth investigating further. Therefore, Ennatuurlijk seeks to investigate thermal energy storage's technical and economic feasibility in salt caverns. This research is a part of the WarmingUP GOO project, funded by MOOI (Missiegedreven Onderzoek, Ontwikkeling en Innovatie) for the built environment. This study aims to significantly contribute to the broader goal of sustainable energy transition and meeting ambitious climate objectives by addressing these challenges.

1.2 Scientific relevance and research problem

The current academic research on the utilization of salt caverns for heat storage is notably sparse, with an almost complete absence of comprehensive literature on the subject. Only two reports have been identified that discuss heat storage in salt caverns: one from 1980 by Collins(Collins et al., 1978) and another from 2019 by Ekwadraat. Collins' study demonstrates the technical and economic feasibility of using salt caverns for high-temperature underground thermal energy storage, focusing on a system that uses hot oil in gravel-filled caverns within salt domes.

The more recent study by Ekwadraat examines the reuse of underground caverns for heat production and storage, providing valuable insights but leaving several critical areas unexplored. Ekwadraat's approach to determining the time-dependent warming within the caverns involves a conceptual model that calculates heat conduction in a spherical hollow space filled with brine encased in rock salt with specific dimensions and thermal properties. While this model offers a foundational understanding, it might only partially assess the caverns' heat storage capabilities. Notably, the study lacks an investigation into thermocline stability, a crucial factor for maintaining efficient heat storage. The absence of this consideration raises questions about potential temperature distribution and stratification during production and injection phases, which are vital for the efficient operation of such storage systems.

This research aims to fill these significant gaps by focusing on the optimal development of salt caverns for heat storage, using the Twente region as a case study. The existing studies provide a general overview and feasibility analysis but lack a detailed examination of a specific geographical location. By focusing on Twente case study, we can account for local geological and environmental conditions, significantly affecting the design and performance of the heat storage system. This localized approach provides a tailored solution that considers local geological formations, thereby improving the applicability and accuracy of the design for the Twente region. While previous studies discuss general feasibility and some design aspects, they do not comprehensively identify and analyze the specific design and operational parameters that influence thermal efficiency. This study will identify key factors like cavern geometry, heat transfer fluid properties, insulation methods, and injection/retrieval cycles, offering a detailed

analysis of their influence on thermal efficiency to guide the development of more optimized designs.

The existing research provides some insights into thermal losses but lacks a systematic approach to quantifying the overall thermal efficiency of the storage system. Developing a methodology to determine thermal efficiency quantitatively allows for a more precise assessment of system performance, enabling better design and operational adjustments to enhance efficiency. Additionally, there is a need for a detailed study on how varying different parameters can impact thermal efficiency and the extent of this influence. The contribution of this research will be the quantification of the sensitivity of thermal efficiency to changes in key parameters, offering valuable insights for optimizing system design and operations. The previous studies briefly touch upon cavern stability but lack an in-depth analysis of the geomechanical aspects and safe operating temperature limits. By establishing temperature limits for safe operation from a geomechanical perspective, it ensures that the long-term stability and safety of the storage system, addressing a critical aspect of practical implementation. Finally, the prior work does not integrate all aspects—design, operation, thermal efficiency, and geo-mechanical stability—into a cohesive optimization framework. This research aims to develop a comprehensive design strategy that optimizes thermal efficiency while ensuring geo-mechanical safety, offering a robust and practical solution for high-temperature heat storage in salt caverns. This comprehensive approach not only advances scientific knowledge but also offers practical solutions for optimizing high-temperature heat storage in salt caverns, thereby significantly contributing to the field.

On a social or practical level, this research offers the tools needed to make the heating sector more sustainable. It provides a binding approach for decarbonizing the heating sector. The step-by-step methodology makes this research practical and widely applicable. As a result, it could also be applied to other cities or geographical levels (e.g., national or European). At a scientific level, this research is relevant because it contributes to the knowledge about the heat transition from a system analysis perspective and provides a starting point for determining the feasibility of utilizing salt caverns for heat storage purposes. Even though this study focuses on the thermal and geo-mechanical feasibility, it will still be a foundation for further research, advancing both scientific understanding and practical applications in the field of sustainable energy storage.

1.3 Research questions

The primary objective of this research is to develop an optimal heat storage system within salt caverns, using the Twente region as a case study. The main research question guiding this study is: How can a heat storage system be designed within a salt cavern to achieve optimal thermal efficiency and heat output?

To effectively address the main question, it is necessary to break it down into the following sub-questions:

1. **Which design and operational parameters most significantly influence thermal efficiency?**
    - Identifying key parameters is essential to focus on the factors that most impact system performance, aiding in targeted optimization efforts.
2. **How can the thermal efficiency of the heat storage system be accurately determined?**
    - Developing accurate methods for measuring thermal efficiency ensures precise performance evaluation and validation of the system's effectiveness.
3. **To what extent do the selected parameters impact thermal efficiency?**
    - Quantifying the influence of different parameters allows for informed design improvements and prioritization of changes that yield significant efficiency gains.
4. **What are the safe operating temperature limits from a geo-mechanical perspective?**
    - Establishing safe operating limits ensures the long-term stability and safety of the storage system, addressing critical aspects of practical implementation.

These sub-questions systematically address the components needed to design an efficient and stable heat storage system in salt caverns. By identifying influential parameters, developing accurate measurement methods, quantifying parameter impacts, and ensuring geo-mechanical safety, this research provides a comprehensive solution tailored to the geological conditions of Twente

1.4 Research scope

The Temporal frame of this study will be 30 years for the utilization of the salt cavern for heat storage. Moreover, the reference for that was based on hydrogen storage in salt caverns(TNO, 2021). However, for the geo-mechanical modeling the temporal scope is measured for 40 years. The geographical scope would be Twente Netherlands and it would be discussed in greater details in **Section** 2.1

2. Twente use case

The region of Twente, in the Province of Overijssel, is located on the eastern border with Germany and is part of the Euregio, a transregional cooperation between bordering areas in Germany and the Netherlands. The size of Twente is 143,000 hectares; there are about 600,000 inhabitants who live in 14 municipalities; half of them live in one of the three cities: Enschede, Hengelo, or Almelo (*Twente*, n.d.).

The Twente region in the Province of Overijssel, Netherlands, serves as an exemplary case study for investigating the feasibility of thermal energy storage in salt caverns due to its unique geological setting, ongoing cavern development, and significant energy consumption. This section covers the geological setting, detailing formations like the Röt Formation crucial for salt mining (**Chapter** 2.1). It explores the historical and technological advancements in cavern development (**Chapter** 2.2). Additionally, it includes analysis of well data, providing a clear stratigraphic framework for accurate modeling (**Chapter** 2.3).

2.1 Geological Setting

The subsurface geological structure in Eastern Twente comprises several distinct formations, including the Solling Formation, Röt Formation, Muschelkalk Formation, Altena Group, Niedersachsen Group, and the North Sea Supergroup. The Röt formation, where the salt deposits are located, comprises layers A through D. Layer A stands out as the thickest and purest, while layers B, C, and D contain interspersed rock layers, as shown in **Figure** 1. Predominantly, layers A and B are thoroughly mined, with only a portion of layer C being utilized, ensuring the caverns' stability. The region is notably free of significant fault zones, facilitating the development of stable caverns. Contrasting with the northern Netherlands, where salt is extracted from dome-shaped structures several hundred meters tall but narrow in diameter, the Röt formation features a flat stratigraphy. The resulting caverns are flat, with a modest height of around 20 meters, depending on the location and salt layer thickness. However, they can extend up to 130 meters in diameter (Mollema, 2011).

Salt production in Twente is not a new practice, and it began in 1886 after unintentionally discovering a salt deposit during a well drilling for fresh water, which unexpectedly produced saltwater. Further explorations in 1909 revealed Zechstein Salt in Winterswijk and Rötsalt in Boekelo. By 1918, post-World War I, the Royal Dutch Salt Industry

(KNZ) started extracting salt in Boekelo, initially from 325 meters deep. Later 1933, operations were moved to Hengelo, taking advantage of its closeness to the Twente Canal.

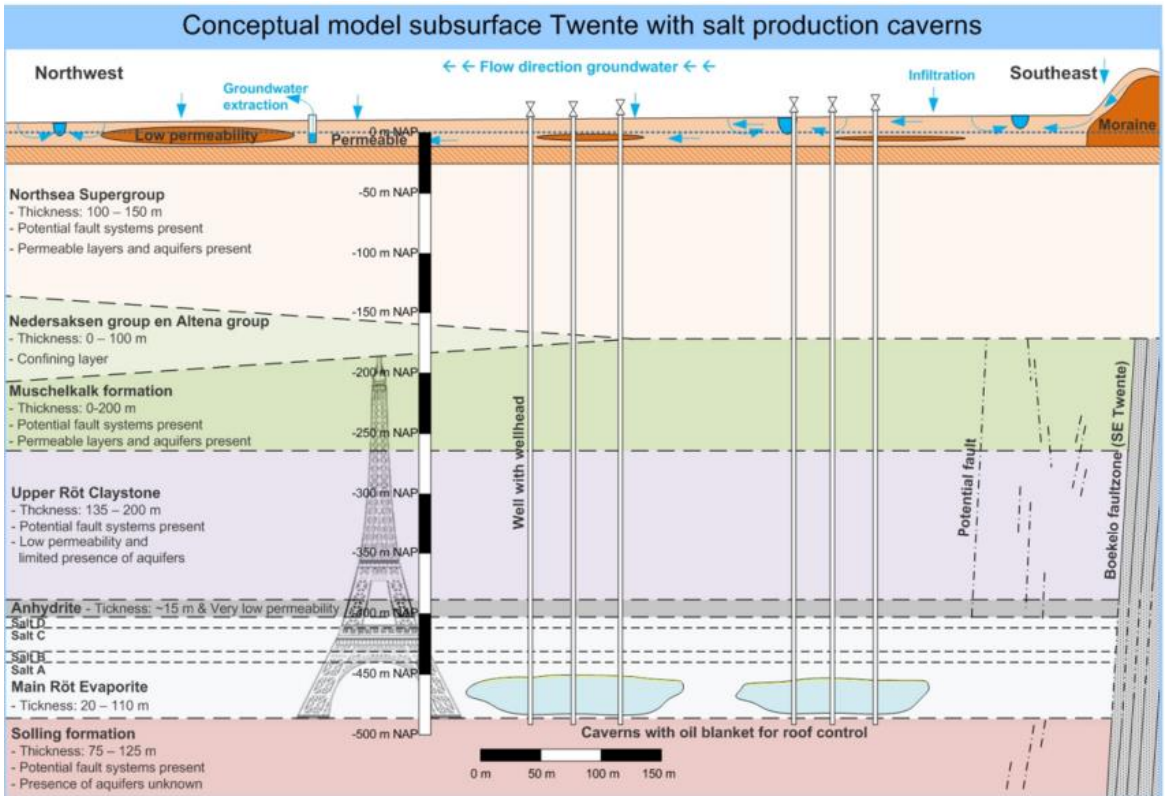

Figure 1: Conceptual model of Twente's subsurface in the context of salt cavern production highlighting the different formation (Mollema, 2011).

Over time, salt extraction methods in Twente have significantly progressed, shifting from the conventional three-well setup to the innovative Single Cavern Completion (SCC) system in 2006. This modern system, facilitating injection and production via a single well, marked a substantial efficiency improvement. Salt extraction predominantly occurs in the Röt formation, explicitly targeting the A and B layers, which are known for their optimal thickness and purity and are essential for maintaining the structural integrity of the caverns.

Table 1 summarizes key details from some of the wells used for cavern production includes well names, end-date of drilling, total vertical depth (TVD), depths and thicknesses of the Main Röt Evaporite Member, and the formations above and below the Main Röt Evaporite Member. This data helps establish a general understanding of the depth and thickness of the relevant geological formations in Twente. The well data indicates that the Röt Claystone Formation extends from the surface down to where the Röt Evaporite Formation begins. For example, the Röt Evaporite starts at 389m in Well TWR-487, 404m in Well TWR-504, 394m in Well TWR-360, 351m in Well TWR-238, 467m and 525m in Well TWR-348/447, and 462m in Well TWR-541. From these observations, we can generalize that the Röt Claystone

Formation extends down to an average depth of approximately 350 meters, considering the variations and the onset of the Röt Evaporite Formation. The thickness of the Röt Evaporite Formation is directly provided in the well data, showing thicknesses of 82m in Well TWR-487, 81m in Well TWR-504, 69m in Well TWR-360, 78m in Well TWR-238, 23m and 82m in Well TWR-348/447, and 82m in Well TWR-541. Thus, we can generalize that the Röt Evaporite Formation spans from 350 meters to approximately 450 meters, with an average thickness of around 80 meters. The Soling Claystone Formation lies below the Röt Evaporite Formation and extends further down. The wells consistently report the presence of the Soling Claystone Formation below the Röt Evaporite Formation, with specific starting depths varying slightly but all below 450 meters. Therefore, we can generalize that the Soling Claystone Formation extends from around 450 meters to a depth of approximately 800 meters. These generalizations provide a clear stratigraphic framework that will be used as inputs in the modeling methodology, ensuring accurate representation of the subsurface conditions in Twente. This coincides with the conceptual model shown in the figure, which illustrates the subsurface geological structure in Eastern Twente, highlighting the various formations and their respective thicknesses and depths, further validating the derived generalizations.

Table 1: Overview of some wells used for cavern production and their corresponding information(NLOG, n.d.).

Well name	**End-Date drilling (DD-MM-YY)**	**TVD [m]**	**Main Röt Evaporite Member [m]**	**Main Röt Evaporite Member (Thickness in [m])**	**Above Main Röt Evaporite Member**	**Below Main Röt Evaporite Member**
TWR-487	29-11-07	472.0	389-471	82	Intermediate Röt Claystone Member (27 m)	Soling Claystone Formation
TWR-504	02-02-10	486.5	404-485	81	Intermediate Röt Claystone Member (26.5 m)	Soling Claystone Formation
TWR-360	14-09-89	463.5	394-463	69	Röt Claystone Member (167 m)	Soling Claystone Formation
TWR-238	01-01-73	431.5	351-429	78	Soling Claystone Member (159 m)	Soling Claystone Member
TWR-348	22-12-89	558.0	525-548	23	Röt Claystone Member (221 m)	Soling Claystone Member
TWR-447	19-05-06	550.0	467-549	82	Röt Claystone Member (155 m)	Soling Claystone Member
TWR-541	19-07-2017		462-544	82	Röt Claystone Member (136 m)	Soling Claystone Member

2.2 Cavern development

Since the 1930s, the development of caverns in the Hengelo brine field has evolved due to advancements in leaching processes and technology. The different cavern types are illustrated in **Figure** 2, where initially, caverns, categorized as Single Completion Caverns (SCCs), were developed with a single well, reaching the top of the salt deposit and laterally expanding, forming hydraulic connections between neighboring caverns. In the 1960s and 1970s, Multi Completion Caverns (MCCs) were introduced, where multiple wells per cavern were drilled to enhance recovery by efficiently mining the salt between wells, particularly with blanket oil. The transition from category 2 to 3 introduced safety measures like a 5-meter safety roof and "inherently safe" caverns to prevent significant subsidence and sinkholes. In the past decade, a single well has developed modern SCCs with a 5-meter safety roof and inherently safe concepts. This approach allows for better monitoring blanket oil levels, resulting in more effective cavern development than MCCs.

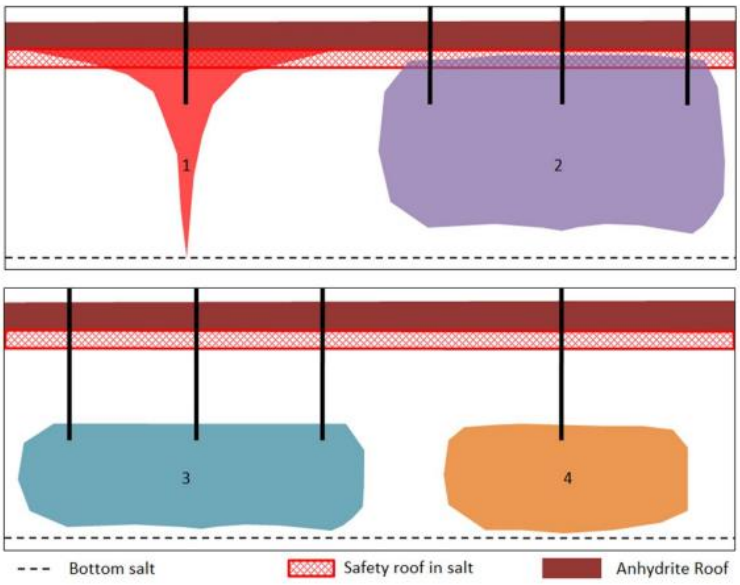

Figure 2: Classification of Cavern Types in the Hengelo Brine Field: (1) Initial Single Completion Caverns (SCCs), (2) Initial Multi Completion Caverns (MCCs), (3) Contemporary MCCs, (4) Contemporary SCCs.

Over time, newer caverns have been developed at increasing distances from the evaporation plant, as depicted in **Figure** 3, while the oldest caverns, highlighted in black, are located near the plant. Building on the geological setting and the development of caverns in the Twente region, it's crucial to understand the specific techniques used to construct salt caverns. These methods are essential for optimizing thermal energy storage in this unique geological context, as the shape of the caverns is significantly influenced by the construction method employed(Wan et al., 2020).

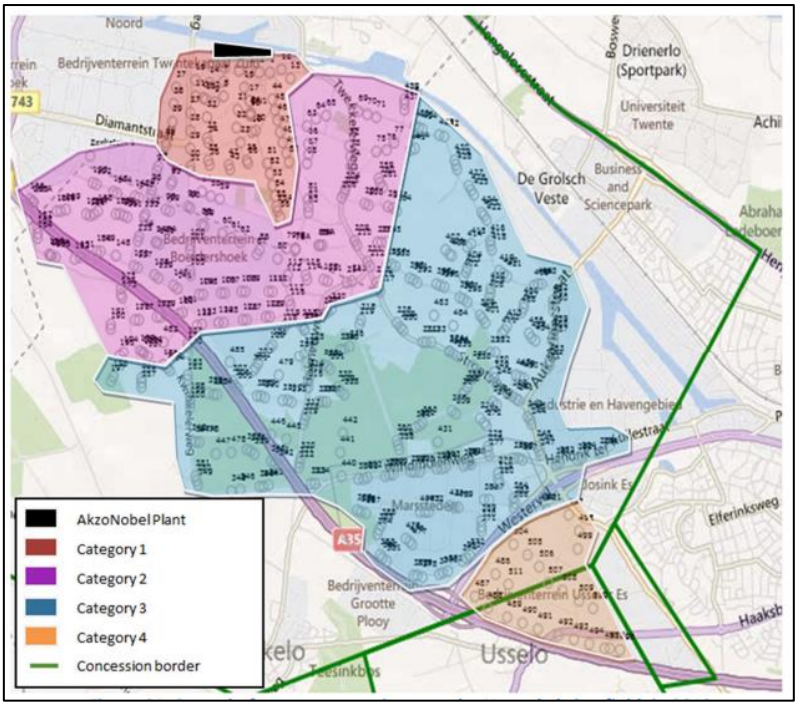

Figure 3: Distribution of Cavern Classifications Across the Hengelo Brine Field

Salt caverns can be constructed using one or more wells. Fresh water is injected into the rock salt formation to dissolve it, and brines are then pumped out, gradually developing a cavern. There are several methods of constructing salt caverns; however, the three most prevalent methods are the Single Well Blanket Method (SWOB), the Two Well Vertical (TWV) and the Two Well Horizontal (TWH).

1. Single Well Blanket Method (SWOB)

The single-well-oil-blanket (SWOB) method is considered as the conventional technique for constructing salt caverns. It is used to build single-well vertical (SWV) caverns in salt formations. This method has low construction efficiency and results in caverns with small usable volumes. In the SWOB method, water dissolves the salt, forming a cavern. This process can be implemented in two ways, as illustrated in **Figure** 4.

The **first** approach, Direct Brine Circulation, involves injecting water down through a central pipe and extracting the dissolved salt (brine) through the space between this pipe and the cavern wall. This typically results in a cylindrical cavern with a slightly bulging bottom part. The **second** approach, Reverse Circulation, introduces water into the cavern through the gap between the central pipe and the cavern wall while the brine is removed through the pipe. This method usually produces a wider cavern at the top and narrower at the bottom, resembling the shape of a morning glory flower. The choice between these two methods influences the leaching rate, which determines how quickly the salt is dissolved and the final shape of the cavern (Wan *et al.*, 2019).

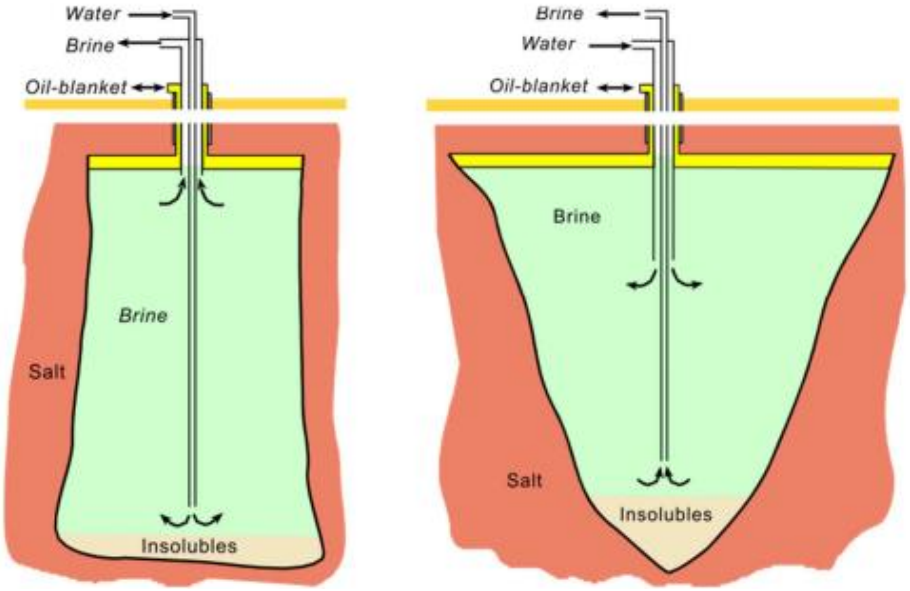

Figure 4: The two methods of applying the Single-Well-Oil-Blanket (SWOB) technique for creating storage caverns in salt deposits: Direct Brine Circulation and Reverse Circulation

2. Two Well Vertical (TWV) & Two Well Horizontal (TWH)

The Two Well Vertical (TWV) method involves constructing a cavern using two vertical wells spaced 15-30 meters or more apart (**Figure** 5a). Initially, two small caverns are created using the single-well-oil-blanket (SWOB) method until they connect automatically. Freshwater or unsaturated brine is injected through one well, while high-concentration brine is withdrawn from the other.

In contrast, the Two Well Horizontal (TWH) method employs a two-well system to develop a long, horizontal cavern (**Figure** 5b). The process begins with drilling vertical and horizontal wells into the salt formation, which are then secured with cemented casings and

equipped with inner tubing that reaches into the salt layer. These wells are connected underground using directional drilling techniques. Fresh water is pumped into the salt formation through the tubing in Well A, dissolving the salt and forming brine. The brine is then extracted through Well B. This process can be reversed, with water injected through Well B and brine removed from Well A. By alternating the injection and extraction between the two wells, a horizontal cavern is formed, ensuring a regular and controlled shape with a length greater than its height (Peng *et al.*, 2023).

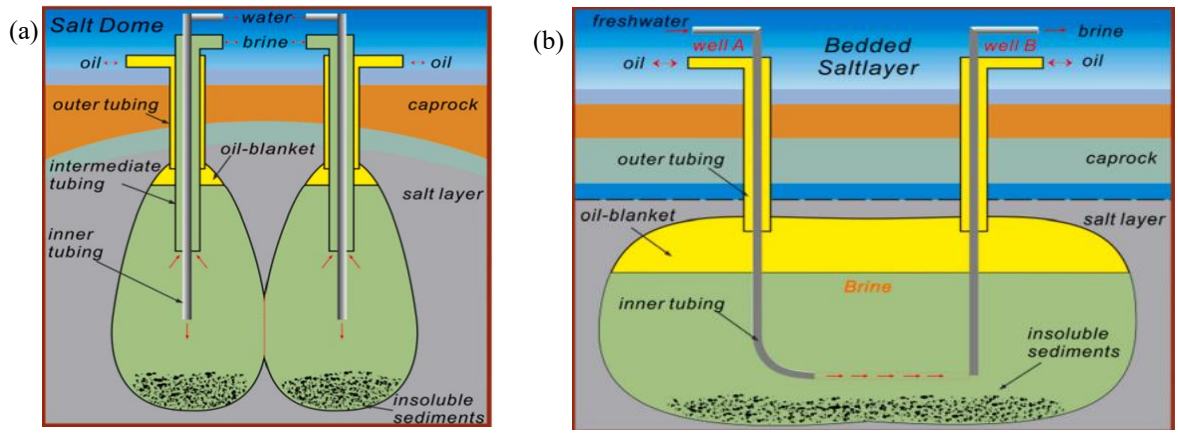

Figure 5: Schematic representation of cavern construction using (a) Two Well Vertical (TWV) and (b) Two Well Horizontal (TWH) methods, showcasing the vertical and horizontal drilling configurations employed in each technique

While the TWV method starts faster than the SWV method, their construction speeds eventually become the same as the process advances. The TWV method needs help shaping the cavern, particularly in thin salt layers with low purity, and it struggles to create large caverns. In both the SWV and TWV methods, the cavern's maximum width and height are significant factors limiting its size.

In contrast, the TWH method presents several advantages. It allows for faster construction due to a higher injection and withdrawal flow rate and greater efficiency. It can create larger caverns, making better use of the salt formations. Additionally, it offers superior control over the shape of the cavern, as wells can be drilled horizontally or at an angle, providing flexibility in design (Wan *et al.*, 2020).

2.3 District Heating Network

In the Twente case study, the primary heat sources for Hengelo and Enschede are the residual heat from Nobian and Twence, with Twence providing approximately 3600 TJ of high-temperature heat, complemented by Nobian's contribution of approximately 100 MWth of low-temperature heat (Regionaal Warmtenet Factsheet Regionaal Warmtenet, n.d.). Twence supplies more than 62,500 households and companies with high-temperature heat, eliminating the need to rely on natural gas for heating. The heat distribution network involves transporting hot water from Twence to Enschede through an underground heat pipeline, which then disperses to facilities like Grolsch and the Ennatuurlijk heat network. Additionally, Empyro supplies low-temperature heat to the Hengelo heat network via Nobian. Approximately 76% of households within the urban area rely on high-temperature heat, linking roughly 128,500 homes. However, not all will be connected to the regional heating network, with around 40% of households eligible for such connections. Looking ahead to 2030, the forecasted total heat consumption for the area is estimated to reach 17,481 TJ per year. It is projected that 60% will be supplied by the regional heating network, accounting for 10,488.6 TJ/year, while the remaining 40% will be sourced from alternative sources, totaling 6,992.4 TJ/year (*Generating and Supplying Heat*, n.d.). Moreover, the heat network in Enschede has been recognized as the most sustainable heat network in the Netherlands for several years, supplying more than 535,000 GJ of heat annually to over 9,000 households and 150 business customers across various districts and businesses (*Warmte Voor Enschede*, n.d.).

Ennatuurlijk operates the district heating network in both Henglo and Enschede, presented in **Figure** 6a, highlighting both the high and the medium temperature network. For a complete, rounded overview, a geographical overlap of salt caverns and the heating network in Twente is presented in **Figure** 6b, which enhances the region's capacity for sustainable energy practices, particularly in energy storage. The salt caverns, naturally suited for large-scale storage, complement the heating network by potentially providing an underground thermal energy storage solution, enabling efficient seasonal energy storage and retrieval. Such a synergy can optimize energy utilization, reduce carbon footprints, and support the region's transition towards renewable energy sources.

(a)

(b)

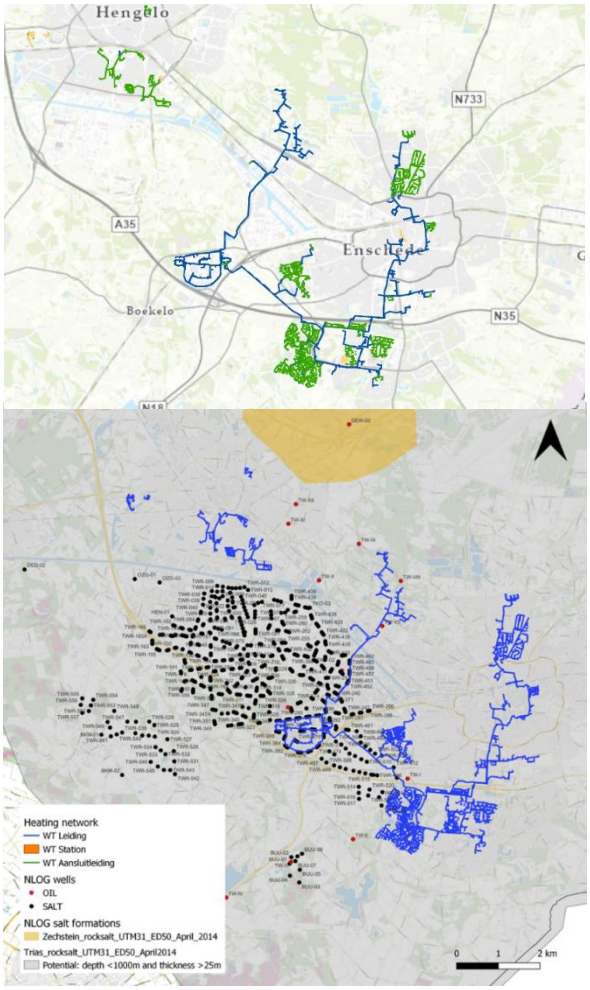

Figure 6: (a) District Heating Network in Twente where Blue represents Hight temp network and Green Medium Temperate Reproduced from reference Leiding_ENN_versie3 (arcgis.com) (b) The location of salt formation, caverns and heating network in Twente

3. Operational Mechanisms of Thermal Energy Storage

Following the geological context and the development of caverns explained in **Section** 2, this section provides a conceptual framework for utilizing salt caverns for heat storage. It details the processes involved in both the heating and utilization phases of thermal energy storage, as well as the annual cycle of charging, standby, and discharging.

To understand the utilization of salt caverns for heat storage, **Figure** 7 illustrates the process through two distinct phases: production and utilization. Initially, the cavern is filled with brine to maintain safe pressure levels. During the **production phase** (**Figure** 7a), brine is extracted from the outlet at the cavern's lower section. It then passes through a heat exchanger, which heats and reinjects it through the inlet at the upper part of the cavern. This method leverages the principle that colder water, being denser, naturally settles at the bottom while hotter water remains at the top.

In the **utilization phase** (**Figure** 7b), the heat stored in the cavern is extracted by producing brine from the outlet at the upper part. This hot brine undergoes heat extraction in the heat exchanger. The cooled brine, now depleted of heat, is reinjected through the inlet at the lower part of the cavern. By dynamically extracting cold brine from the bottom, injecting heated brine at the top during the production phase, and reversing this flow during the utilization phase, the system efficiently utilizes the natural stratification of temperatures within the cavern to store and retrieve heat.

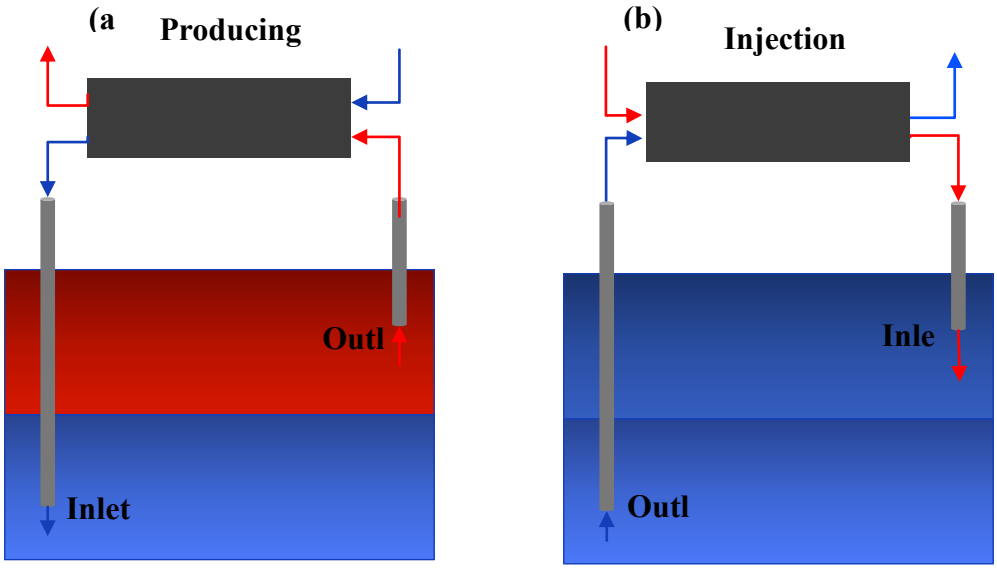

Figure 7: Illustration depicting the process of heat storage and extraction in salt caverns. The diagram outlines the steps involved. (a) represent the production (heat extraction) phase while (b) represent the utilization (heat storing) phase. Red represents the heated stream (arrows) and area (rectangles) of the cavern while blue represents cold stream and area of the cavern.

3.1 Annual Cycle of Charging, Standby, and Discharging for Thermal Energy Storage

Based on the analysis of heat demand depicted in **Figure** 8, which shows significant seasonal variations in space heating, cooling, and hot water demand, the annual operation of the thermal energy storage system is divided into phases to optimize efficiency. Although the optimal cycle for each phase would ideally be four months, for computational efficiency, a three-month cycle has been adopted.

From **Figure** 8, space heating demand is highest from January to April, declines from May, and reaches its lowest point from June to September before rising again in October. Cooling demand, conversely, peaks during the summer months from June to August. Hot water demand remains relatively constant throughout the year. Total heat demand reflects these seasonal variations, peaking during the winter months and dipping in the summer.

During the **charging phase**, which runs from May to July, hot fluid at 80 °C is injected into the storage system. This period is characterized by minimal demand for space heating and an increase in cooling demand. The surplus waste heat available from the Twence plant during the warmer months is utilized to store thermal energy for later use. This ensures sufficient energy is stored during the period of low heating demand.

Following the charging phase, the system enters the **standby rest period** from August to October. As the system transitions from the summer months of high cooling demand to the winter months of high heating demand, this phase allows the stored thermal energy to be maintained without significant losses. Despite relatively high cooling demand, the stored heat is not heavily utilized, stabilizing the system and preserving energy for the peak heating season.

The **discharging phase** occurs from November to January and February to April, corresponding to the high heat demand due to increased space heating needs. During this phase, the stored thermal energy is effectively released to meet heating requirements. The fluid, initially at 80 °C, is used for heating purposes and cools down to 40 °C by the end of the phase, indicating the utilization of the stored energy. This phase helps reduce reliance on conventional heating sources and enhances the overall efficiency of the thermal energy storage system.

In summary, although the optimal cycle for each phase would be four months to align perfectly with seasonal changes in heat demand, the phases have been adjusted to three months

for computational simplicity. Therefore, the annual operation is divided into **three-month cycles** of **charging** (May to July), **standby** rest (August to October), and **discharging** (November to January and February to April). This approach ensures efficient storage and utilization of thermal energy throughout the year, optimizing the system's performance in response to varying energy demands as illustrated in Graph X.

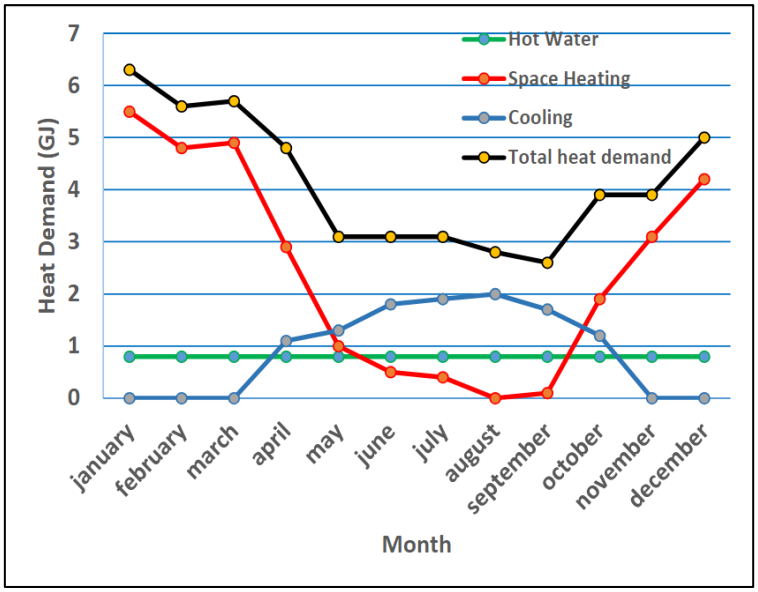

Figure 8: Monthly district heating heat demand in the Netherlands over the course of a year. (De Geus et al., 2015)

4. Theoretical

The chapter provides the theoretical framework for this research and will answer 2 out of the 5sub research question, SQ1 & SQ2. The answer of sub question 1 (SQ1) will provide the reasoning for the simulation tool selection (**Chapter** 4.1). Furthermore, **Chapter** 4.2 assists in the understanding of heat transfer theory that is crucial for answering SQ2 in **Chapter** 4.3. The later chapter is the thermal section which includes the review of thermal energy storage systems, key design and operational parameters, and the thermal dynamics in caverns, that will answer which design and operational parameters are most influential in determining the thermal efficiency of salt caverns. **Chapter** 4.4 gives insight on the theory of fluid dynamics inside the cavern while **Chapter** 4.5 provides evaluation metrics for the efficiency calculation. **Chapter** 4.6, is the geomechanical section focuses on the geomechanical properties and the selection criteria that the safety consideration will be based upon.

4.1 Simulation Tool

In selecting an appropriate simulation tool for modeling salt caverns as thermal storage systems, a comparative study of several fluid simulation software products was conducted. The analysis focused on three prominent fluid flow simulation modules: Ansys Fluent, OpenFOAM, and COMSOL Multiphysics.

Ansys Fluent is a well-established fluid modeling tool renowned for its robust capabilities in predicting fluid flow, heat and mass transfer, and related phenomena. As a component of the Ansys fluid simulation suite, Fluent is supported by additional tools such as the "CFD Premium Bundle," which includes Workbench, SpaceClaim (a pre-processing tool), CFX (another CFD solver), and CFD-Post (a post-processing tool). Fluent operates on both Windows and Linux systems, though SpaceClaim is available exclusively for Windows. The integration between Fluent and SpaceClaim facilitates the import of geometries from various CAD packages, enhancing the creation, separation, and marking of parts and boundaries. Ansys's suite of tools provides a comprehensive multi-physics platform characterized by validated numerical methods, extensive physics and multiphysics capabilities, and substantial user support through online resources and webinars. However, the need for standalone software for pre-processing (SpaceClaim) and the higher costs associated with the complete suite are notable drawbacks(Georgieva et al., 2021).

COMSOL Multiphysics is identified as a pivotal tool for detailed thermal energy storage (TES) system planning due to its advanced 3D modeling capabilities and integration of groundwater flow, which support comprehensive analysis and design. Its Fluid Flow and Heat Transfer Modules enable detailed workflow research, pre-processing, and post-processing, contributing to high productivity and accuracy. Due to the diverse aspects involved in planning, designing, and assessing energy systems, a variety of tools are necessary to examine and optimize different parameters. For instance, renewable-based district heating (R-DH) systems require tools for system capacity, optimal scheduling, water flow, thermal losses, and pumping costs. While dynamic system simulation tools such as Modelica/Dymola, TRNSYS, and Simulink are effective for capacity and scheduling, they often lack precision in estimating thermal losses and optimizing pipeline design(Ochs et al., 2022). Therefore, multiphysics tools like COMSOL Multiphysics, which integrate heat transfer, fluid flow, and structural mechanics, are preferred for detailed thermal efficiency analysis and pipeline optimization.

OpenFOAM is an open-source software package designed for computational fluid dynamics (CFD). It is highly regarded for its extensive customization options, broad user base, and substantial online support and tutorials. OpenFOAM's flexibility and cost-free nature make it particularly appealing in academic and research contexts. Nonetheless, OpenFOAM requires additional programs for post-processing, which can complicate the installation process and limit functionality in Windows environments.

The advancement of information and computer technology has significantly simplified the study of fluid flow behavior. This progress has reduced the time required for analyzing and simulating processes in thermal systems, thereby enhancing the quality and reliability of results. An analysis of scientific publications on CFD, sourced from the Scopus database, reveals that the earliest publications on this topic date back to 1996. Over the past decade, there has been substantial growth and an accelerated pace of research in CFD, driven by rapid technological advancements and the increasing availability of computational tools. This trend suggests that CFD research will continue to expand in the coming years (Georgieva et al., 2021)These simulation tools each offer distinct features and capabilities that can be leveraged for modeling the thermal efficiency and heat storage potential of salt caverns. The selection of a simulation tool will depend on specific project requirements, including the need for detailed fluid dynamics modeling, multi-physics simulations, and user accessibility

Figure 9 highlights the distribution of usage among various CF D tools, with Ansys Fluent, OpenFOAM, and COMSOL Multiphysics being prominent choices. The visual representation underscores the widespread adoption and importance of these tools in the academic and research community, aligning with the comparative analysis discussed.

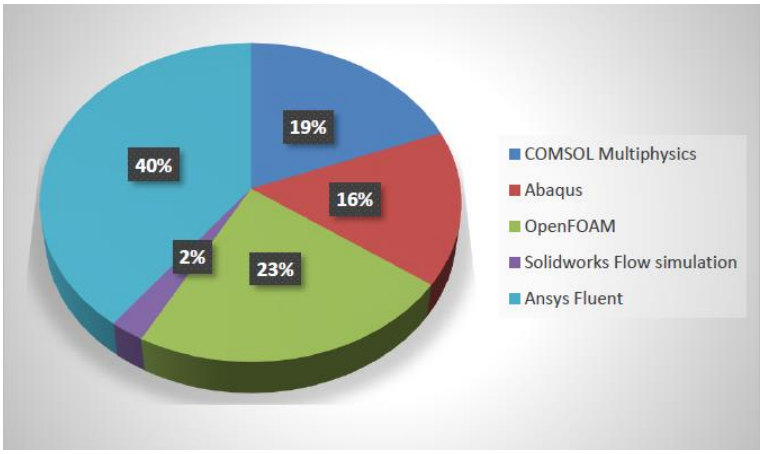

Figure 7: Analysis of the frequency of use of CFD software products in research published in Scopus(Georgieva et al., 2021).

Based on the detailed evaluation of available computational fluid dynamics (CFD) software tools and considering the specific requirements of our simulation project, COMSOL Multiphysics has been selected as the most appropriate tool. COMSOL's advanced capabilities in 3D modeling, that make it particularly well-suited for this project's focus on detailed thermal energy storage (TES) system planning. Its comprehensive multiphysics environment supports a seamless integration of heat transfer, fluid dynamics, and structural mechanics, which is crucial for accurately modeling and optimizing the complex interactions within salt cavern thermal storage systems.

4.2 Heat Transfer/Losses in the Cavern

The thermal behavior of thermal storage systems and the surrounding rocks is influenced by three distinct types of heat losses: periodic, transient, and stationary. Periodic heat losses vary seasonally and are often simplified to annual average temperatures for practicality. Transient heat losses occur during the initial phase and gradually decrease as the surrounding bedrock adjusts to the operational temperature. Stationary heat losses represent the consistent heat loss achieved once the system has stabilized, which is crucial for long-term operational efficiency. This is particularly important in large storage systems, where stationary heat losses benchmark subsequent transient conditions.

The depth of the storage system significantly affects heat losses, with shallower storages experiencing greater thermal leakage. The influence of the ground surface becomes practically significant at depths of 10-20 meters. Initially, the system may inefficiently heat the surrounding bedrock. However, as it transitions from transient to stationary states, the temperature between the cavern and the surrounding rock stabilizes, leading to stationary heat transfer and optimizing energy retention. This highlights the importance of strategic operational planning to enhance the overall efficiency of cavern thermal energy storage (TES) systems (Arnfelt, 2022).

Understanding the fundamental mechanisms of conduction and convection and recognizing the various parameters influencing thermal efficiency is pivotal in heat transfer within caverns.

4.2.1 Conduction

Conduction is the process of transferring heat through a stationary material via physical contact. This happens when neighboring atoms vibrate against each other or when electrons move between atoms. The basic transport processes of momentum, heat, and mass are all described by a similar type of transport equation. This equation explains that a driving force is needed to overcome resistance to move a property. Heat transfer by conduction follows this principle and is described by Fourier's Law in fluids and solids(Rivki et al., n.d.). The rate of heat conduction can be calculated using **equation** 1:

$$\frac{q_x}{A} = -k\frac{dt}{dx} \qquad \text{(eq. 1)}$$

Where:

- q_x is the heat transfer rate in the x direction in watts [W]
- A is the cross-sectional area normal to the direction of flow of heat in [m^2],
- T is temperature in Kelvin [K]
- x is distance in [m]
- k is the thermal conductivity in $[W/(m * K)]$ in the SI system.

The quantity q_x/A is called the heat flux [W/m^2]. The quantity dT/dx is the temperature gradient in the x direction.

4.2.2 Convection

Convection involves the transfer of heat through the large-scale movement of a fluid. This heat transfer can be classified into two main types. The first type is free or natural

convection, which occurs when fluid motion is caused by density changes due to heat transfer. This results in a buoyant effect that creates natural circulation, allowing the fluid to flow past a solid surface. The second type is forced convection, where fluid flow is driven by external forces such as pressure differences, pumps, or fans.

The process of heat transfer through convection is greatly affected by the physical properties of the moving fluid. These properties include thermal conductivity (k), density (ρ), specific heat (Cp), and dynamic viscosity (μ). Although convection is a complex heat transfer process, it is directly proportional to the temperature difference between the fluid and the surface. This relationship is effectively described by Newton's Law of Cooling in as shown in **equation** 2 (Yunus & Cengel, 2004).

$$\frac{dQ}{dt} = h(T_s - T_\infty) \qquad \text{(eq. 2)}$$

Where:

- Q is the rate of heat transfer,
- h is the convective heat transfer coefficient,
- A is the surface area through which heat is transferred,
- Ts is the surface temperature, and
- $T\infty$ is the fluid (ambient) temperature

In salt caverns, natural convection can occur due to geothermal gradients, thus the heat transfer would be greater at the bottom leading to a greater temperature at the lower section of the cavern, and due to the density difference of the between the hot brine and cold brine.

4.2.3 Thermal Stratification

Thermal stratification is a phenomenon in thermal energy storage (TES) systems where the storage medium develops distinct temperature layers, leading to a vertical separation of warm and cool regions. This natural layering effect is due to density differences caused by temperature variations, which cause hotter water to rise to the top and cooler water to sink to the bottom, creating a transition zone known as the thermocline(Njoku et al., 2014). The need for thermal stratification arises from its ability to significantly improve the efficiency of TES by reducing undesired mixing and preserving temperature gradients, which is essential for optimizing the efficiency of various TES applications.

In TES systems, natural convection driven by buoyancy forces due to density differences between hot and cold fluids leads to the formation of stratification. This stratification minimizes

thermal mixing and maintains a stable temperature gradient, with the hot layer on top acting as a thermal barrier that reduces the heat transfer rate to the cooler layers below. This stable density gradient resists mixing, allowing hot water to retain its thermal energy for extended periods. Strong thermal stratification also suppresses buoyancy-driven flow, which decreases heat transfer due to convection.

Several factors contribute to the formation and maintenance of thermal stratification. The material properties of storage walls play a significant role, with TES systems using walls made of materials that have higher thermal diffusivity than the storage medium. This creates a thermal bridge between hot and cold layers, inducing thermal convection within the system. Heat loss and natural convection also contribute to stratification. Losses from TES systems through conduction and convection help establish thermal stratification, with natural convection driven by buoyancy forces playing a pivotal role in creating and maintaining distinct layers(Njoku et al., 2014).

The temperature difference between the upper and lower layers is a key parameter influencing the formation of thermal stratification. A more significant temperature difference often enhances the creation of distinct layers. Flow rates also impact the degree of thermal stratification, as higher flow rates may disrupt stratification by causing unwanted mixing within the system. The geometry of storage tanks is also crucial, with the shape and dimensions of the storage container playing a pivotal role in establishing and maintaining stratification. Specific geometries can either facilitate or impede the layering effect. Additionally, the location and design of inlet and outlet points are critical in determining flow patterns and influencing the degree of stratification within the TES system. Higher temperature differences between inlet and stored tank water reduce mixing due to greater density differences between layers.

Addressing these factors comprehensively is essential to achieving a deeper understanding of thermal stratification. This understanding lays the groundwork for optimizing TES systems and their varied applications.

Figure 10 showcases the factors that lead to de-stratification. Heat loss to the surroundings occurs when heat escapes from the storage system to the external environment, disturbing the temperature gradients within the storage medium. Forced convection, introduced by external influences such as pumps or mechanical mixers, can mix layers of different temperatures, leading to a loss of stratification. Heat conduction between layers can cause the layers to homogenize over time, reducing the effectiveness of stratification. Natural convection,

driven by density differences at varying temperatures, can result in fluid movement within the storage, potentially disrupting the thermal layers(Njoku et al., 2014).

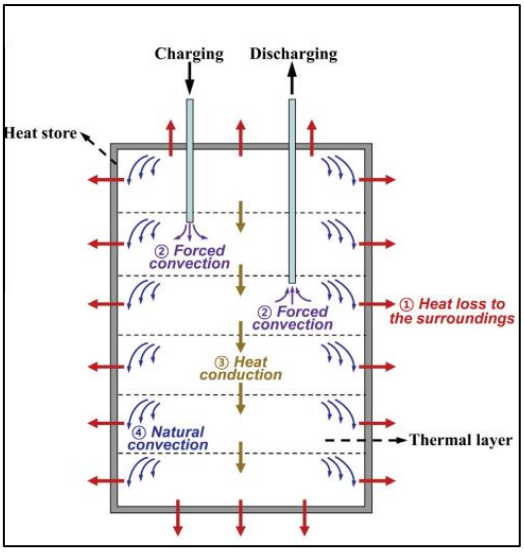

Figure 10. Factors effecting thermal stratification.

4.3 Shape, Geometrical and Operational Considerations of Thermal Storage

Due to the limited literature on using salt caverns for heat storage, comparing them to storage tanks is reasonable since both are open-hole systems. Many Thermal Energy Storage Systems (TTES) studies mainly focus on thermal stratification. The geometry and shape of thermal storage tanks are crucial for their thermal performance, affecting energy efficiency, exergy efficiency, and entropy generation. The height-to-diameter (H/D) aspect ratio is a key factor influencing the tank's standby heat losses and thermal stratification.

The **aspect ratio** of storage tanks significantly affects standby heat losses. Natural convection, axial wall conduction, and ambient heat losses depend on the tank's surface area, which is influenced by the aspect ratio. An optimal balance is essential; for example, increasing the aspect ratio from 2.5 to 5 can improve thermal stratification by up to 30.69% and reduce initial mixing at the inlet. However, a higher aspect ratio enhances stratification and increases ambient heat losses due to a larger surface area. Thus, there is a trade-off between stratification efficiency and heat loss. Tanks with higher aspect ratios and thinner walls benefit from reduced de-stratification during dynamic operations but at the cost of increased ambient heat losses. An optimal aspect ratio is typically between 3 and 4, balancing improved stratification with minimized heat losses (Chandra & Matuska, 2019).

Different tank shapes exhibit varying thermal behaviors. Circular truncated cone tanks maintain superior temperature stratification, especially at specific radius ratios. In contrast, despite their minimal surface area and excellent thermal insulation, spherical tanks are less effective in stratification. This highlights the complex relationship between tank shape and thermal performance, emphasizing the importance of careful design to optimize thermal efficiency(Li et al., 2018). The shape is determined during the construction of salt caverns, limiting the ability to optimize thermal performance by shape. Therefore, selecting a cavern with a favorable shape or constructing a new cavern specifically for storage may be necessary.

The relationship between the aspect ratio and surface area is crucial, as a higher aspect ratio can enhance convection currents due to increased ambient losses. Therefore, selecting a cavern with an optimal aspect ratio and shape is essential to minimize heat loss, maximize energy efficiency and stratification, and ensure the system's overall thermal integrity(Lou et al., 2021a).

The research of Wanruo Lou *et al.* provided a table with comprehensive parametric study on thermocline-based thermal energy storage (TES) systems, focusing on the impacts of flow rate and temperature range on system performance. Studies involving vertical cylinders with various inner structures, such as no packing and porous beds, indicate that low inlet flow rates confine mixing to specific zones, preserving thermocline stability during discharging, while higher inlet flow rates lead to more pronounced mixing and thermocline deterioration (Dehghan & Barzegar, 2011) (Yaïci et al., 2013). Optimal flow rates balance mixing and thermal diffusion, enhancing overall system performance (Nandi et al., 2018). Inlet velocity significantly affects transient thermocline thickness, mechanical stress on steel walls, and overall charging/discharging efficiency (Wang et al., 2020). Regarding temperature range, higher ΔT generally increases thermal stratification and penetration length, thus improving thermal storage efficiency. However, higher ΔT also increases mixing and thermocline thickness, potentially reducing (Lou et al., 2021a). Different inner structures without packing affect thermal performance, with higher temperature ranges leading to thicker thermoclines and more mixing (Yaïci et al., 2013). This analysis underscores the importance of optimizing both flow rates and temperature ranges to enhance the efficiency and performance of thermocline-based TES systems, providing valuable insights for TES design and implementation.

The impact of inlet/outlet locations on thermal energy storage (TES) performance was extensively studied. Differences in density and velocity between incoming flow and stored fluid

create a shear layer and jet at the inlet, leading to vortex formation and mixing within the storage vessel (Lou et al., 2021a). To mitigate excessive mixing, it is recommended to position inlet/outlet ports near the top or bottom of the tank (Toyoshima *et al.,* 2013). Experimental and numerical studies suggest placing these ports close to the upper and lower walls enhances exergy efficiency (Assari *et al.,* 2018; Yaïci *et al.,* 2013; (Lou et al., 2021a)). Configurations with immersed pipes for introducing and extracting fluid further improve performance by reducing thermal conduction between the pipes and stored fluid(Lou et al., 2021a). These findings underscore the importance of optimal port positioning to minimize mixing and maintain thermal stratification, thereby enhancing TES system efficiency

4.4 Turbulent Flow

Turbulent motion is characterized by its irregular and chaotic nature. This irregularity can be described by turbulent fluid motion exhibiting random variations in quantities like velocity components and pressure over time and space. These variations are such that their statistical averages can be quantitatively expressed. Turbulence involves random fluctuations arising from disturbances, such as surface roughness. These fluctuations can either be dampened by viscous forces or grow by drawing energy from the surrounding flow. When the Reynolds number is below a critical threshold, the kinetic energy of the flow is insufficient to maintain these fluctuations against viscous damping, resulting in laminar flow. However, when the Reynolds number exceeds this critical value, the kinetic energy supports the growth of fluctuations, leading to the onset of turbulence (Uruba, 2019).

The Reynolds number (Re) is a dimensionless quantity used to predict flow regimes in fluid dynamics. It's calculated as the ratio of inertial forces to viscous forces in the fluid and is given by **equation** 3

$$Re = \frac{Density \times Velocity \times Characterstic\ length}{Viscosity} \quad \text{(eq. 3)}$$

Interpretation of the Reynolds number:

- $Re < 2000$ indicates laminar flow.
- $2000 < Re < 4000$ suggests transitional flow.
- $Re > 4000$ signifies turbulent flow.

Equation 4 is the Navier-Stokes equation describe the motion of fluid substances and are the foundation of fluid dynamics.

$$\frac{\partial u}{\partial t} + (u \cdot \nabla)u = -\nabla p + \nu \nabla^2 u + f \quad \text{(eq. 4)}$$

The local acceleration ($\frac{\partial u}{\partial t}$) and convective acceleration (u·∇)u on the left side of the equation represent the total acceleration of a fluid particle. While the right side of the equation consists of the forces acting on the fluid: the pressure gradient force ($-\nabla p$) viscous diffusion ($\nu \nabla^2 u$) , and any external body forces (f) (Bistafa, 2018)(Uruba, 2019)(Bistafa, 2018).

There are several methods to solve turbulence, each with applications and limitations. Direct Numerical Simulation (DNS) is feasible but only for low Reynolds number flows and simple geometries, as it requires resolving all scales of turbulence. However, DNS's detailed time and space information is unnecessary for design purposes. Large Eddy Simulation (LES) offers a compromise by resolving large-scale turbulence structures while modeling the smaller eddies, making it suitable for more complex flows but still computationally intensive. For most engineering applications, the Reynolds-Averaged Navier-Stokes (RANS) equations are commonly used, as they average the effects of turbulence over time, providing sufficient accuracy for design purposes without the need to capture the smallest eddies(Idealsimulations, n.d.).

The k-ε model is one of industrial applications most widely used turbulence models. It includes the standard k-ε model, introducing two additional transport equations and dependent variables: turbulent kinetic energy (k) and turbulent dissipation rate (ε). Low Reynolds number turbulence is most commonly found in the near-wall region in industrial processes. Consequently, the low Reynolds number k−ε turbulence model focuses on accurately representing turbulence in these near-wall regions. This focus is crucial because the behavior of turbulence near walls significantly affects the overall flow characteristics and performance in many industrial applications. Therefore, for applications where near-wall resolution is essential, low Reynolds number k−ε would be a preferable option (Multiphysics, 2015).

The Kays-Crawford model provides a relatively exact model for the turbulent Prandtl number (PrT), which is essential for determining turbulent thermal conductivity. This leads to more precise heat transfer predictions, especially in boundary layers and duct flows. By accounting for the effective thermal conductivity, the model leads to more accurate predictions

of heat transfer rates in turbulent flows, particularly in regions close to walls with steep temperature gradients(Multiphysics, 2015).

4.5 Performance and efficiency metrics

In the study of thermal energy storage (TES) systems, thermal or energy efficiency is a critical parameter that directly impacts the overall performance and cost-effectiveness of the system. Thermal efficiency can be broadly defined as the ratio of useful output energy in the form of heat to the total input energy, often expressed as a percentage. This measure provides a quantitative assessment of how effectively a TES system can store and release thermal energy with minimal losses(Ma et al., 2012).

The evaluation of thermal efficiency in TES systems can be approached through various metrics, each offering unique insights into different aspects of system performance. These metrics are primarily grounded in the principles of the first law of thermodynamics, which governs the conservation of energy. The key metrics used to assess thermal efficiency include energy efficiency and capacity ratio. Energy efficiency is a functional measure dependent on the ratio of the net difference between input and output energy to the total input energy(Lou et al., 2021b) .

The efficiency during the energy input phase when the system is being charged with thermal energy is called **Charging Efficiency** (**equation** 5):

$$\eta ch = \frac{E_{in} - E_{out}}{E_{in}} = \frac{\int_0^t \dot{m} C_p (T_{in}(t) - T_{out}(t)) dt}{\int_0^t \dot{m} C_p (T_{in}(t) - T_0) dt} \qquad \text{(eq. 5)}$$

Where:

- ηch is the charging efficiency
- E_{in} is the input energy
- E_{out} is the output energy
- $\dot{m}$ is the mass flow rate
- cp is the specific heat capacity
- $T_{in}(t)$ the inlet temperature as a function of time
- $T_{out}(t)$ is the outlet temperature as a function of time, and
- T_0 is the initial reference temperature

The efficiency during the energy output phase when the stored thermal energy is being utilized is given by the **equation** 6 of the **Discharging Efficiency**(Lou et al., 2021b):

$$\eta dis = \frac{E_{out} - E_{in}}{E_{stored}} = \frac{\int_0^t \dot{m} C_p (T_{out}(t) - T_{in}(t)) dt}{E_{stored}} \quad \text{(eq. 6)}$$

Where:

- ηdis is the discharging efficiency
- E_{out} is the output energy
- E_{in} is the input energy, and
- E_{stored} is the stored energy.

An aggregate measure that sometimes reflects the impact of cyclic operations, indicating how the system performs over multiple charge-discharge cycles is the **Overall Efficiency** given by **equation** 7:

$$\eta_{overall} = \frac{E_{out}}{E_{in}} \quad \text{(eq. 7)}$$

Where:

- ηoverall is the overall efficiency
- E_{out} is the total energy output, and
- E_{in} is the total energy input.

4.6 Geomechanical Analysis of Rock Salt for Energy Storage Applications

In rock mechanics, materials can undergo two main types of deformation: elastic and plastic. Elastic deformation, like stretching a rubber band, allows the material to return to its original shape once the stress is removed. Conversely, plastic deformation results in a permanent change in shape even after the stress is released. This distinction is often illustrated on a stress-strain diagram, where materials initially stretch elastically along a straight line. However, with continued stress, materials undergo plastic deformation, including strain

hardening or strain softening, where materials either strengthen or weaken as they deform. Despite stress removal, some deformations persist due to their irreversible nature .

4.6.1 Creep Behavior in Rock Salt

Rock salt exhibits unique mechanical properties influenced by stress-dependent domains known as dilatancy and compaction. In the dilatancy domain, micro-crack formation and propagation increase porosity and weaken the material, potentially leading to failure through creep. In contrast, the non-dilatant compaction domain involves plastic deformation and micro-crack compaction, which may initiate a healing process that reduces permeability. Additionally, pure creep, driven by dislocation movement and elastic deformation, can occur in this domain. These behaviors in rock salt are influenced by various factors such as temperature, stress, water content, and the intrinsic structure of the rock (Schulze et al., 2001).

4.6.2 Understanding Material Behavior

Understanding the behavior of materials under various conditions is essential for predicting stress and strain, determining acceptable stress levels, and identifying potential failure points. Diverse material models capture linear elastic behavior, creep, and pre- and post-failure behavior. Selecting models that match specific material characteristics and responses can improve understanding of material behavior under different stress regimes. This, in turn, aids in the development of effective engineering designs and strategies to ensure material integrity and stability.

For example, the Bundesanstalt für Geowissenschaften und Rohstoffe (BGR) utilizes the BGR creep model to study salt behavior. Hooke’s law for linear elastic behavior is integrated with BGR's creep law in this model. The Fokker creep model, which addresses secondary creep using the same creep law as BGR's, also incorporates primary creep. Primary creep is observed immediately after a change in load and is evident at the beginning of a creep test when loads are first applied (Wijermans, 2013).

The time-dependent deformation (creep) of salt is significantly affected by temperature. A decrease of 50 °F (11 °C) can result in a five-fold reduction in the salt creep rate, which is crucial for the design, performance, and stability of cavern fields in geomechanical terms (Circle & Voegeli, 2018). Furthermore, a direct relationship between internal pressure and long-term creep performance in salt cavern gas storage has been identified. Greater creep and

deformation occur with lower internal pressures, emphasizing the need to avoid extreme pressure levels (Liu & Xiao, 2014).

4.6.3 Phases of Creep

The three phases of creep can be understood with reference to **Figure** 11a. **Primary Creep** (Phase I) begins with high creep rates that decrease as deformation progresses. Initially, dislocation movement within the crystal lattice dominates, but as deformation continues, new dislocations form, increasing the material's resistance against further deformation. This stage is depicted by the initial curve in the green section labeled "primary creep," where the deformation rate ($\dot{\varepsilon}$) decreases transiently. As deformation proceeds, the material transitions into **Secondary Creep** (Phase II), or the stationary creep phase, where the rates of dislocation movement and recovery balance each other, resulting in a constant creep rate. This phase is represented by the flat portion of the red section labeled "secondary creep," where $\dot{\varepsilon}$ remains constant. If damage progresses beyond the dilatancy threshold, the material enters **Tertiary Creep** (Phase III), characterized by accelerated creep rates leading to eventual creep failure. This phase is illustrated in the blue section labeled "tertiary creep," where $\dot{\varepsilon}$ increases rapidly, culminating in creep fracture.

Additionally, **Figure** 11b shows the behavior of a material that can creep (red line) versus a material that cannot creep (blue line). At two specific points in time, labeled 1 and 2, the load on both materials increases, leading to increased strain. However, during periods of constant load, the strain remains constant for the non-creeping material (blue line), whereas it continues to increase for the creeping material (red line).

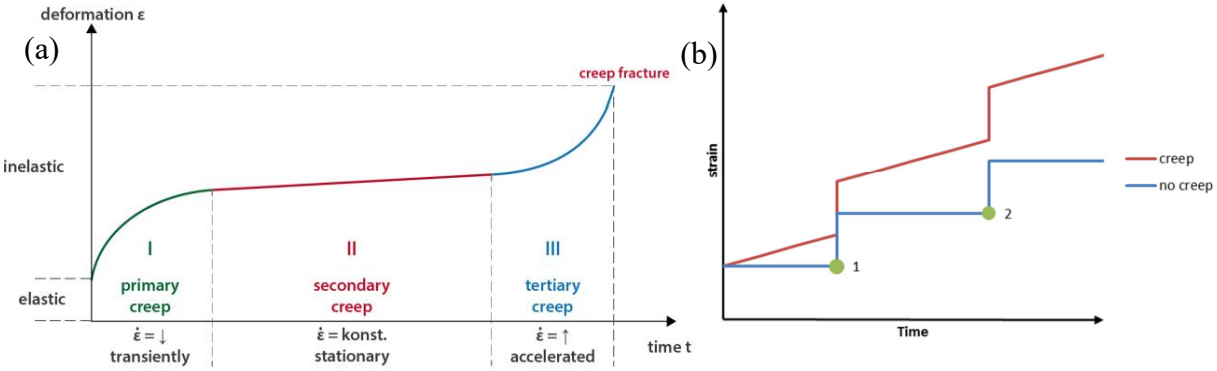

Figure 11. (a) Creep test with three creep phases. (b) Creep Comparison. Blue line: Non-creeping material. Red line: Creep-prone material. Strain remains constant for the blue line during constant load, while steadily increases for the red line.

4.6.4 Influence of Temperature on Rock Salt

Temperature significantly impacts the geo-mechanical properties of rock salt. As temperature increases, a noticeable reduction in P-wave velocity (Vp) is observed, indicating a decrease in the rock's ability to transmit seismic waves efficiently. Concurrently, the tensile strength of rock salt exhibits a non-linear decline, reflecting a weakening in its resistance to tensile stress. In contrast, the uniaxial compressive strength increases linearly with temperature, suggesting enhanced ductility and a greater ability to withstand axial loads. This transition from brittle to ductile behavior is further evidenced by a significant increase in axial strain at ultimate stress levels.

Additionally, acoustic emission (AE) activity, which tracks microcrack formation and propagation, intensifies with temperature, indicating more active microcrack development. X-ray micro-CT imaging reveals a corresponding increase in microcracks and porosity as temperature escalates. These findings underscore the critical impact of temperature on rock salt's structural integrity and mechanical behavior, emphasizing the necessity of accounting for thermal effects in the design and stability assessment of rock salt storage caverns.

There are several criteria in order to evaluate the safety of the salt cavern which the most important are the following:

1. **Volume Shrinkage Limits**

To ensure the long-term stability and integrity of salt caverns used for storage, specific volume shrinkage limits have been established. specify that the volume shrinkage of a salt cavern should be no more than 1% after one year and no more than 30% after thirty years. Building on this, Liu *et al.* (2018) provide a more detailed criterion, setting limits of 1% volume shrinkage after one year, 5% after five years, and maintaining the 30% limit after thirty years. Chen *et al.* (2020) similarly focus on these timeframes, reinforcing the importance of limiting volume shrinkage to 1% within the first year and 30% over thirty years.

2. **Displacement Limits**

The maximum displacement of salt caverns should not exceed 5% of the maximum cavern diameter. This criterion is crucial for maintaining the structural integrity and stability of the caverns, ensuring that deformation remains within safe limits. By adhering to this guideline, the risks associated with excessive displacement, such as structural failure or compromised storage capacity, are significantly mitigated (Zhang et al., 2023).

3. **Geological Tightness**

Geological tightness must be maintained to ensure that the cavern remains sealed and stable. This is achieved by ensuring that the minimum principal stress (σmin) in the surrounding rock is sufficiently high. Specifically, σ_{min} should be at least 10% higher than the maximum internal pressure (P_{max}) within the cavern (Susan, 2019):

$$\sigma_{min} \geq 1.1 \times P_{max} \quad \text{(eq. 8)}$$

4. **Internal Pressure Limits**

The maximum internal pressure should be controlled to prevent overpressure and potential structural failure. This is typically limited to 85% of the lithostatic pressure at the cavern depth (Susan, 2019)(**equation** 9):

$$P_{max} \leq 0.85 \times P_{lithostatic} \quad \text{(eq. 9)}$$

This ensures that the cavern can withstand the internal pressure without compromising its structural integrity.

5. **Subsidence Limit**

Subsidence, or the gradual sinking of the ground surface, is an ongoing process that must be continuously monitored. It is recommended to set a maximum allowable subsidence rate to ensure long-term stability. A commonly used threshold is 2.5 millimeters per year. Regular geological assessments and pressure adjustments are necessary to maintain subsidence within this limit (Susan, 2019).

5. Methodology

To effectively address the research questions posed in this study, a comprehensive methodological framework was employed, combining computational fluid dynamics (CFD) simulations and heat transfer modeling using COMSOL Multiphysics. These methodologies were selected for their ability to accurately simulate the complex thermal and fluid dynamic interactions within salt caverns, particularly under varying operational conditions. Given the intricate behavior of heat propagation and fluid dynamics challenges that are difficult to assess through traditional experimental methods the use of CFD and heat transfer modeling is crucial for this study.

The appropriateness of this methodology is underscored by the precision needed to capture how different parameters such as cavern shape, aspect ratio, flow rates, and temperature settings impact overall thermal efficiency. These parameters are particularly relevant within the context of the Röt salt formations, whose specific geological and petrophysical characteristics were integrated into the model. By employing fundamental principles of fluid dynamics and heat transfer, the model replicates real-world conditions within the salt caverns, ensuring that the findings are both scientifically robust and contextually relevant.

In applying this methodology, a 3D model was developed using COMSOL Multiphysics to investigate the interaction between heat transfer and turbulent flow, tailored to the unique geological context of the Röt salt formations. The model incorporates specific cavern dimensions and material properties derived from geological data, ensuring its accuracy. Additionally, a multi-phase evaluation was conducted to explore the effects of varying operational parameters on thermal efficiency. This approach allowed the study to not only test existing theories but also to investigate new research questions related to optimizing energy storage in salt caverns.

The methodological framework that is being used in this study is illustrated in **Figure** 12, highlighting the integration of data collection, modeling, analysis, and optimization processes. It visually includes the systematic approach taken to explore and address the research questions, emphasizing the role of each phase in achieving the study's objectives.

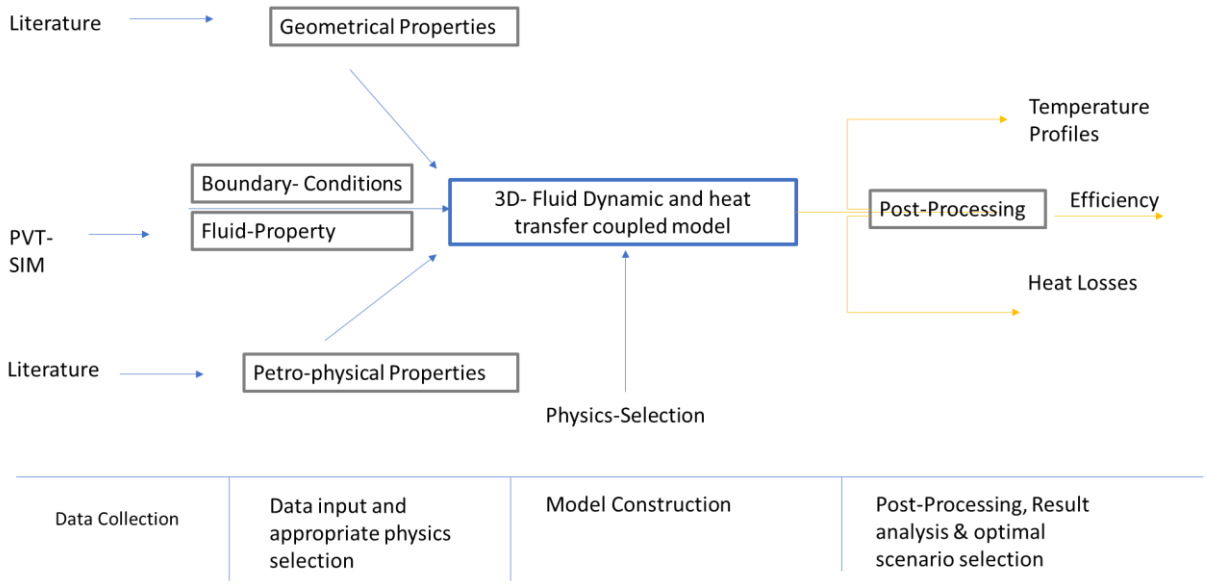

Figure 12: Methodological Framework for Assessing Thermal Efficiency in Salt Caverns

5.1 Data Collection

In this section, the choices for the model geometry, petrophysical parameters, and flow dynamics essential for the salt cavern heat storage study are outlined. The cavern's dimensions and shape, the properties of the geological formations, and the inlet and outlet flow rates and positions are detailed, laying the groundwork for the simulation analysis. It is noteworthy that the chosen shape for the simulation may vary in Twente, depending on the type of cavern construction.

5.1.1 Geological Formation and Depths

The depth and type of geological formation for the salt cavern model were determined by examining lithological data from various wells in the Twente region, as discussed in **Chapter** 2.2. Based on this information, the modeled salt caverns are situated within the Triassic Röt Evaporite Formation, part of the Upper Germanic Triassic Group (RN). The geological context and lithology of the salt caverns, including depths determined by averaging data from relevant wells, are detailed in **Chapter** 2.2. The salt cavern lies within the Röt Claystone Formation, extending down to 350 meters, followed by the Röt Evaporite Formation from 350 to 450 meters, and the Soling Claystone Formation down to 800 meters. To ensure the simulation accurately reflects the typical physical characteristics of the Röt formation, the model was aligned with these real-world conditions, with a simulation domain defined as 350 meters in width and 250 meters in length.

5.1.2 Cavern Shape and Dimensions

The Röt salts are located at relatively shallow depths of 400-500 meters, where approximately 270 disc-shaped, thin caverns have been developed through solution mining, with an average diameter of 120 meters and a height of a few dozen meters (Muntendam-Bos et al., 2022). This information, consistent with **Chapter** 2.2, justifies the chosen shape of the cavern in the modeling. Additionally, a safety thickness of at least 5 meters is maintained above and below the cavern to ensure structural integrity. The input parameters for both the formation depths and cavern shape are summarized in **Table** 2.

Table 2: Summary of Model Geometry Parameters

Parameter	Value [m]
Formation Width (X)	350
Formation Depth (Y)	250
Height Rot Claystone formation	350
Height Rot Evaporite formation	100
Height Rot Soiling Clay formation	350
Upper & Lower Salt Thickness	30
a Ellipse	60
b Ellipse1	30
Cavern Height	40
Well radius	0.3

5.1.3 Petrophysical Parameters

In this subsection the petrophysical properties of each geological formation involved in the study will be highlighted, by employing data from geological assessments and available sources. Essential parameters such as porosity, permeability, thermal conductivity, and other relevant petrophysical characteristics will be covered which are crucial for the accuracy of the simulation. For the parameters used in the model, an average of the available data has been utilized to ensure consistency and reliability.

There is no rock mechanical data exist for the Röt Salt formation from lab experiments, only for the Zechstein salt from various locations around NL. The information about salt properties was extracted from a (Hunfeld et al., 2022) . Typical values are used instead in the **Table** 3, but the creep rate (A1, A2) can vary quite a bit from one salt to another. These values match two sets of lab data from Zuidwending and Barradeel and would be used in the model for the gromechanical model used in Diana.

The parameters listed in **Table** 3 are critical inputs for the various aspects of the modeling conducted in this study. They inform the thermal and geomechanical behavior of the modeled salt cavern, ensuring that simulations closely reflect the real-world conditions of the Röt formation. Specifically:

1. **Thermal Modeling**: Parameters such as density, heat capacity, and thermal conductivity are used to simulate heat transfer within the cavern and surrounding geological formations.
2. **Geomechanical Modeling**: Mechanical properties like Young's Modulus, Poisson's Ratio, and creep parameters are essential for assessing the structural stability of the cavern, particularly in response to thermal stresses.

These inputs are crucial for ensuring that the simulations are accurate and relevant to the specific conditions encountered in the Röt salt formation, thus providing reliable data for optimizing the cavern's thermal efficiency.

Table 3: Summary of Geological Formation and Mechanical Properties Used in Modeling

Parameter	Value	Description/Purpose	
Evaporite Heat Capacity [J/kg·K]	1100	Determines heat storage capacity of the evaporite formation.	**Formation Parameters**
Evaporite Thermal Conductivity [W/m·K]	2	Governs heat transfer rate within the evaporite.	
Rot Clay Density [kg/m³]	2000	Used in modeling thermal and mechanical properties of the Rot clay.	
Rot Clay Heat Capacity [J/kg·K]	1350	Determines heat storage capacity of the Rot clay formation.	
Rot Clay Thermal Conductivity [W/m·K]	2	Governs heat transfer rate within the Rot clay formation.	
Soling Clay Density [kg/m³]	2600	Used in thermal and mechanical modeling of the Soling clay layer.	
Soling Clay Heat Capacity [J/kg·K]	1400	Determines heat storage capacity of the Soling clay formation.	
Soling Clay Thermal Conductivity [W/m·K]	1.2	Governs heat transfer rate within the Soling clay formation.	
Geothermal Gradient [°C/m]	0.03	Defines the temperature increase with depth in the geological model.	
Surface Temperature [°C]	10	Initial surface temperature for geothermal gradient	

Density [kg/m³]	2130-2200	Average density for the cavern and surrounding formations.	**Mechanical Properties**
Young's Modulus [GPa]	30-32	Elastic property used in geo-mechanicallmodeling	
Poisson's Ratio [−]	0.26-0.3	Describes deformation characteristics in mechanical modeling.	
Thermal Expansion Coefficient [1/K]	3×10^{-5}	Used in thermal stress analysis within the cavern.	
Heat Conductivity [J/day·m·K]	1.71×10^{5}	Governs heat transfer rate within the mechanical model.	
Heat Capacity [J/m³·K]	1.84×10^{6}	Determines heat storage capacity in the mechanical model.	
Initial Stress Ratio [K_0]	1	Assumed for initial geomechanical stress conditions.	
Elastic Equivalent Young's Modulus [GPa]	0.075	Equivalent elastic modulus for mechanical modeling.	
Elastic Equivalent Poisson's Ratio [−]	0.005	Equivalent Poisson's ratio for mechanical modeling.	
A1 [1/day]	5	Parameter for time-dependent mechanical modeling.	
A2 [1/day]	1	Parameter for time-dependent mechanical modeling.	
n1 [−]	6495	Parameter for non-linear mechanical behavior.	

n2 [−]	3007	Parameter for non-linear mechanical behavior	

5.1.4 Working Fluid Brine Properties

Saturated brine at 60 °C, with an NaCl percentage of 26.395%, was utilized. The characteristics of the brine at saturation level were calculated using PVT simulation at an average temperature of 60 °C. The values are presented in the table below. While other properties were calculated specifically at 60 °C, density and viscosity were examined across a broader temperature range. Data were collected at 35 temperature points, ranging from 20°C to 105°C with increments of 2.5 °C. These data points were then plotted, and a fitting process was applied to develop formulas representing both density and viscosity as functions of temperature. This comprehensive approach ensured a detailed understanding of the brine's behavior across a wide temperature range.

Table 4 presents the key physical properties of the saturated brine solution utilized in the simulation, including density, specific heat capacities at constant pressure (C_p) and constant volume (C_v), viscosity, and thermal conductivity. All values were computed using PVT simulation at an average temperature of 60 °C. These parameters are critical for accurately modeling the thermal and fluid dynamics within the salt cavern.

Table 4: Summary of Brine Parameters Used in the Simulation

Parameter	**Value**
Brine Density	1151 [Kg/m^3]
C_p Brine	4165 [J/kg C]
C_v Brine	3953 [J/kg C]
C_p/C_v Brine	1.05
Brine Viscosity	$9.357*10^{-4}$ [Pa.s]
Thermal Conductivity	0.495 [W/m C]

Figure 13 illustrates the relationship between density and temperature for saturated brine. As the temperature increases, the density decreases, following a linear relationship described by the equation $y = -0.5542x + 1213.6$ with $R^2 = 0.9999$. The high R^2 value indicates an extremely strong fit to the experimental data. This linear inverse relationship suggests that as the brine heats up, its density decreases consistently.

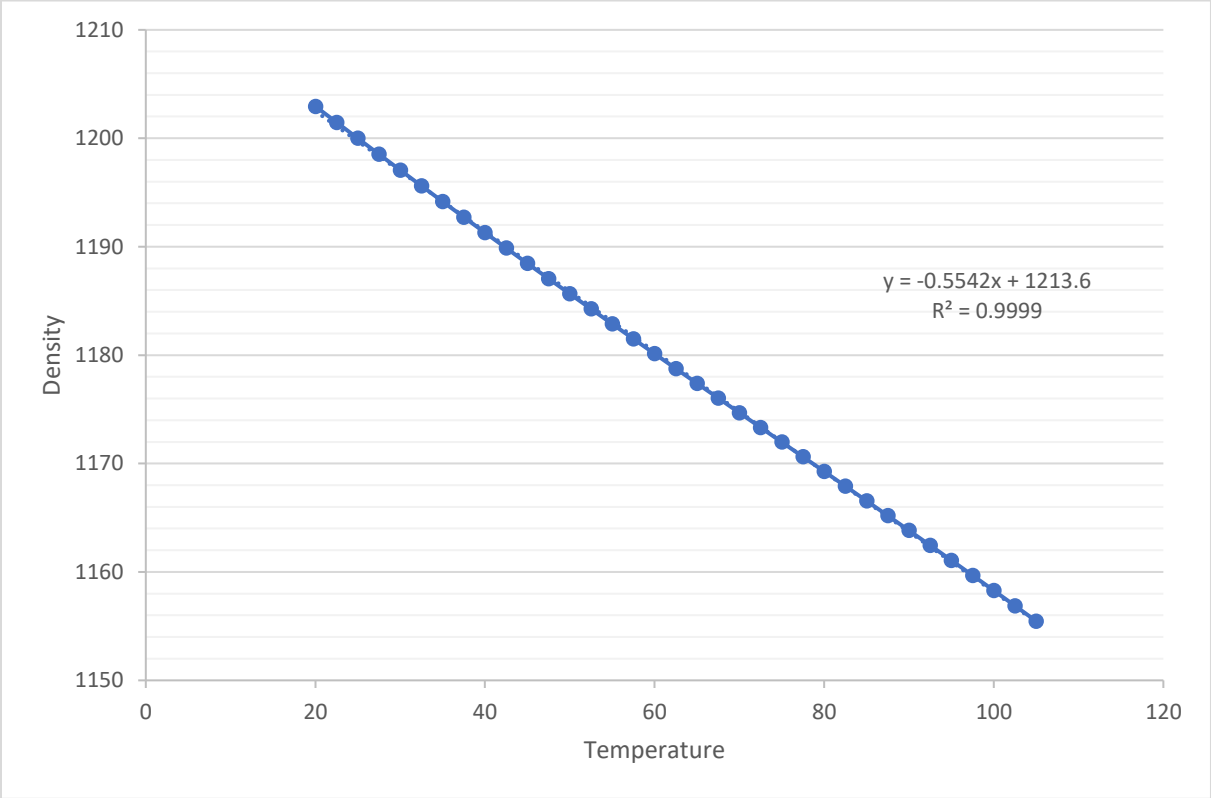

Figure 13**:** Fitted relationship between density and temperature for saturated brine derived from PVT simulation, described by the equation $y = -0.5542x + 1213.6$ with an R^2 value of 0.9999

Figure 14 shows the relationship between viscosity and temperature for saturated brine. As temperature increases, viscosity decreases, following a power-law relationship described by $y = 0.026x^{-0.82}$ with R^2 value of 0.986. This high R^2 value of 0.986 indicates a strong fit to the experimental data. This inverse relationship suggests that as the brine heats up, its viscosity decreases significantly

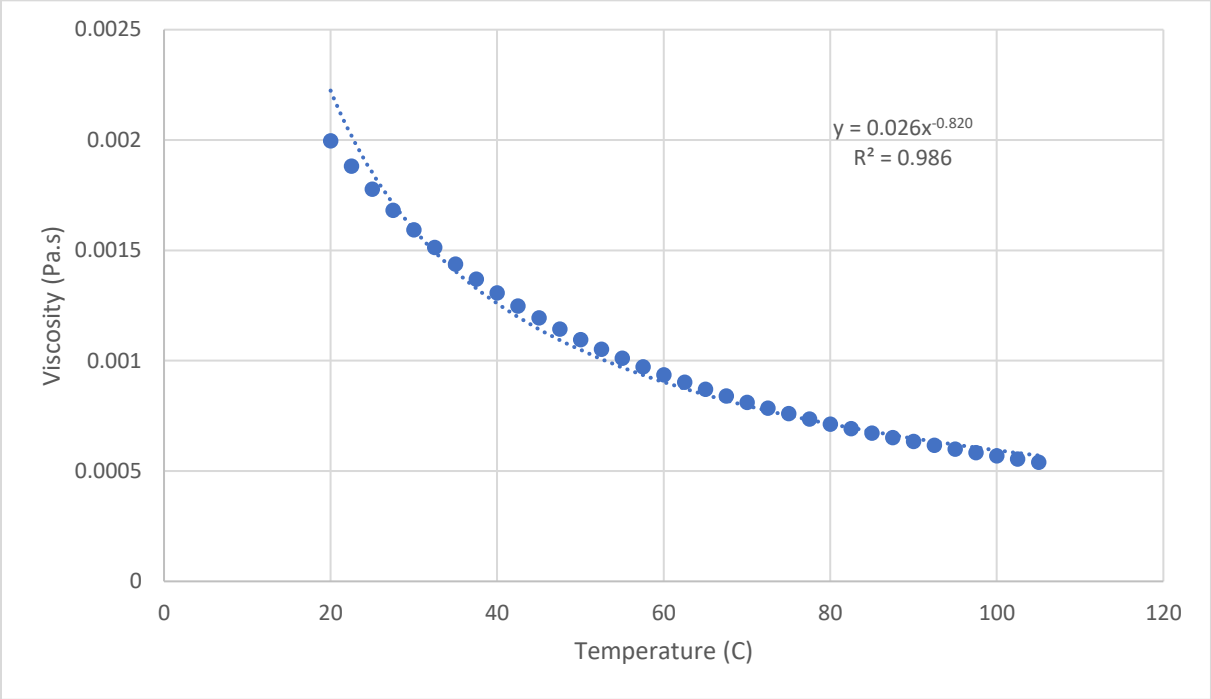

Figure 14: Fitted relationship between viscosity and temperature for saturated brine derived from PVT simulation, described by the equation $y = 0.026x^{-0.820}$ with an R^2 value of 0.986.

5.2 Model Setup and Simulation in COMSOL

This section outlines the comprehensive approach taken to simulate the thermal and fluid dynamics within a salt cavern environment using COMSOL Multiphysics. The methodologies and configurations detailed here ensure a systematic and transparent depiction of the modeling process, facilitating replicability.

5.2.1 Model Geometry

In this section of the methodology, we will elaborate on the comprehensive approach taken to accurately simulate the thermal and fluid dynamics within a salt cavern environment.

To ensure a systematic and transparent depiction of our modeling process, using COMSOL Multiphysics to ensure replicability.

The methodology section describes the critical parameters and configurations used to model the salt cavern within the Röt formation. To further illustrate these configurations, **Figure** 15 provides a visual representation of the model setup within COMSOL. Panel (a) depicts the complete geological formation, showing the relative positions of the Röt Claystone, Evaporite, and Soling Claystone layers, while panel (b) offers a closer view of the cavern itself. The axes of the elliptical cavern are clearly defined, which aligns with the detailed dimensions and shape discussed in Section 5.1.2. This visual aid serves to bridge the gap between the descriptive elements of the methodology and the practical application within the modeling software, ensuring a comprehensive understanding of the setup and its relevance to the study.

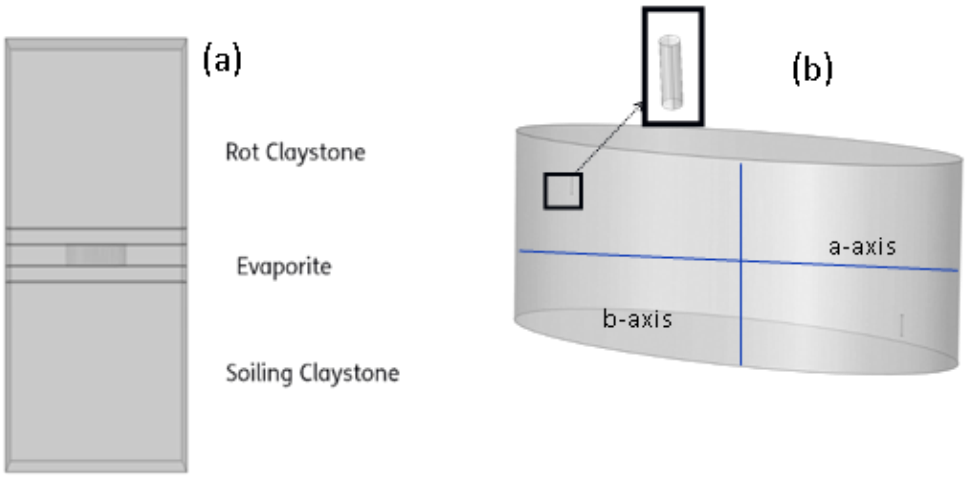

Figure 158: Representation of Formation and Cavern Geometry in COMSOL: (a) Shows the Entire Formation with (b) Zooming in on the Cavern and Inlet Geometry

5.2.2 Flow Rates Set-Up

Flow rates were determined based on a 3-months period as has been discussed in section (3) period for both the charging and discharging phases. To maintain constant pressure within the cavern, it is assumed that the mass flow rate entering the system is equal to the mass flow rate exiting it $mass_{in} = mass_{out}$. This balance is essential for ensuring the system's stability

1 Cycle = 3 months = 2160 h/ 3 months

The volume of an elliptical cylinder can be calculated using the formula:

$$Volume = \pi \times a \times b \times h$$

where:

- *a=60m* is the semi-major axis of the ellipse
- *b*=30 is the semi-minor axis
- *h*: is the height of the cylinder.

Volume= 226,195m^3

$$\dot{V} = \frac{\dot{m}}{\rho} = \frac{V}{t} = \frac{226{,}179\ m^3}{2160\ h} = 78.5\frac{m^3}{h}$$

$$\dot{m} = \rho \times \dot{V} = 1151 \times 78.5 = 86{,}350\frac{kg}{h} \times \frac{1\ h}{3600\ s} = 24\frac{kg}{s}$$

5.2.3Injection and production Set up

The strategic positioning of the inlet and outlet points within the cavern was designed to optimize both storage efficiency and heat transfer, while minimizing mixing of fluids. The following table details the configurations for both charging and discharging phases.

Table 5: Table illustrating the Injection and Production Details for Charging and Discharging Phases in the Salt Cavern Thermal Energy Storage System, including brine temperature, injection locations, and horizontal distances from the cavern sides

Stage	**Hot Well (At Top)**	**Production Well (At Bottom)**
Injection	Injection of 80°C brine at the upper part	Producing cold fluid from the lower part
	Located at 0.25H_{cavern} cavern from the top	Located at 0.25H_{cavern} from the bottom
	10m away from the side horizontally	10m away from the side horizontally
Production	Injection of 40°C brine (Return) at the lower part	Producing hot fluid from the upper part
	Located at 0.25H_{cavern} from the bottom	Located at 0.25H_{cavern} cavern from the top
	10m away from the side horizontally	10m away from the side horizontally

The placement of the inlet and outlet at a distance of 0.25 of the cavern's height from the top and bottom, respectively, along with their 10-meter distance from the sides, not only optimizes fluid flow and heat transfer but also will delay the connection between the inlet and outlet. thereby reducing mixing (Karim et al., 2018). This strategic positioning ensures that the injected brine and extracted brine have sufficient space to circulate within the cavern without immediately mixing upon entry or exit.

5.2.4 Physics Setup

This section details the integration of heat transfer in porous media and fluid flow dynamics, focusing on turbulent flow. Heat transfer is modeled using the convection-diffusion equation, enhanced by thermodynamic properties averaging models that incorporate both the solid matrix and fluid properties. This ensures a comprehensive simulation of heat transfer phenomena, assuming temperature equilibrium within the porous matrix and fluid.

For fluid dynamics, the Reynolds-Averaged Navier-Stokes (RANS) equations are used to capture a wide range of flow behaviors and turbulence-induced phenomena. Wall functions are critical for accurately modeling turbulent flows near solid boundaries, balancing computational efficiency and accuracy in predicting wall-bounded turbulent flows (Dreeben & Pope, 1997).

5.2.4.1 Heat Transfer in Porous Media

This section outlines the simulation settings for different geological formations and the thermal behavior within the modeled salt cavern. The porous media approach is applied to the Röt-claystone and Soling-claystone formations, which are characterized by their porosity and permeability, essential for simulating heat transfer.

The Evaporite formation is modeled as a solid, non-porous medium due to its geological characteristics, indicating it lacks the porosity and permeability typical of porous media. This formation is treated as impervious, with no fluid flow or related heat transfer through pore spaces.

The brine within the system is confined to the cavern space. The initial temperature distribution in the surrounding formations is based on the geothermal gradient, using equation 10 :

$$\boldsymbol{T_z = T_{Surface} - (T_{Gradient} \times z)} \quad \text{(eq. 10)}$$

where T_z is the temperature at depth z, $T_{Surface}$ is the surface temperature (10°C), and $T_{Gradient}$ is the geothermal gradient (0.03°C/m). The cavern is initialized with a brine temperature of 40°C, assuming this as the starting condition for the injected brine.

Thermal insulation is applied to the outer walls, assuming no heat flux across the boundary, effectively isolating the system thermally. This condition focuses the simulation on internal heat transfer processes.

Tempearture and outflow boundary conditions are applied to the cavern's inlet and outlet to estimate heat flux through the boundaries and determine temperature changes due to fluid movement. This approach accurately models heat exchange from fluid flow, which is critical for the system's thermal dynamics.

5.2.4.2 *Fluid Dynamics (Fluid Flow)*

As stated earlier in chapter 4.4, that the flow regime will be calculated based on Reynolds number in order to apply the appropriate physics for the simulation. It is important to determine what characteristic length and velocity to choose for the Reynolds number calculation. Using the average velocity inside the tank and the tank height as the characteristic length aligns with the principles of dimensional analysis and fluid dynamics, as discussed in the Cradle CFD article. The logic involves selecting relevant parameters that accurately represent the flow conditions in the specific scenario being analyzed. Where in this case the flow is within the tank and directed vertically therefore the vertical extent over which the flow develops and interacts with the tank boundaries is taken as characteristic length and the average velocity inside the tank is taken as the characteristic velocity

$$Re = 11{,}000$$

Given that the average velocity is $2.4 * 10\text{^} - 4$ using the brine properties as specified in Table 4.

The Reynolds number is around 11,000 indicates a turbulent flow regime within the brine as it courses through the cavern. This regime characterizes a scenario where the forces arising from the fluid's inertia overpower the effects of viscosity.

Turbulent flow in the salt cavern is important for effective convective heat transfer. It enhances mixing, enabling efficient heat exchange between the brine and the cavern walls, thereby increasing heat transfer rates. This enhanced mixing also ensures a more uniform temperature distribution within the cavern, affecting the formation and stability of the thermocline, which separates warmer and cooler stored heat. The turbulent flow is simulated using the low Reynolds number k-epsilon (k-ε) model, with specialized wall treatment to capture near-wall effects accurately. Incompressible flow is assumed for the analysis, matching the expected physical conditions in the salt cavern

In the fluid flow configuration, the gravity consideration is activated by selecting the 'Include gravity' checkbox, which integrates buoyancy forces into the Navier–Stokes equations, enhancing the realism of the simulated fluid dynamics by accounting for density-driven flow components. With gravity included, the 'Use reduced pressure' setting is selected to adjust the pressure formulation from total pressure to reduced pressure, advantageous in systems where density variations are minimal. This setting is specifically applied within the cavern, the sole domain where fluid flow is considered. The fluid properties node incorporates the momentum and continuity equations required by the physics interface. For the turbulent flow setup, it additionally encompasses the turbulence transport equations, pivotal for capturing the complex dynamics of turbulent flows.

For the initial and boundary conditions, both the velocity field and pressure are initially set to zero, assuming a static fluid state at the beginning of the simulation. The default initial values for the turbulence model parameters—turbulent kinetic energy (k), turbulent dissipation rate (ε), and reciprocal wall distance (G)—are maintained. Boundary conditions include the no-slip condition applied to model the interaction between the fluid and solid walls, ensuring zero relative velocity at the boundary, which is crucial for stationary walls. The inlet is defined by a specified mass flow rate. To ensure a smooth transition from static to dynamic conditions and avoid inconsistencies, the flow rate is gradually increased from zero to 24 kg/s using a ramp function, as illustrated in Figure 15. **Outlet**: The outlet is defined by a specific pressure condition, which is strategically chosen instead of specifying the velocity vector at both the inlet and outlet to prevent convergence issues (*Outlet Comsol*, n.d.). This approach ensures a smooth outflow from the domain, avoiding any irregularities or disturbances in back-pressure that could affect the simulation's stability and accuracy.

5.2.4.3 Nonisothermal Flow multiphysics coupling

The Nonisothermal Flow multiphysics coupling is used in order to accurately simulate fluid flows where fluid properties are temperature-dependent. This coupling is particularly advantageous in scenarios where temperature changes significantly influence fluid flow. A comprehensive solution is provided by simultaneously solving the conservation equations for energy, mass, and momentum in both fluids and porous media, as well as energy conservation in solids.

The thermal and fluid dynamic aspects of the system are effectively integrated by the Nonisothermal Flow multiphysics interfaces, ensuring accurate representation of phenomena such as heat transfer coupled with fluid motion and the resultant changes in fluid properties due to temperature variations.

Material data evaluated at specific reference temperatures and pressures are utilized to capture essential thermal effects in the simulation. When gravity is included, the buoyancy forces are linearized with respect to temperature, making the simulation of buoyancy-driven flow more manageable while maintaining physical accuracyr

5.3 Mesh Generation

In CFD modeling, the volume is divided into numerous small cells or elements, which collectively form a mesh. Each cell in this mesh corresponds to a specific region where the flow is analyzed. The flow physics are then modeled by applying mathematical equations to each of these cells. Ensuring that the mesh is of high quality is vital for obtaining accurate results and maintaining the stability of the numerical calculations.

The worst non-inverting deformation of a mesh element is skewing, where angles deviate significantly from 90°, leading to reduced local accuracy and making equations harder to solve. Skewed elements often occur in boundary layer meshes, curved geometries, or when transitioning between different element types. Skewness is used to detect such distortions, and while there's no strict quality threshold, values below 0.01 should be avoided.

In CFD problems, the mesh contains the shape functions that represent the flow and pressure fields. Sharp gradients in these fields necessitate a denser mesh in specific areas to accurately capture the details. If these gradients are not adequately resolved, the numerical discretization scheme, such as stabilization or upwinding, may dissipate them, leading to reduced accuracy or

even causing oscillations and divergence. A smart approach to meshing involves strategically increasing mesh density where higher gradients are expected, rather than uniformly refining the mesh across the entire domain. A skilled fluid mechanics expert can anticipate these critical areas and apply finer meshing accordingly.

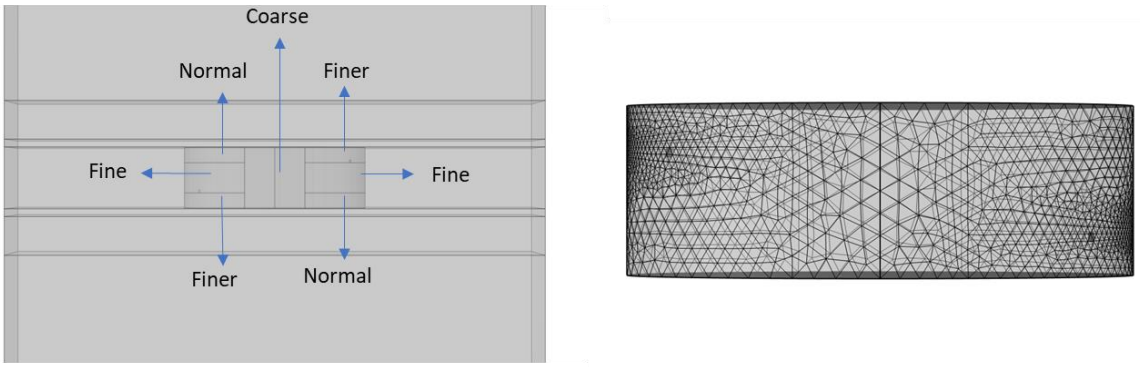

Figure 16: Mesh configuration showing varying densities, with finer mesh near the hot and cold wells to accurately capture high gradients, and coarser mesh in less critical areas for computational efficiency

As shown in figure 16, the mesh configuration for your CFD simulation is carefully designed to optimize both accuracy and computational efficiency by varying the element sizes across different regions of the domain. The mesh is made finer near the hot well and cold well, where temperature and pressure gradients are higher, with element sizes ranging from 1.18 m to 10.9 m. This targeted refinement ensures that the mesh can accurately capture the sharp changes in these critical areas, leading to more precise simulations of flow dynamics and heat transfer. A fine mesh setting, with element sizes between 2.96 m and 15.7 m, is used in regions requiring moderate detail, providing a balance between precision and computational cost. The normal mesh, with element sizes from 5.92 m to 19.8 m, is likely applied in areas where flow features are less critical, offering a reasonable trade-off between accuracy and computational load. Finally, a coarse mesh, with element sizes from 8.87 m to 29.6 m, is used in regions where fine detail is unnecessary, significantly reducing computational demands. This strategic variation in mesh density, with a total of 445,041 elements and an average element quality of 0.6831, ensures high accuracy where needed, while effectively managing overall computational resources. Despite the large number of elements, the minimum element quality of 0.141 indicates that the mesh maintains a reasonable standard, contributing to reliable and stable simulation results.

Table 6: Domain Element Statistics for the CFD Mesh Configuration, detailing the number of elements, minimum and average element quality, and the element volume ratio

Domain Element Statistics	Value
Number of elements	445041
Minimum element quality	0.141
Average element quality	0.6831
Element volume ratio	2.777E-8

In conclusion, this carefully designed mesh setup is crucial for ensuring the accuracy and reliability of the CFD simulations by precisely capturing the critical flow dynamics and thermal gradients within the salt cavern. The strategic variation in mesh density allows for a detailed and computationally efficient simulation, which is essential for obtaining meaningful results. To further validate the robustness of this mesh configuration, a mesh convergence study, demonstrating the impact of mesh refinement on the simulation outcomes, will be presented in Section 5.4.

5.4 Model Verification

Model validation is crucial for ensuring that a numerical model accurately represents real-world phenomena. Various methods are used, typically classified by the comparison pattern. One method is **validation using other numerical solutions**, which compares the model's results with those from previously validated numerical methods or multiple numerical methods solving the same problem. **Validation using analytical solutions** involves comparing simulation results with known analytical solutions, suitable for simple problems and useful for validating numerical method codes. **Validation using experimental results** compares model results with experimental measurements, demonstrating consistency with reality, though care is needed to match measurement configurations and simulations closely. **Validation using intermediate**

results involves comparing intermediate outcomes with known experimental or theoretical values, useful when final results are hard to measure directly, such as near-field measurements in electromagnetic simulations. Lastly, **validation using convergence** checks if the model's convergence behavior matches reference results, helpful when direct comparison patterns are unavailable, but not recommended as a final validation method due to uncertainty in guaranteeing convergence. Overall, validation fundamentally involves comparing results, often visually, supplemented by quantitative methods to ensure model accuracy and reliability.

In this study, the validation of the model is conducted using the method of validation through other numerical solutions, as described in “Cavern Thermal Energy Storage for District Cooling paper”(Alfasfos, n.d.). Given that experimental validation is not a feasible option at this time, this approach serves as the best available method to ensure the accuracy of the model. By comparing the results of the model under study with the results obtained from a previously validated numerical model, we can verify that the physics used in the model is correctly implemented and reliable. This method provides a robust alternative to experimental validation, ensuring the integrity of the simulation results.

The following steps were undertaken to verify the model: maintaining the same physics (e.g., fluid dynamics, thermal properties) as used in the reference model, adjusting the geometry to match the dimensions and configurations described in the paper, and altering the simulation time to align with the conditions presented in the paper. By carefully replicating these parameters, we ensured that our model closely followed the reference model's setup. Specific attention was given to ensuring that boundary conditions, initial conditions, and material properties were consistent with the reference model. Subsequently, we validated our results by comparing them with those obtained from the reference model, focusing on key output variables such as temperature distributions, velocity fields, and pressure profiles. The results from both models are presented in Figures 17 and 18, demonstrating a strong correlation between the two sets of data. This comparison confirmed the accuracy and reliability of our model's implementation, demonstrating that the physics were correctly applied. This approach provided a comprehensive validation method in the absence of feasible experimental options, ensuring confidence in the model's predictive capabilities.

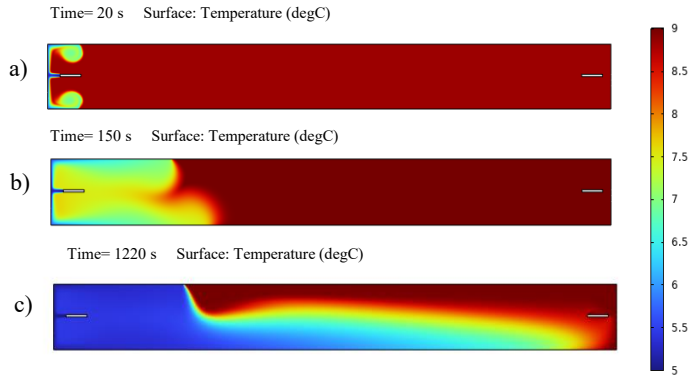

Figure 17: Temperature distribution over time for the verification scenario built to test the physics. The snapshots show temperature profiles at different times: (a) 20 seconds, (b) 150 seconds, and (c) 1220 seconds. The color scale indicates the temperature in degrees Celsius

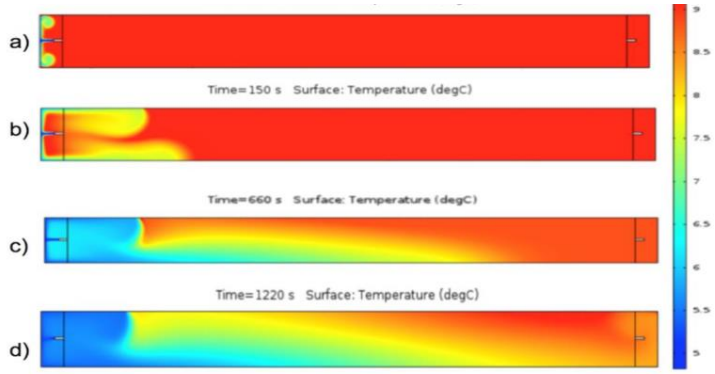

Figure 18: Temperature distribution over time from the reference paper used for validation. The snapshots show temperature profiles at different times: (a) 20 seconds, (b) 150 seconds, (c) 660 seconds, and (d) 1220 seconds. The color scale indicates the temperature in degrees Celsius

In this study one different physics will be added to the the validated physics is the addition of the kays-Crawford model based on the reasoning that was mentioned in chapter 4.4

Mesh Convergence Study

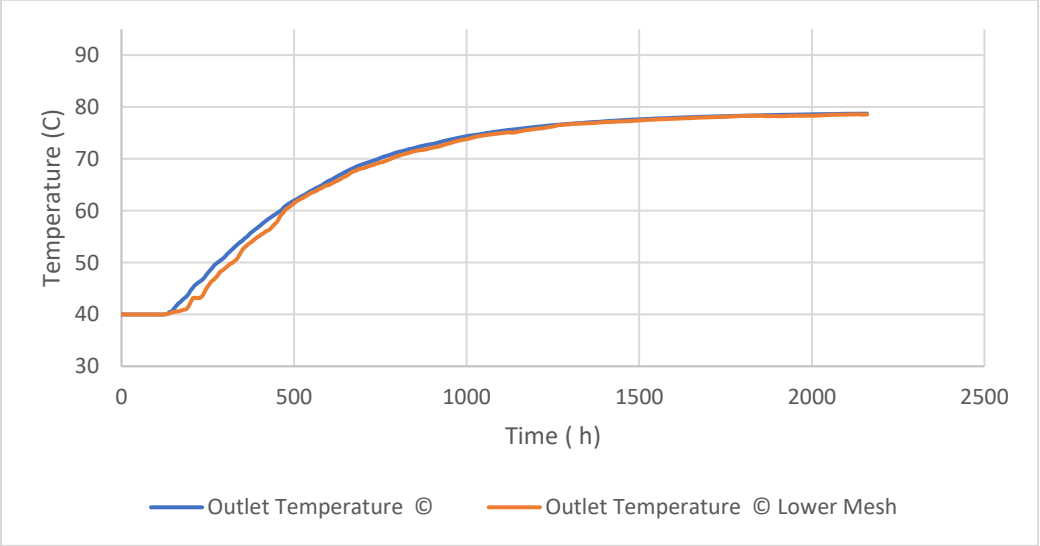

Figure 19: Outlet Temperature Over Time for Different Mesh Resolutions

Figure 20: Percentage Change in Outlet Temperature Between High and Low Mesh Resolutions

The provided figures (19&20) illustrate a mesh convergence study for evaluating outlet temperature in a thermal energy storage system. The top graph plots outlet temperature against

time for two different mesh configurations: a higher-resolution mesh (blue line) and a lower-resolution mesh (orange line). The temperature steadily increases from around 40°C, leveling off near 80°C after approximately 2000 hours. Initially, the temperature rise is steep (0 to about 500 hours), indicating active thermal energy storage. From 500 to 2000 hours, the curve flattens, suggesting the system is nearing thermal equilibrium. Both meshes show similar profiles with minor differences, indicating good mesh convergence. The bottom graph displays the percentage change in outlet temperature over time between the meshes. Initially, there are noticeable fluctuations, peaking at around 7%, due to the system's sensitivity to mesh resolution. After 500 hours, the percentage change stabilizes below 1%, with minimal fluctuations, showing that the difference between mesh resolutions becomes negligible as the system approaches equilibrium. From 1000 to 2500 hours, the percentage change remains consistently low, reinforcing that the mesh resolution has a minor impact on long-term temperature predictions. Thus, the study demonstrates that outlet temperature predictions are reliable across different mesh resolutions, affirming the adequacy of the current mesh settings for this analysis

Optimal Scenario Selection Process

The optimal configuration for maximizing thermal efficiency within the salt cavern system is determined through a systematic comparison of various key parameters, each evaluated against a base scenario. The process involves selecting the best-performing configuration in each category—temperature, flow rate, inlet position, cavern shape, and height-to-diameter (H/D) ratio—by comparing the thermal efficiency achieved in each scenario.

1. **Temperature Evaluation:**
    - The initial cavern temperature and injecting temperature are the first parameters to be evaluated. Scenarios with initial temperatures of 40°C and 50°C, combined with injecting temperatures of 70°C, 80°C, and 90°C, are compared to the base scenario (40/80).
    - The scenario that achieves the highest thermal efficiency in comparison to the base is selected as the optimal temperature configuration.
2. **Flow Rate Evaluation:**
    - Following the temperature evaluation, the selected optimal temperature configuration is used to assess different injection flow rates (100 m^3/h, 150 m^3/h, and 200 m^3/h).

- Each scenario's efficiency is compared to the base scenario's efficiency at 100 m^3/h. The flow rate yielding the highest thermal efficiency is selected.

3. **Inlet and Outlet Position Evaluation:**
    - The best temperature and flow rate configuration is then used to assess the impact of inlet and outlet positions. Vertical and horizontal configurations are compared.
    - The configuration that achieves the highest efficiency compared to the base scenario's vertical position is chosen.
4. **Cavern Shape Evaluation:**
    - With the optimal inlet/outlet position, the study then evaluates the impact of cavern shape (elliptical vs. circular).
    - The shape that enhances efficiency the most relative to the base elliptical configuration is selected.
5. **Height-to-Diameter (H/D) Ratio Evaluation:**
    - Finally, the study assesses different H/D ratios (0.3,1) using the best configurations identified in the previous steps.
    - The H/D ratio that provides the highest thermal efficiency is selected as the optimal configuration.

By systematically comparing each scenario to the base scenario, the optimal configuration for each category is selected. The overall best-performing scenario is identified based on the highest thermal efficiency achieved across all categories. Ideally, examining all possible combinations of these parameters would yield the most comprehensive understanding of optimal configurations. However, such an approach would be computationally intensive and beyond the practical scope of this study. Therefore, this systematic comparison provides a balanced approach to identifying the most efficient configuration without overwhelming computational demands.

5.4 Diana Model Set Up

In the context of thermal energy storage within salt caverns, understanding the geomechanical behavior of the surrounding rock formations is crucial to ensuring the long-term stability and safety of the system. This study employs DIANA FEA software to simulate subsidence, stress distribution, and salt creep within the Röt Evaporite formation. By incorporating temperature effects into the geomechanical model, we aim to provide a comprehensive assessment of the cavern's behavior under its utilization for heat storage purposes. This approach is designed to address Sub-Question 4 (SQ 4), which focuses on ensuring the safe operation of the cavern for thermal energy storage

Model Geometry

The geomechanical model in DIANA FEA was constructed using an existing model framework, which was adapted to incorporate the specific geological and operational parameters of this study. This existing model provided a solid foundation, enabling the transformation of required inputs for accurate simulation.

Figure 21 represents the 2D axisymmetric model constructed in Diana. The geometry and formation depths are consistent with those used in the COMSOL Multiphysics simulations. The model includes three primary formations: the Röt Claystone Formation (0-350m), the Röt Evaporite Formation (-350 to -450m), and the Soling Claystone Formation (-450 to -800m). The salt cavern is positioned with its roof at -380m, extending vertically for 40m, and horizontally with a radius of 60m.

While the formation depths and cavern dimensions mirror those used in the COMSOL model, a key difference lies in the cavern's shape. In DIANA, the cavern is modeled as cylindrical rather than elliptical, to avoid potential edge effects that could arise in the DIANA simulation environment. This adjustment ensures the geomechanical model can accurately simulate subsidence, stress distribution, and other critical behaviors without introducing artifacts related to cavern geometry.

The model simulations were performed assuming a constant pressure, reflecting the equal injection and production rate. Additionally, a surface temperature of 10°C and a fixed geothermal gradient of 0.034°C/m were applied, replicating the same conditions used in the thermal modeling conducted in DIANA as well. This consistency in thermal conditions across models ensures the results are comparable and accurately reflect the real-world scenario.

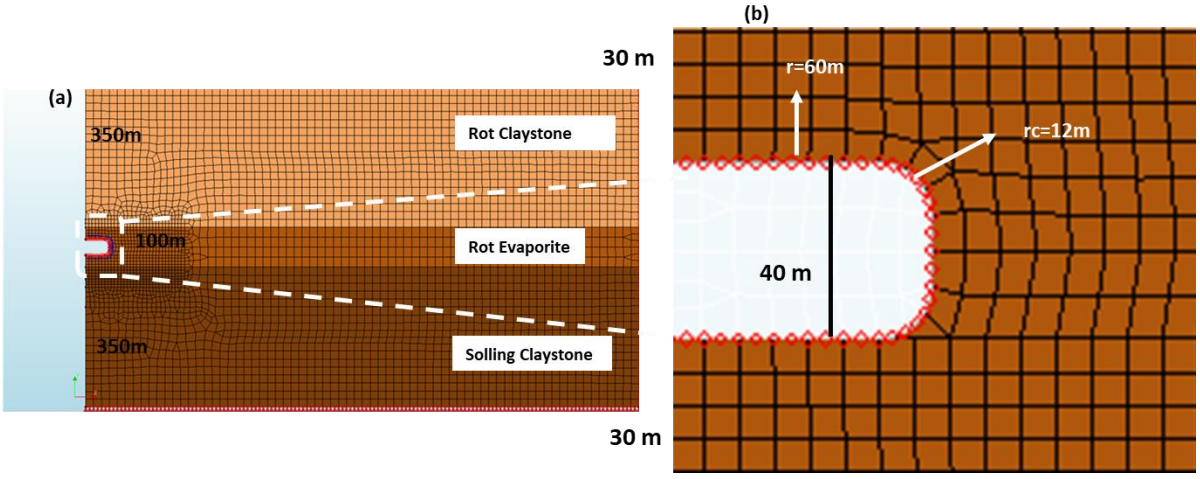

Figure 21: Geomechanical Model Setup in DIANA FEA: The left panel illustrates the axisymmetric model of the salt cavern within the geological formations, including the Röt Claystone, Röt Evaporite, and Soling Claystone layers. The right panel provides a detailed view of the cavern geometry, showing the cavern's radius (r=60m) and its roof curvature radius (rc=12m). The mesh is refined near the cavern boundaries to accurately capture stress concentrations and deformation patterns within the surrounding rock formations

Material parameters

To accurately simulate the geomechanical behavior of the salt cavern and surrounding formations, it is essential to define the material parameters for each geological layer. These parameters play a critical role in determining how the rock formations will respond to stress, temperature changes, and other operational conditions within the cavern. In this section, we outline the material properties used in the DIANA FEA model, drawing from available data and making informed assumptions where direct measurements are not available.

Since no direct rock mechanical data exist for the Röt Salt formation from laboratory experiments. However, extensive data is available for the Zechstein salt from various locations around the Netherlands. Typical values have been provided in the table below, but it is important to note that the creep rate parameters (A1, A2) can vary significantly between different salt formations. The values selected here correspond to lab data from two locations:

Zuidwending and Barradeel. Given the lack of specific data for the Röt Salt, these typical values have been used as a proxy.

For the mechanical properties of the Röt and Soling claystone formations, no specific data was found in the literature. Therefore, average values for the Young's modulus of claystone have been applied to ensure a reasonable approximation of their mechanical behavior in the model.

Cavern Lifecycle Simulation Phases

For the model lifecycle set up three phases are modelled (Table x): (1) the cavern construction phase (1.5 y), where the cavern pressure is changed linearly in time from lithostatic to hemostatic, simulating leaching of the cavity; (2) the brine production phase (7.5y), with constant hemostatic pressure (3) the cavern utilization phase (30y), where brine pressure is set constant. The injection and standby period assumes a temperature inside the cavern at (80C) for 180 days followed by a production period with brine temperature at (40C) for 90 days and that is done for a total of 42 cycles during the 30 years of utilization.

Table 7: This table details the lifecycle of a salt cavern, highlighting the phases of construction, sealing, and operational cycles, along with corresponding pressure conditions and temperature ranges throughout the process

Lifecycle Phases Of The Salt Cavern	Start/End	Cavern Pressure	Temperature (K)
Cavern Construction	0-548	Lithostatic-Halmostatic	313
Sealed	548-3285	Halmostatic	313
Cycles	3285-14350	Halmostatic	313/353

6. Results

This chapter presents the comprehensive findings from the simulations conducted to assess the thermal performance and structural safety of salt caverns utilized for energy storage. Utilizing advanced modeling tools, COMSOL Multiphysics and DIANA FEA, this research examines the effects of various operational parameters on the efficiency of heat storage and the geomechanical stability of the caverns. The results are segmented into two main sections: thermal efficiency outcomes and geomechanical safety assessments

6.1 Thermal Efficiency Analysis

6.1.1 Temperature Distribution in the Cavern

Figure 22 below depicts the progression of heat distribution within a salt cavern used for thermal energy storage, as visualized through a series of temperature and heat flux maps over a 30-day period. Initially, the temperature within the cavern is uniformly set at 40°C, with minimal heat flux as indicated by subdued arrow vectors. As heat is injected over the days, distinct patterns emerge:

1. **At 0 Hours (Top Left):** The uniform temperature of 40°C and minimal heat flux suggest stable initial conditions without active thermal gradients.
2. **At 3 Days (Top Right):** Temperature rises near the injection point, and pronounced heat flux vectors at the cavern's periphery indicate the onset of heat propagation. The formation of streamlines suggests convective currents are beginning to facilitate heat transfer within the cavern.
3. **At 10 Days (Bottom Left):** A visible temperature gradient develops, with warmer areas near the injection site. Complex streamlines and more active heat flux vectors along the boundaries illustrate an increase in convective activity and heat transfer to the surrounding rock.

At 30 Days (Bottom Right): The cavern shows a more uniform temperature distribution at elevated levels, indicating thermal stabilization. Convection appears to slow, suggesting the

system is nearing thermal equilibrium. Heat flux vectors are evenly distributed, signifying uniform heat conduction to the surrounding rock.

These images collectively highlight the dynamic process of heat distribution within the cavern, from initial stability, through active convection and heat transfer, to near equilibrium. The visualizations provide valuable insights into the thermal behavior of salt caverns during energy storage operations, underscoring the effectiveness of using convective currents and thermal gradients in managing heat distribution over time.

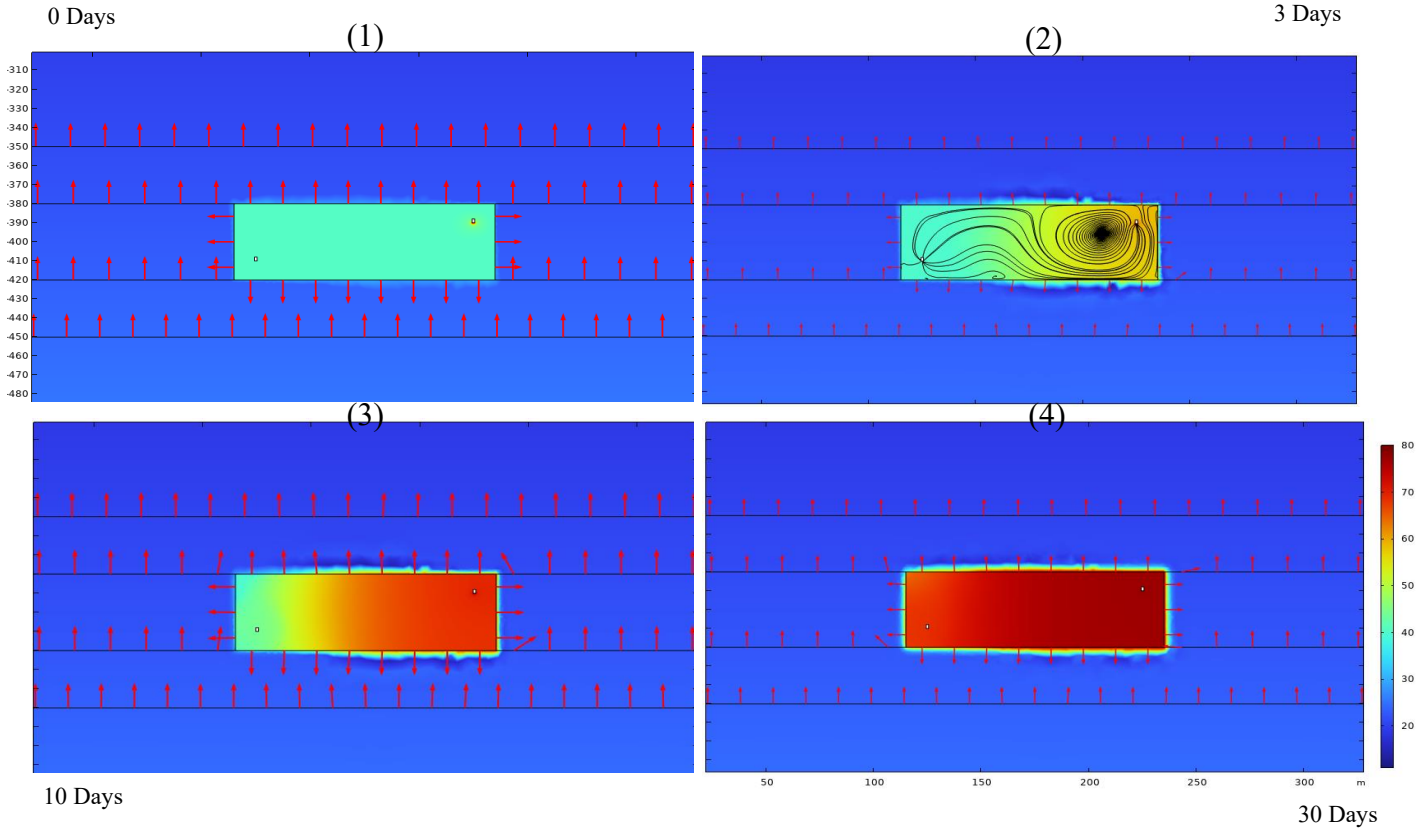

Figure 22: 2D XZ cross-sections of the salt cavern during the injection phase, showing heat propagation, streamlines, and heat flux vectors at four different time steps: (1) 0 hours, (2) 3 days, (3) 10 days, and (4) 30 days. The images illustrate the development of the thermal field within the cavern, with streamlines indicating the direction of heat flow and arrows

Figure 23 illustrates the temperature distribution and convective flow patterns within a salt cavern during different phases of thermal energy storage and extraction. The sequence of thermal images showcases how the internal conditions of the cavern evolve over time, highlighting the dynamic nature of heat storage and retrieval processes.

1. **At the Start of the Standby Phase (Top Left):** Initially, the temperature distribution within the cavern is uniform, with well-defined, organized streamline patterns indicative of stable internal convection currents. This setup helps maintain thermal equilibrium, with heat largely retained within the cavern as indicated by subdued heat flux vectors.
2. **At the End of the Standby Phase (Top Right):** The temperature remains fairly consistent across the cavern, although the convective currents have slightly weakened. This reduction in internal circulation suggests that the system is nearing a state of thermal equilibrium. The heat flux vectors remain present but less active, reflecting the cavern's stability with minimal heat loss to the external environment.
3. **Three Days into the Production Phase (Bottom Left):** As heat extraction commences, the internal temperature starts to vary, particularly near the reinjection points of colder water, enhancing convective activity. The resulting complex streamline patterns show intensified movement of heat towards these cooler areas. Heat flux vectors become more pronounced around the cavern walls, indicating increased heat transfer to the surrounding rock as the system adjusts to the removal of heat.
4. **One Month into the Production Phase (Bottom Right):** The temperature distribution becomes increasingly non-uniform, displaying a clear gradient from the warmer areas near the residual heat to the cooler areas near the extraction points. Although convective currents continue to facilitate heat transfer within the cavern, their focus shifts towards aiding heat delivery to the extraction points. The heat flux vectors, while still noticeable, show a decline in intensity, suggesting that the temperature difference between the cavern and its surroundings is decreasing as the system progressively stabilizes after prolonged heat extraction.

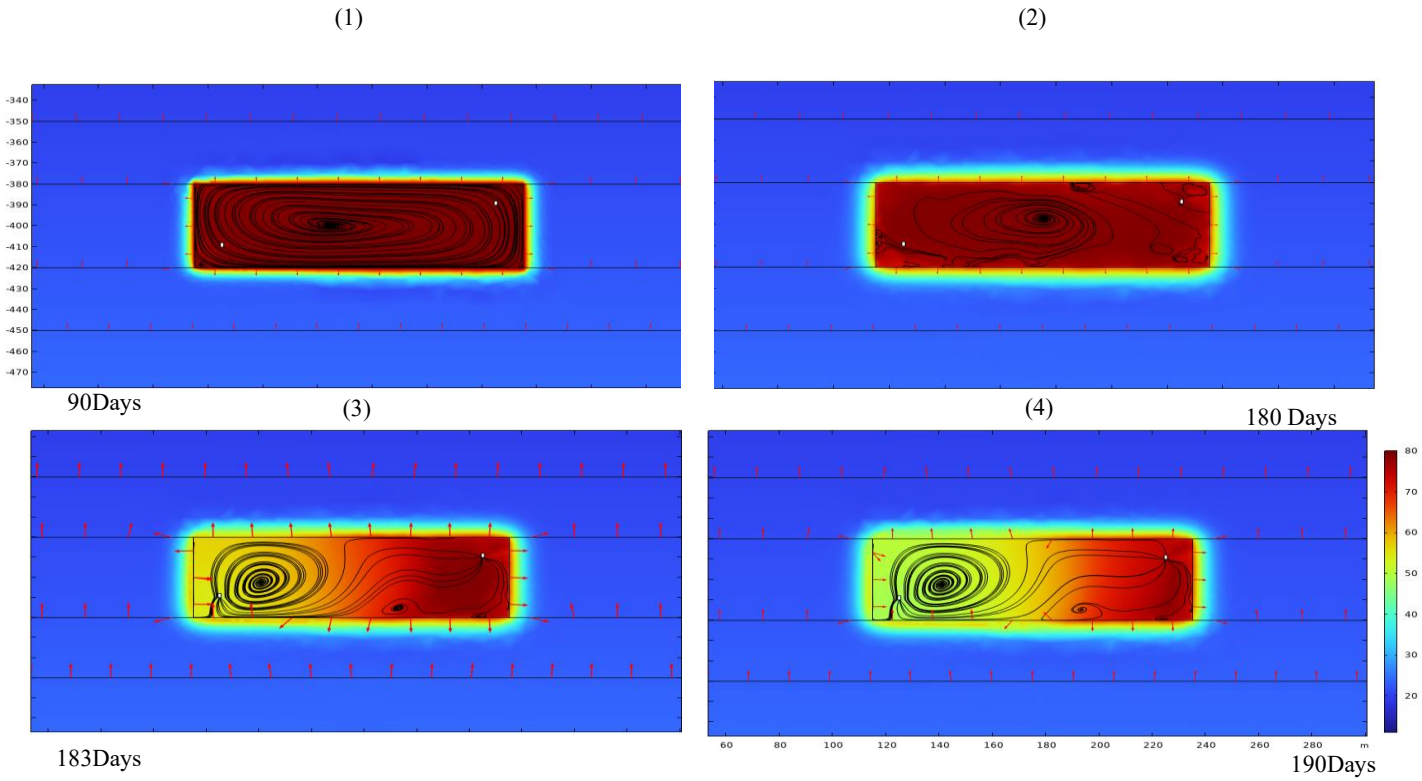

Figure 93: Temperature distribution and streamline patterns in the salt cavern during different phases. Images 1 and 2 illustrate the temperature and convective flow at the start and end of the standby phase, respectively. Images 3 and 4 depict the conditions 3 days and 1 month after the production phase has begun, showing the evolution of heat propagation and internal convection over time.

6.1.2 Operational Phase Analysis and Temperature Dynamics in Salt Cavern Thermal Storage: HotWell and ColdWell Perspectives

In this analysis, the temperature profiles of both the HotWell and ColdWell are examined across three distinct operational phases: the **injection phase (0-2160 hours)**, where heat is injected into the system; the **standby phase (2160-4320 hours)**, where the system is monitored for heat retention without active injection; and the **production phase (4320-6480 hours)**, where stored heat is extracted from the system. In this setup, the ColdWell is located at the bottom of the system, while the HotWell is positioned at the top. During the injection phase, heat is injected into the system from the top (HotWell) and distributed downward, while in the production phase, heat is extracted from the top (HotWell), and cooler water is injected at the bottom (ColdWell). The temperature plots are categorized based on different operational parameters, such as Delta T and initial temperature, and are compared to a base scenario (40°C initial, 80°C injecting temperature).

The analysis focuses on several key aspects:

1. **Heat-Up Rate:** How quickly the system heats up during the injection phase.
2. **Time to Plateau:** How long it takes for the temperature to stabilize, either reaching a plateau or approaching an asymptotic value.
3. **Heat Discharge Efficiency:** How effectively the system discharges heat during the production phase.
4. **Temperature Stability During Standby Phase:** How stable the temperature remains during the standby phase, indicating the effectiveness of thermal retention.
5. **Influence of Initial Temperature:** The impact of initial temperature on heat retention and discharge efficiency, with higher initial temperatures enhancing storage but potentially leading to faster energy depletion.
6. **Scenario Comparison:** Assessing the overall performance of different scenarios to identify which provides the best balance between heat storage, retention, and discharge.

These aspects are crucial for evaluating the thermal efficiency and overall performance of the storage system under varying operational conditions, providing insights into optimizing the system for different applications

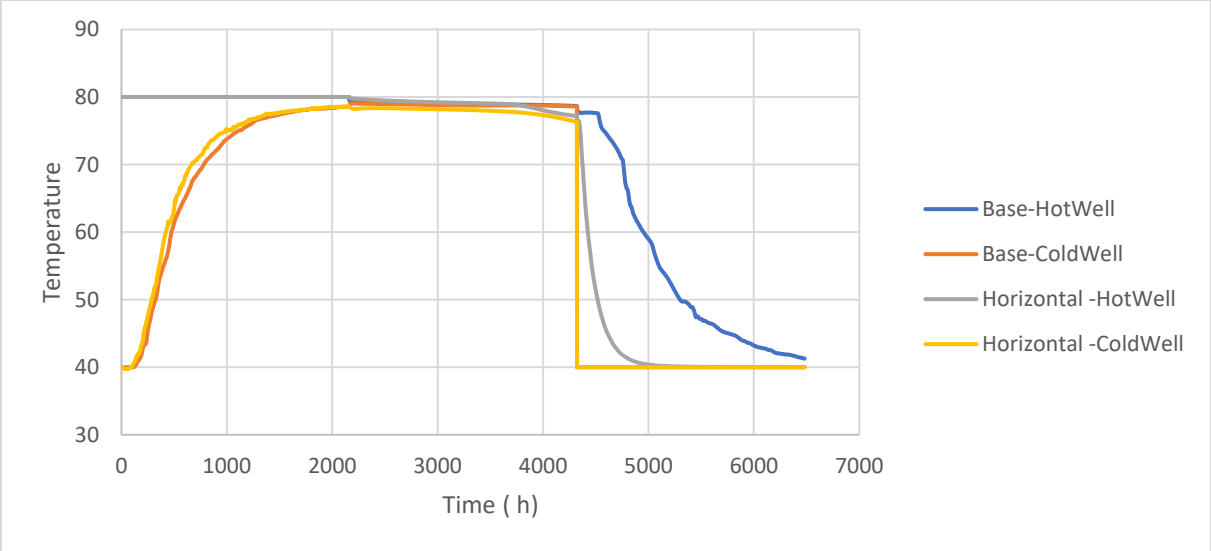

Figure 24: Temperature Profiles in Horizontal Well Scenario

The comparison between the vertical and horizontal flow direction scenarios reveals that both configurations perform similarly in terms of heat-up rate, time to reach a stable temperature

plateau, and temperature stability during the standby phase, indicating that flow direction does not significantly affect these aspects of thermal performance. However, during the production phase, the horizontal flow direction scenario exhibits a much faster temperature decline, leading to rapid energy depletion compared to the vertical flow direction. Notably, the production profile for the horizontal flow direction shows an unexpected and significant drop, suggesting that this configuration may not be effectively managing heat discharge. This unusual behavior may be due to a numerical error in the simulation run, indicating the need for re-running the simulation with a tighter mesh and lower error tolerance. As a result, the horizontal flow direction scenario will be excluded from further analysis until a more reliable simulation can be conducted. Meanwhile, the vertical flow direction is considered more suitable for applications requiring sustained heat output.

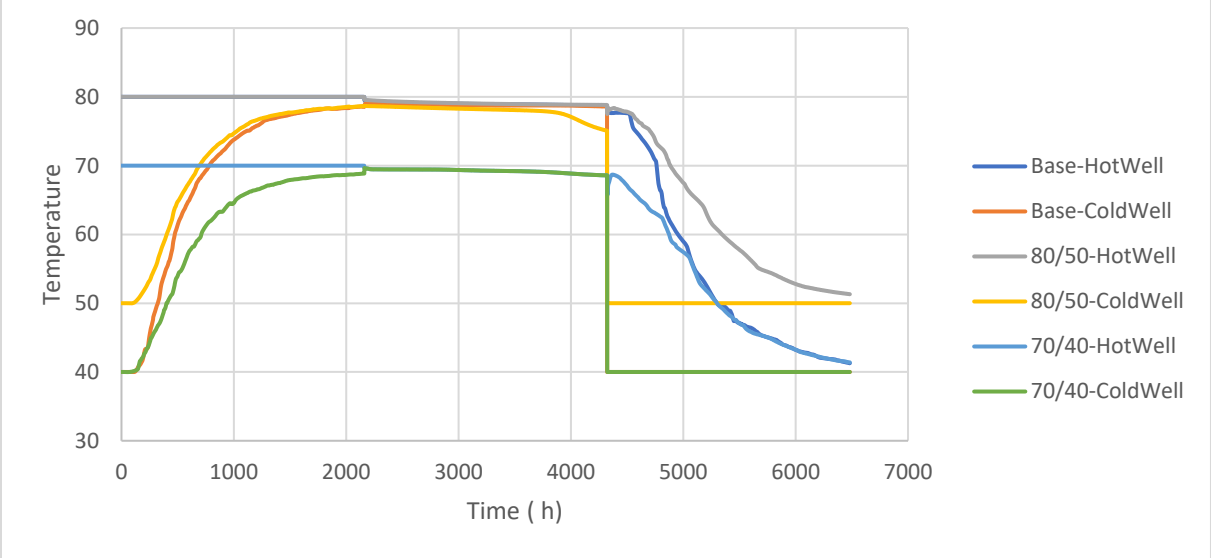

Figure 25: Temperature Profiles in Delta (3) Scenarios

The analysis of the Delta T (30°C) scenarios reveals distinct differences between the **70/40-HotWell** and **80/50-HotWell** configurations. The **80/50-HotWell** scenario exhibits a rapid heat-up rate, quickly stabilizing at a high temperature due to its higher initial temperature. However, it also results in faster heat depletion during the production phase, indicating that while it efficiently stores heat, it may not sustain energy output as effectively over longer periods. Notably, the temperature at the ColdWell in this scenario is slightly lower, suggesting that the lower section of the system, where the ColdWell is located, remains cooler—an effect not observed in the other scenarios. This could imply the presence of vertical temperature gradients, with potential implications for the overall thermal efficiency of the system. In contrast, the **70/40-HotWell** scenario shows a slower heat-up rate and takes longer to reach

stability, reflecting the challenges of a smaller Delta T in achieving quick thermal equilibrium. This scenario also discharges heat more slowly, resulting in lower overall energy output, but it may be preferable in situations requiring gradual heat release.

When comparing these scenarios to the base/reference scenario (**Base-HotWell, 80/40**), the base scenario provides a balanced performance across all phases, with moderate heat-up, stable retention, and controlled discharge. The **80/50-HotWell** scenario, while excelling in rapid storage and retention, sacrifices longer-term efficiency during extraction compared to the base scenario, possibly due to the observed cooler conditions at the ColdWell. Meanwhile, the **70/40-HotWell** scenario, although less efficient overall, may be suited for applications where a slower and steadier thermal response is desired. This comparative analysis underscores the importance of optimizing initial temperatures and Delta T values to align with specific operational goals, whether the priority is rapid energy storage, sustained output, or balanced thermal management

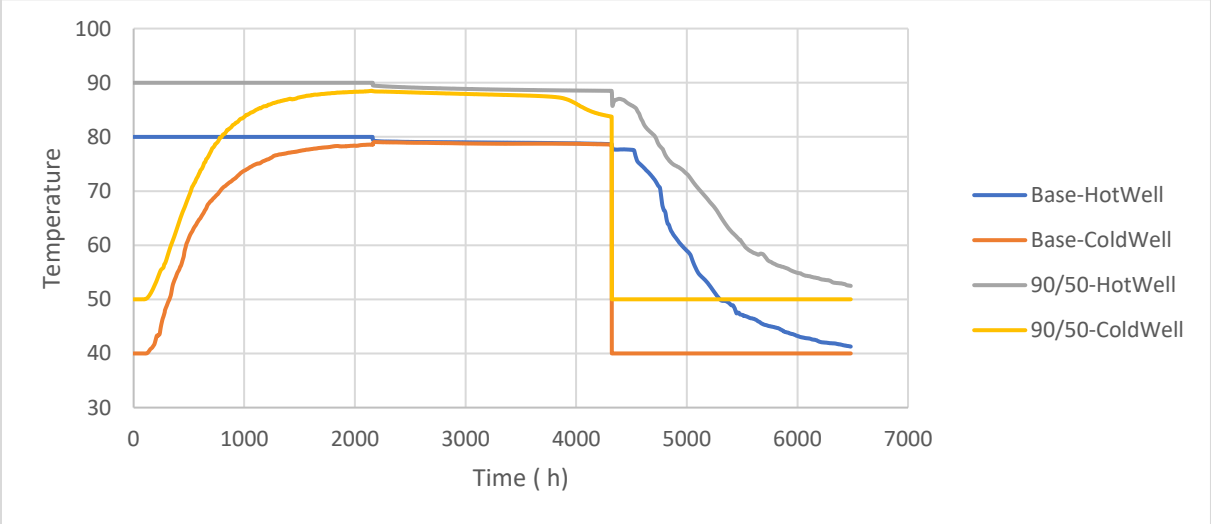

Figure 26: Temperature Profiles in Delta T (40) Scenarios

The analysis of the Delta T (40°C) scenarios, specifically comparing the **Base-HotWell (80/40°C)** and **90/50-HotWell** configurations, highlights distinct thermal performance patterns, particularly in how the system responds to higher initial and injecting temperatures.

The **90/50-HotWell** scenario shows a rapid heat-up rate, quickly reaching a high temperature near 90°C due to its higher temperature settings. This scenario stabilizes efficiently during the injection phase but exhibits a slightly lower temperature at the ColdWell compared to the HotWell, indicating that the lower section of the system remains cooler. This effect, more

pronounced than in the Delta T (30°C) scenario, suggests the presence of vertical temperature gradients, which could impact the system's overall thermal efficiency, particularly in retaining and distributing heat during the standby and production phases.

In contrast, the **Base-HotWell (80/40°C)** scenario, which has already been established as a stable and balanced performer in the Delta T (30°C) analysis, continues to provide consistent heat-up, retention, and discharge behaviors. While the **90/50-HotWell** scenario initially performs well, its higher thermal gradient leads to a quicker depletion of stored energy during the production phase, with the ColdWell showing a more rapid decline. This faster depletion may limit its effectiveness in applications requiring prolonged heat discharge, despite its initial efficiency.

Overall, the **Base-HotWell (80/40°C)** scenario remains a reliable reference point for balanced thermal management, while the **90/50-HotWell** scenario highlights the trade-offs involved in using higher initial temperatures and larger Delta T values. This comparison underscores the importance of selecting the appropriate thermal configurations based on specific operational needs, with the **Base-HotWell** serving as a steady benchmark against which the impacts of higher temperature settings are measured.

For both the Delta T (30°C) and Delta T (40°C) analyses are consistent in terms of the observed performance patterns. The higher initial temperature scenarios (80/50 for Delta T 30°C and 90/50 for Delta T 40°C) both lead to rapid heat absorption but also quicker heat depletion, with potential issues related to vertical temperature gradients. The **Base-HotWell (80/40°C)** scenario remains a reliable and balanced option across both analyses, providing steady thermal management without the pronounced depletion seen in the higher initial temperature scenarios. This consistency reinforces the findings and highlights the trade-offs involved in optimizing thermal storage systems for different operational needs.

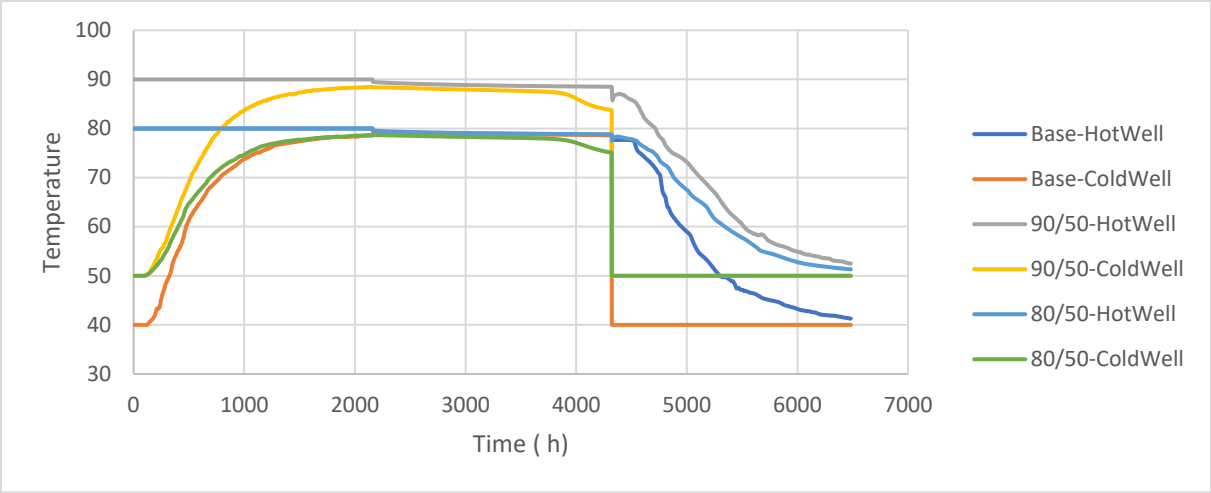

Figure 27: Temperature Profiles in Initiall (T) 50C Scenarios

The comparison of the **Base-HotWell (80/40°C)** and **90/50-HotWell** scenarios, both with an initial temperature of 50°C, provides valuable insights into the impact of different Delta T values on thermal performance across the injection, standby, and production phases.

The **90/50-HotWell** scenario, characterized by a higher Delta T, exhibits a rapid heat-up rate, quickly reaching its peak temperature near 90°C. This efficiency in heat absorption and storage during the injection phase highlights the advantages of a larger Delta T. However, the slightly lower temperature observed at the ColdWell suggests cooler conditions at the lower section of the system, indicating that a larger Delta T may lead to more pronounced vertical temperature gradients. These gradients could potentially affect the uniformity of heat distribution and overall thermal efficiency, particularly during the standby and production phases.

In contrast, the **80/50-HotWell** scenario, with a smaller Delta T, heats up more gradually and stabilizes at a lower temperature around 80°C. This scenario demonstrates a more balanced thermal profile, with closer temperature alignment between the HotWell and ColdWell, suggesting more uniform heat distribution and better thermal management across the system.

The **Base-HotWell (80/40°C)** scenario, serving as a consistent reference point, provides moderate heat-up rates and stable temperature retention. During the production phase, the **90/50-HotWell** scenario experiences a faster decline in temperature, likely due to the higher thermal gradient causing quicker depletion of stored energy. The ColdWell also declines more rapidly, reflecting less effective heat retention. This behavior is typical of higher Delta T scenarios, where initial heat storage efficiency does not necessarily translate into sustained heat output.

Conversely, the **80/50-HotWell** scenario maintains a more controlled and steady temperature decline during the production phase, with the ColdWell's temperature remaining closer to that of the HotWell. Despite its lower peak temperature, this scenario provides more consistent and sustainable heat output, making it suitable for applications requiring steady thermal management without the rapid depletion seen in larger Delta T configurations.

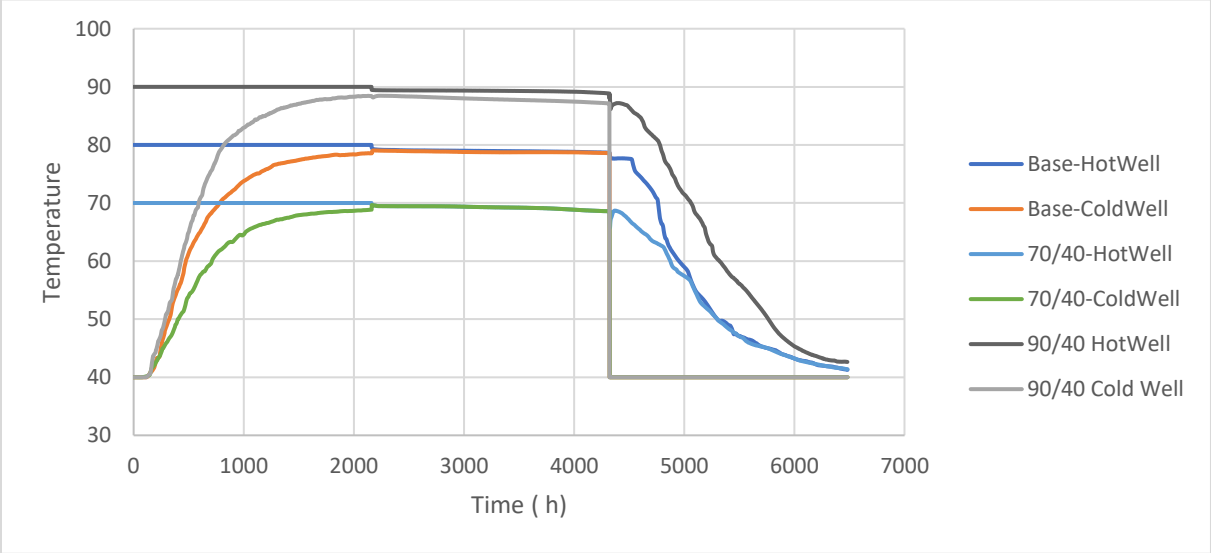

Figure *28:* Temperature Profiles in Initiall (T) 40C Scenarios

The comparison of the **70/40-HotWell**, **80/40-HotWell (Base)**, and **90/40-HotWell** scenarios, all with an initial temperature of 40°C, reveals that higher injecting temperatures lead to faster heat-up rates and quicker stabilization during the injection phase. The **90/40-HotWell** scenario reaches the highest temperature and stabilizes the fastest, followed by the **80/40-HotWell** and **70/40-HotWell** scenarios. However, during the production phase, the **90/40-HotWell** scenario also experiences the most rapid temperature decline, indicating quicker energy depletion, while the **70/40-HotWell** scenario shows a more gradual temperature drop, suggesting steadier energy output. The **80/40-HotWell (Base)** scenario provides a balanced performance, with moderate heat-up and steady discharge. This analysis highlights how increasing the injecting temperature enhances initial thermal performance but may lead to faster energy depletion.

The analysis of temperature scenarios, varying both Delta T and initial injecting temperatures, reveals important trade-offs in thermal performance. As the injecting temperature increases, as seen in the **90/50-HotWell** and **90/40-HotWell** scenarios, the system demonstrates a rapid heat-up rate and quickly reaches a high peak temperature, leading to efficient initial heat

absorption. However, these scenarios also face challenges during the production phase, where the stored heat is depleted more rapidly, indicating a quicker energy output that may not be sustainable for long-term applications.

In contrast, scenarios with moderate injecting temperatures, such as **80/50-HotWell** and **Base-HotWell (80/40°C)**, show a more balanced performance. These scenarios achieve stable temperatures efficiently while also maintaining more consistent heat distribution and a steady decline during the production phase, making them well-suited for applications requiring a balance between rapid heat absorption and sustained energy release.

Lower temperature scenarios, like **70/40-HotWell**, exhibit slower heat-up rates and take longer to stabilize. However, they offer the advantage of more gradual and sustained energy output during the production phase, making them ideal for applications where long-term thermal stability is prioritized.

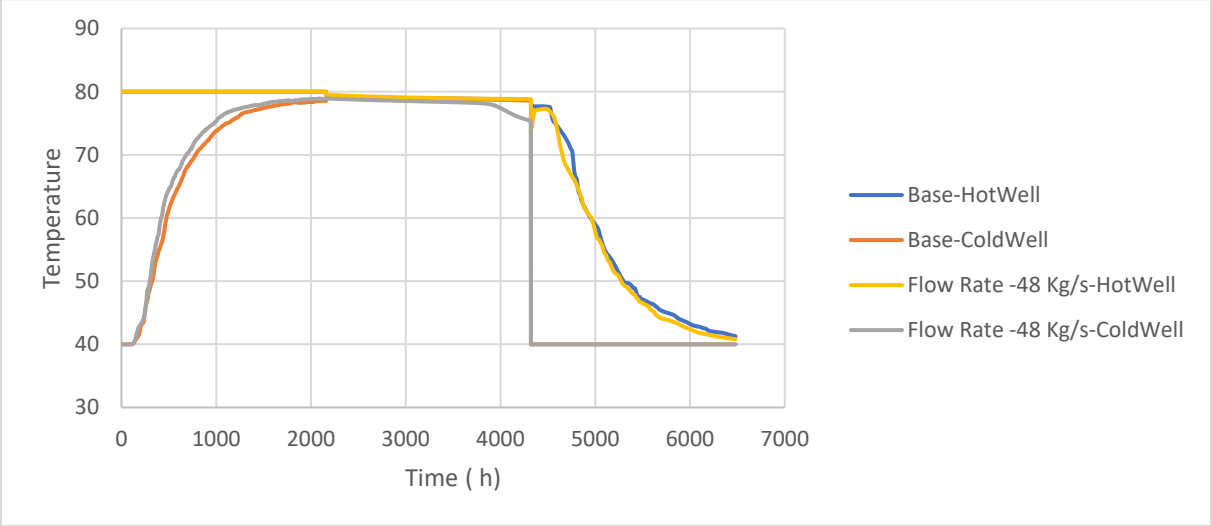

Figure 29: Temperature Profiles For 48Kg/s Scenario vs Base Scenario

The comparison between the **Base-HotWell (80/40°C)** scenario and the higher flow rate scenario shows that increasing the flow rate had a minimal impact on overall thermal performance. While there was a slight improvement in the heat-up rate and uniformity of heat distribution, the time to reach the plateau and the rate of temperature decline during the production phase remained largely unaffected. Both scenarios demonstrated similar temperature stability during the standby phase, indicating that the increased flow rate did not significantly influence the system's long-term thermal behavior. This suggests that, under these

conditions, the flow rate does not play a critical role in altering the thermal efficiency of the system.

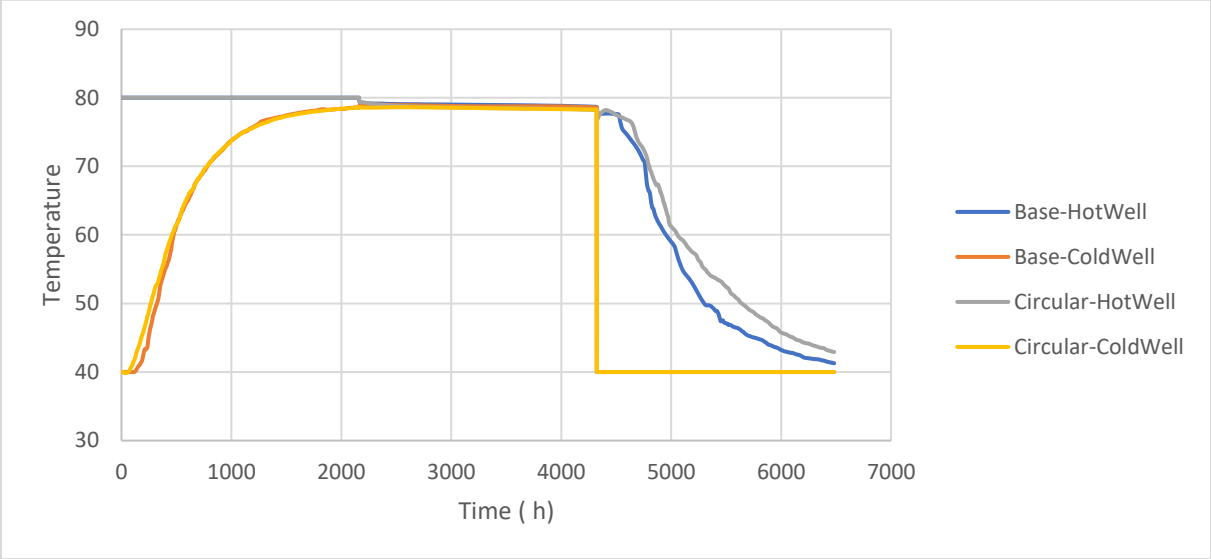

Figure 30: Temperature Profiles for Circular Shape Scenario vs Base Scenario

The comparison between the elliptical (Base-HotWell) and circular cavern shapes indicates that the circular shape has a slight advantage in thermal performance. The circular shape shows a faster heat-up rate during the injection phase, reaching the target temperature more quickly than the elliptical shape. During the standby phase, the circular shape also retains heat more effectively, maintaining higher temperatures throughout the phase. In the production phase, the circular cavern exhibits a more gradual decline in temperature, indicating better heat retention and a more controlled release of stored energy compared to the elliptical shape, which shows a quicker temperature drop. This suggests that the circular shape may be more effective in maintaining thermal efficiency and ensuring a steadier energy output over time.

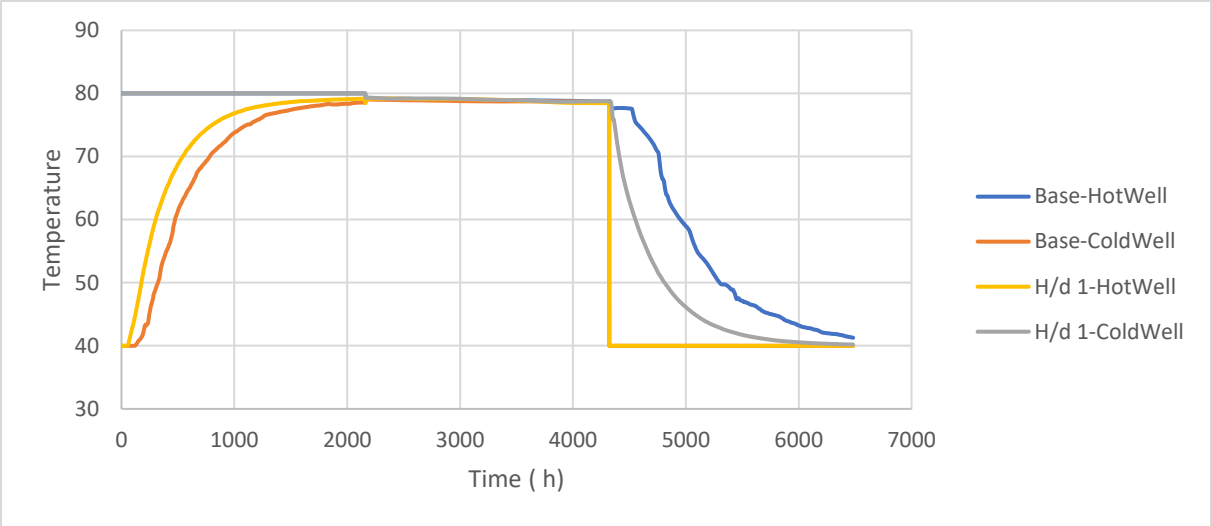

Figure 31: Temperature Profiles in H/d 1 vs Base Scenario

The comparison between the base scenario with an H/D ratio of 0.3 and the scenario with a higher H/D ratio of 1 shows that the higher H/D ratio not only leads to a quicker heat-up during the injection phase but also reaches a higher temperature and stabilizes at that temperature more quickly. However, this comes at the cost of a faster temperature drop during the production phase, indicating that the stored heat is depleted more rapidly. In contrast, the lower H/D ratio (0.3) results in better heat retention and a more gradual release of energy.

6.1.3 Thermal Efficiencies

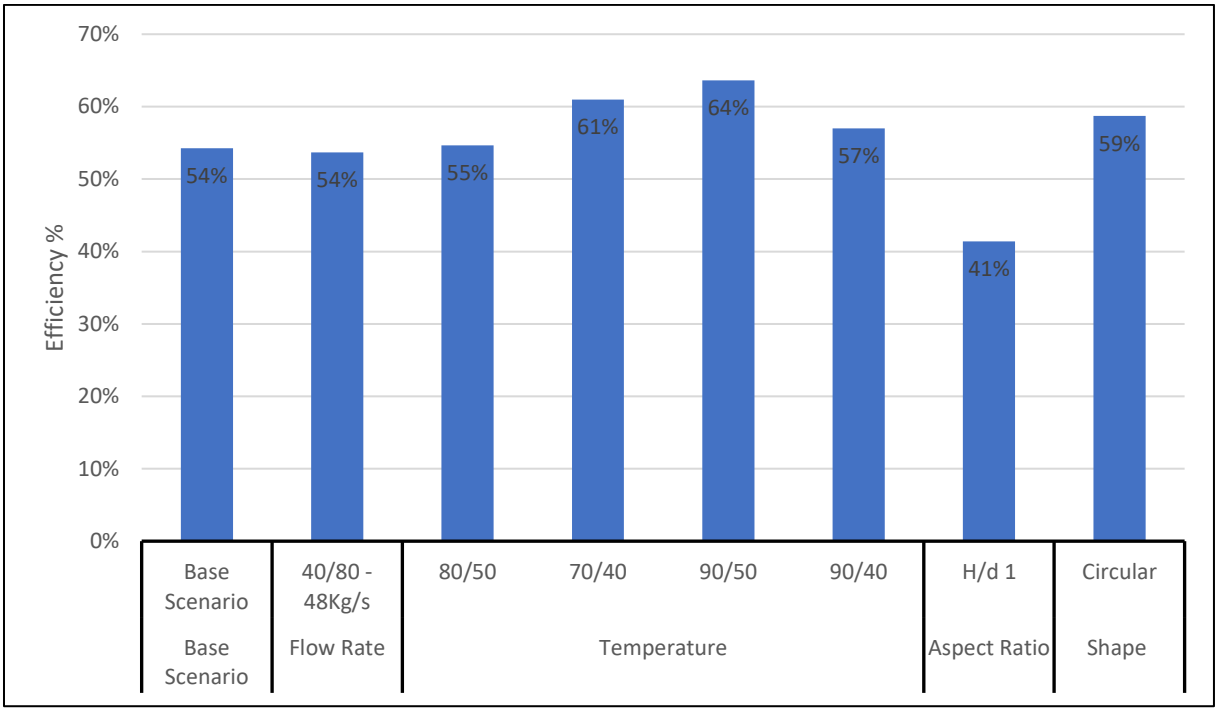

Figure 32: Efficiency of Various Operational Scenarios in Salt Cavern Thermal Storage

This graph compares the thermal efficiency of different operational scenarios within a salt cavern. The base scenario serves as a benchmark at 54% efficiency. Adjustments in flow rate, temperature settings, aspect ratio, and cavern shape illustrate their impact on thermal performance, with temperature variations showing the most significant effect, particularly in the 70/40 and 90/50 scenarios, achieving efficiencies of 61% and 64% respectively.

Flow Rate: The scenario with an increased flow rate (48 kg/s) maintains the same efficiency as the base scenario at 54%. This indicates that changing the flow rate does not have a significant impact on thermal efficiency under the tested conditions. The results suggest that within the tested range, adjustments in flow rate alone are not a significant factor for improving thermal efficiency.

Temperature

Temperature differentials significantly affect the efficiency of thermal storage systems. The scenarios analyzed demonstrate the following:

80/50 Scenario: Efficiency improves slightly to 55%, indicating that even a modest increase in ΔT can yield better results than the base scenario (54%).

70/40 Scenario: A substantial increase in efficiency to 61% is observed, suggesting that this combination of initial and injecting temperatures is particularly effective.

90/50 Scenario: This scenario achieves the highest efficiency at 64%, underscoring the importance of a larger ΔT for enhancing thermal performance.

90/40 Scenario: Efficiency decreases to 57%, indicating that while higher injecting temperatures generally improve efficiency, there may be diminishing returns or other factors that limit further gains when the differential is too large.

When comparing scenarios based on their initial temperatures, two sets of scenarios were analyzed:

Set 1: Initial Temperature of 50°C (80/50, 90/50):

Efficiency: 55% (80/50) and 64% (90/50)

Average Efficiency: 59.5%

Set 2: Initial Temperature of 40°C (70/40, 80/40, 90/40):

Efficiency: 61% (70/40), 57% (80/40), and 57% (90/40)

Average Efficiency: 58.33%

The set with an initial temperature of 50°C shows a slightly higher average efficiency (59.5%) compared to the set with an initial temperature of 40°C (58.33%). This suggests that higher initial temperatures generally lead to better thermal efficiency in these scenarios.

Comparison of Scenarios Based on Delta T (ΔT)

Two sets of scenarios were also compared based on their ΔT values:

Set 3: ΔT = 30°C (80/50, 70/40):

Efficiency: 55% (80/50) and 61% (70/40)

Average Efficiency: 58%

Set 4: ΔT = 40°C (80/40, 90/50):

Efficiency: 57% (80/40) and 64% (90/50)

Average Efficiency: 60.5%

The set with a ΔT of 40°C demonstrates a higher average efficiency (60.5%) compared to the set with a ΔT of 30°C (58%). This finding indicates that a larger ΔT is more beneficial for maximizing thermal efficiency.

Initial Temperature Impact: Comparing scenarios with initial temperatures of 50°C and 40°C shows that a higher initial temperature results in slightly better efficiency (59.5% vs. 58.33%). Therefore, higher initial temperatures should be considered when designing thermal storage systems for improved performance.

Delta T (ΔT) Impact: When comparing ΔT values of 30°C and 40°C, the higher ΔT yields better efficiency (60.5% vs. 58%). This reinforces the importance of optimizing the temperature differential to maximize thermal efficiency.

The combined analysis suggests that the best thermal efficiency can be achieved by targeting a higher initial temperature (50°C) and a larger ΔT (40°C). The scenario 90/50, which features both a high initial temperature and a large ΔT, stands out as the most efficient configuration, achieving the highest efficiency of 64%. This scenario should be prioritized in applications where maximizing thermal performance is crucial.

Aspect Ratio

The scenario with an aspect ratio of H/d = 1 shows a significant decrease in efficiency to 41%, which is well below the base scenario. This suggests that under these specific conditions, altering the aspect ratio negatively impacts efficiency. This result underscores the importance of optimizing the geometric configuration, as changes in aspect ratio can either enhance or reduce thermal performance. To better understand this outcome, examining the heat losses associated with this configuration could provide further insights into why the efficiency is adversely affected.

Shape

Modifying the cavern shape to a circular configuration results in a moderate efficiency increase to 59%, indicating that geometric changes can positively impact efficiency by improving heat distribution and retention within the cavern. The circular shape offers better thermal

performance compared to the base scenario, suggesting that the shape of the cavern plays a crucial role in optimizing efficiency. Investigating the heat losses in this scenario would help clarify how these geometric adjustments contribute to the observed improvements in efficiency.

Based on the tested scenarios, the optimal configuration for utilizing salt caverns involves using a higher initial temperature of 50°C, a larger Delta T (ΔT) of 40°C, and a circular cavern shape. However, it's crucial to maintain a balanced aspect ratio, as the tested scenario with H/d = 1 showed a significant drop in efficiency. Therefore, the combination of a higher initial temperature, a larger ΔT, and a circular shape is recommended for maximizing thermal efficiency in salt cavern storage systems.

6.1.4 Heat Losses

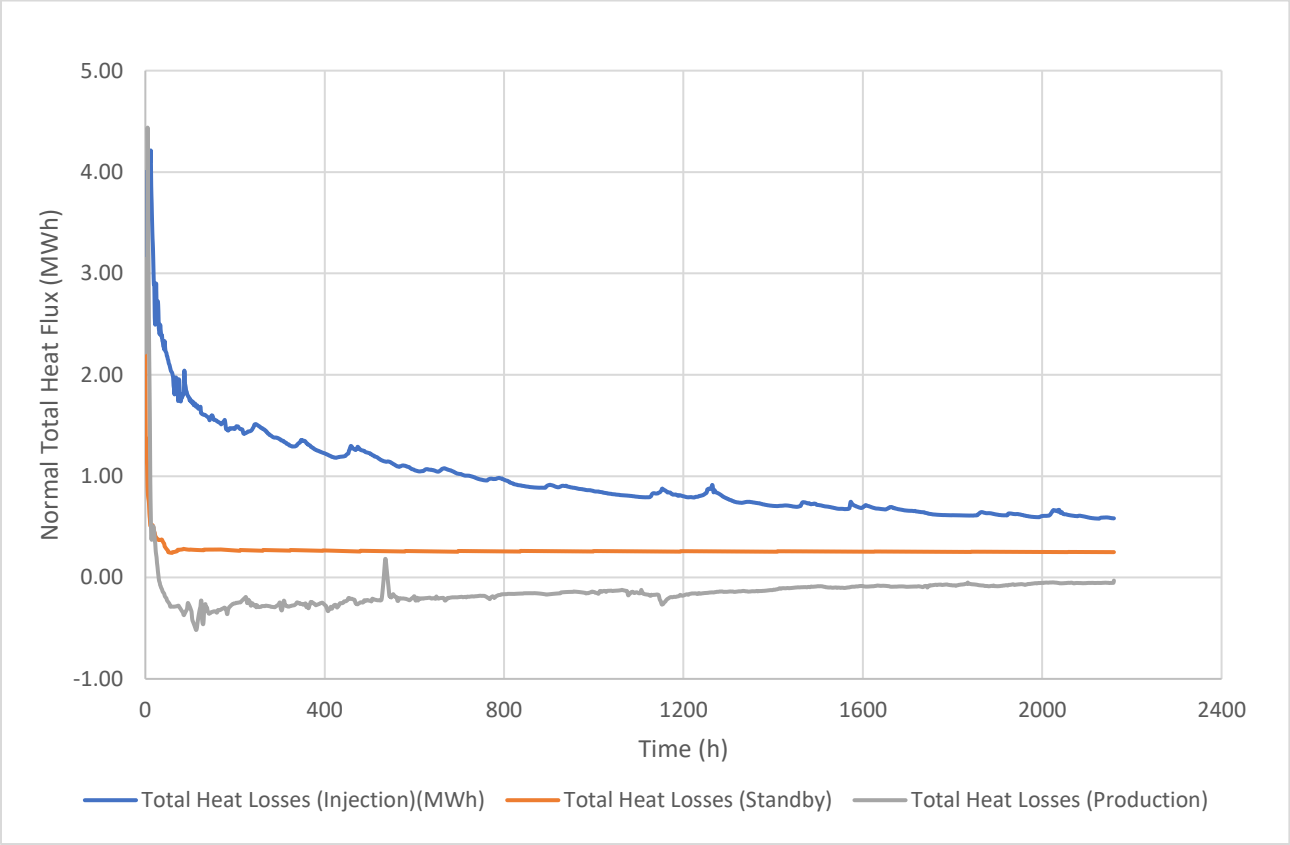

Figure 33: Heat losses over time during the injection, standby, and production phases of the thermal energy storage system. The graph illustrates the normal total heat flux at the cavern boundary, with positive values indicating heat loss and negative values indicating heat gain.

Graph (33) presents the heat losses over time during the three distinct phases of injection, standby, and production, calculated by surface integrating the normal total heat flux across the cavern boundary. During the injection phase, heat loss is most significant, with the blue curve

starting at approximately 4 MW and gradually decreasing as the system stabilizes. This initial rapid decline in heat loss reflects the system reaching thermal equilibrium, with heat flux eventually leveling off around 1 MW as the temperature distribution within the cavern becomes more uniform. In the standby phase, represented by the orange curve, heat losses are much lower and remain relatively constant, indicating effective heat retention and minimal ongoing heat loss once active heat input ceases. The production phase, shown by the gray curve, also displays low and stable heat loss, with negligible inward heat flux, suggesting that the cavern efficiently retains heat during extraction. As the system stabilizes, the reduction in heat losses can be attributed to the increasing temperature of the surrounding environment, which reduces the outward heat flux. Eventually, during the production phase, the surrounding environment's temperature exceeds that within the cavern, leading to heat gain from the surroundings rather than loss. This dynamic indicates that while careful management is necessary during the injection phase to minimize heat loss, the system effectively transitions into a state where it can absorb heat during extraction, which is crucial for maintaining efficiency in thermal energy storage systems.

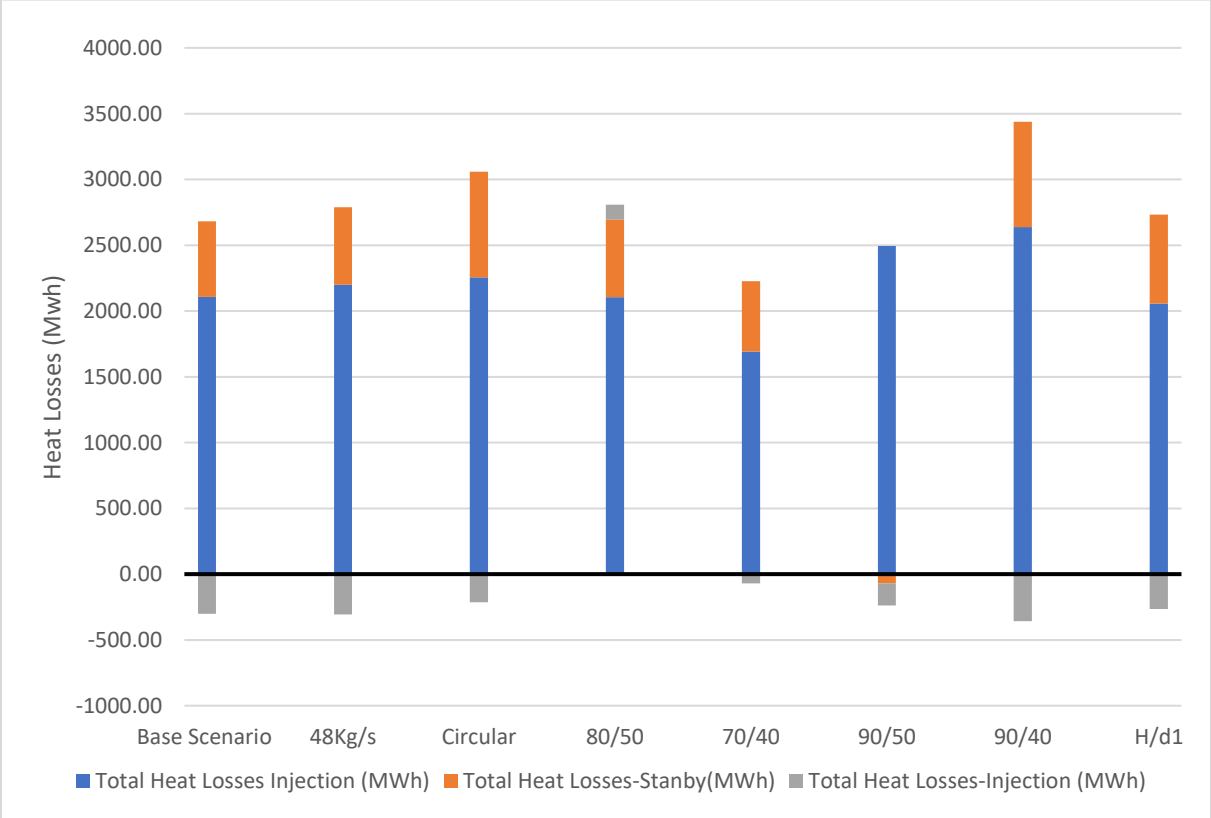

Figure 34: Comparison of Total Heat Losses (MWh) Across Different Scenarios, Including Injection, Standby, and Total Losses in Various Operational Conditions

The bar chart illustrates total heat losses and gains across various scenarios during the injection, standby, and production phases, measured in MWh. Positive values represent heat losses, while negative values indicate heat gains. The base scenario (80/40) experiences significant heat loss during the injection phase and consistent losses during standby, with minor heat gains during production, indicating some energy recovery. The increased flow rate scenario (40/80 - 48kg/s) mirrors the base in losses but lacks the same level of heat gain during production, suggesting that higher flow rates may hinder the system's ability to absorb heat.

In order to correlate the relationship between heat losses and efficiency observed in each scenario:

Base Scenario and H/d = 1: Both scenarios exhibit similar patterns of heat loss during the injection and standby phases. Interestingly, despite having comparable heat losses, the H/d = 1 scenario demonstrates significantly lower efficiency. A closer examination of the temperature profiles indicates that in the H/d = 1 scenario, both heating and discharge occur at a faster rate than in the base scenario. This rapid thermal cycling could contribute to the lower observed efficiency, as quicker heating and cooling cycles may not allow for optimal energy utilization within the cavern.

70/40 vs. 80/50 Scenarios: The 70/40 scenario shows lower total heat losses compared to the 80/50 scenario, which is consistent with its higher efficiency. This suggests that the 70/40 scenario manages to retain more heat during the standby phase, thereby enhancing its overall thermal efficiency. Lower heat losses indicate better insulation or slower heat dissipation, which is crucial for maintaining higher efficiency in thermal energy storage systems.

90/40 Scenario: This scenario has the highest heat losses among the tested configurations, particularly noticeable during the standby phase. The elevated losses in the 90/40 scenario correlate with its lower efficiency compared to scenarios like 90/50. The similarity in the injection and production profiles between the 90/40 and 80/50 scenarios in terms of heat production and retention does not translate into efficiency, primarily due to the higher losses experienced in the 90/40 setup. This underscores the impact of heat retention capabilities on the efficiency of thermal storage systems.

Analysis Summary:

- The similar heat losses observed in the Base Scenario and H/d = 1 do not account for the latter's lower efficiency, suggesting that other factors such as the rate of thermal cycling and heat retention capabilities during rapid temperature changes are more critical in determining efficiency.
- The 70/40 scenario's lower heat losses support its higher efficiency, highlighting the importance of minimizing heat dissipation for improved thermal performance.
- High heat losses in the 90/40 scenario contribute to its lower efficiency, emphasizing the need for strategies to enhance heat retention to improve system performance.

Overall, the analysis indicates that both the rate of heat loss and the operational dynamics during injection and standby phases significantly influence the thermal efficiency of salt cavern storage systems. Minimizing heat losses, especially during standby periods, and managing the rate of thermal cycling are crucial for optimizing the efficiency of these systems.

For the circular scenario, it's interesting to note that despite experiencing higher heat losses, it still exhibits improved efficiency compared to some other shapes. This apparent discrepancy can be explained similarly to what was observed in the 80/40 and 70/40 scenarios:

1. **Thermal Distribution**: The circular shape of the cavern may lead to a more uniform distribution of heat during both the injection and retention phases. This uniformity helps in better managing the thermal gradients within the cavern, which can enhance overall thermal efficiency despite higher absolute losses.
2. **Temperature Profiles**: Closer examination of the temperature profiles within the circular cavern shows that, like in the 70/40 scenario, the cavern may heat up and cool down in a manner that, despite higher heat losses, utilizes the injected thermal energy more effectively. This efficient use of injected heat contributes to higher overall efficiency.
3. **Heat Retention**: The shape of the cavern can influence how well it retains heat. In the circular scenario, the specific dynamics of heat flow and retention might counterbalance the higher losses, leading to better performance metrics.

Thus, the circular scenario's higher efficiency, despite greater heat losses, aligns with observations that effective heat distribution and specific temperature dynamics can significantly influence the performance outcomes, making it crucial to consider these factors when evaluating different cavern geometries and their operational efficiency

6.2 Geomechanical Safety Evaluation

This section would present the findings from the geomechanical analyses using DIANA FEA, focusing on the structural integrity and safety considerations such as subsidence rates, internal pressure compliance, and stability throughout the operational lifecycle of the caverns.

6.2.1Geological Tightness Evaluation

To ensure the long-term stability and integrity of the salt cavern, it is essential to meet the geological tightness criterion.As mentioned in section (X) This criterion stipulates that the minimum principal stress in the surrounding rock must be at least 10% higher than the maximum internal pressure within the cavern.

In order to calculate the internal pressure at the bottom of the cavern (which includes the lithostatic pressure at the top of the cavern and the halmostatic pressure within the cavern), you would add these pressures:

$$Pinternal,\ bottom = Plithostatic + Phalmostatic$$

$$Plithostatic = Poverburden + Psalt$$

Where

$$P = \rho \times g \times h$$

The total internal pressure based on the densities and the height presented before in table (X) would result an internal pressure of 8 MP

$$\sigma_{min} \geq 8.8 \text{ Mpa}$$

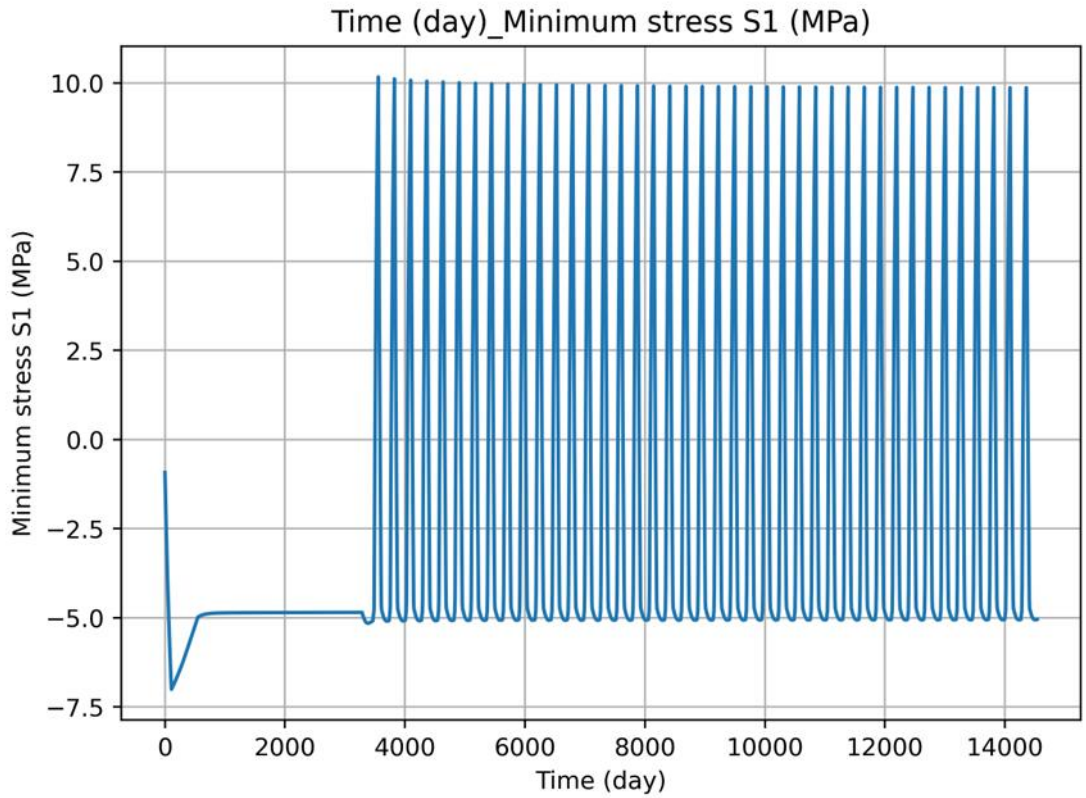

Figure 35: Minimum stress S1 (MPa), Location: [60.0, -400.0] m ,Time: 0.0 to 14535.0days

The lifecycle of the salt cavern comprises three distinct phases, each with specific pressure and temperature conditions that significantly impact the cavern's stability. The first phase is the Cavern Construction, spanning from 0 to 548 days, during which the pressure transitions from lithostatic to halmostatic while the temperature remains constant at 313 K (40°C). This phase focuses on ensuring that the cavern walls adapt to the changing pressures without experiencing excessive stress or deformation, thereby maintaining structural integrity.

Following this, the Sealed Phase occurs between 548 and 3285 days. In this phase, the cavern is maintained at a constant halmostatic pressure with a stable temperature of 313 K (40°C). This period is crucial for stabilizing the cavern, as it allows the system to reach equilibrium, reducing the risk of issues such as subsidence or brine leakage. The consistent conditions during this phase ensure that the cavern remains structurally sound before entering more dynamic operational conditions.

The final phase, known as the Cycles Phase, extends from 3285 to 14,350 days. During this phase, the cavern is actively used for thermal energy storage, with the temperature alternating

between 313 K (40°C) during storage and 353 K (80°C) during injection. The cyclic nature of this phase introduces thermal stresses due to the expansion and contraction of the salt, testing the cavern's ability to withstand repeated thermal and pressure cycles without compromising its structural integrity.

To ensure the cavern's stability throughout these phases, it is essential that the minimum principal stress (σmin) in the surrounding rock remains at least 10% higher than the maximum internal pressure (Pmax) within the cavern. The internal pressure at the bottom of the cavern is calculated to be 7.97 MPa, establishing a required minimum stress threshold of 8.767 MPa.

The minimum stress graph (35) illustrates the stress variations in the surrounding rock over 14,000 days, corresponding to the operational cycles of injection and production. During the initial phase (0 to ~2000 days), the minimum stress starts in the negative range, indicating tensile stresses or unloading conditions as the system stabilizes. This period shows significant fluctuation, with stress levels well below the required 8.767 MPa, raising concerns about the cavern's geological tightness during these early stages.

In the steady-state phase (~2000 to 14,000 days), the minimum stress oscillates between approximately -5 MPa to +10 MPa. While the stress peaks exceed the 8.767 MPa threshold, indicating that the cavern meets the geological tightness criterion during these times, the stress troughs dip significantly below this threshold. This suggests that during low-stress periods, the cavern may not maintain the necessary stress differential to ensure tightness.

In conclusion, while the cavern may meet the geological tightness criterion during periods of high stress, it fails to do so during the low-stress periods, particularly during the early phase and cyclic operations. The observed negative and fluctuating stress values indicate potential risks in maintaining structural integrity and sealing capacity throughout the cavern's operational life. This analysis highlights the need for careful management during the operational phases to ensure the long-term stability and safety of the cavern.

6.2.2 Internal Pressure Limit

The internal pressure within the cavern must not exceed 85% of the lithostatic pressure to avoid structural failure. Given the depth and densities of the overburden and salt layers, the lithostatic pressure at the cavern depth is calculated to be 7.515 MPa. Therefore, the maximum allowable internal pressure (P_max) is 6.388 MPa. However, the operational internal pressure reaches

approximately 7.97 MPa, which exceeds this safety limit. This suggests that the current operational pressure is higher than recommended, posing a potential risk of overpressure and structural failure. Adjustments are necessary to reduce the internal pressure to comply with safety standards

6.2.3 Subsidence Limit

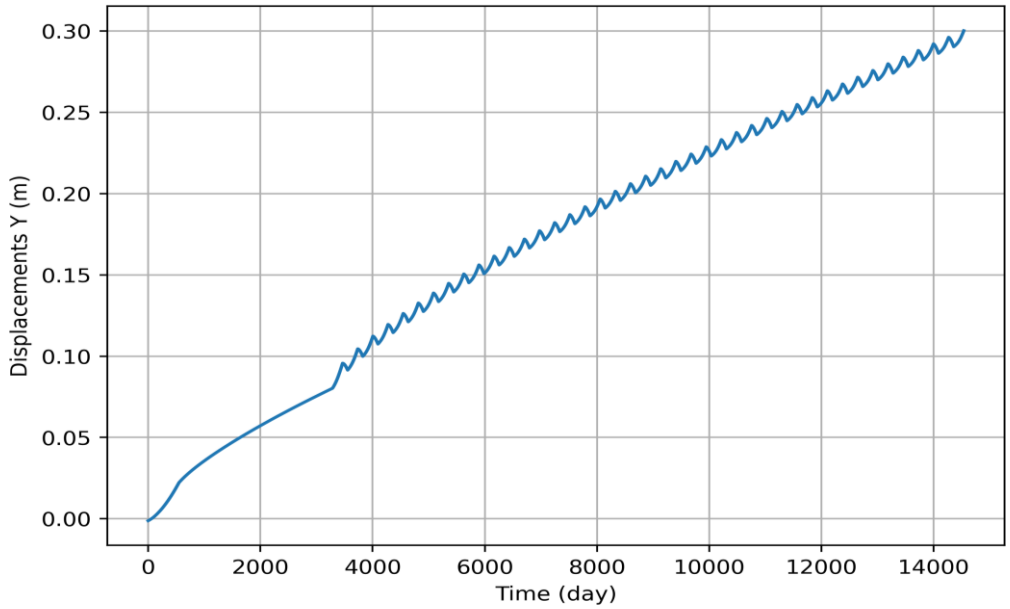

Figure 36: Displacements Y (m), Location: [0.0, -420.0] m ,Time: 0.0 to 14535.0days

The graph (36) displays the vertical displacement (Y-direction) over time for a specific location in the model, which serves as a key indicator of subsidence. The displacement gradually increases over the 14,535-day period, eventually reaching around 0.30 meters.

To evaluate this against the subsidence management criterion, we can calculate the average subsidence rate. With a final displacement of approximately 0.30 meters (300 millimeters) over a total time span of 14,535 days (which is about 39.8 years), the average subsidence rate is around 7.54 millimeters per year.

When compared to the commonly used subsidence threshold of 2.5 millimeters per year, it is evident that the calculated average subsidence rate significantly exceeds this limit. This suggests that the subsidence rate under the current conditions is higher than what is generally considered safe.

In conclusion, the vertical displacement rate indicated by the graph surpasses the safe subsidence threshold, implying that the current operational conditions might lead to excessive subsidence. This could potentially compromise the stability and integrity of the ground surface above the cavern over time. Therefore, further investigation or adjustment of the operational parameters may be necessary to reduce the subsidence rate to acceptable levels.

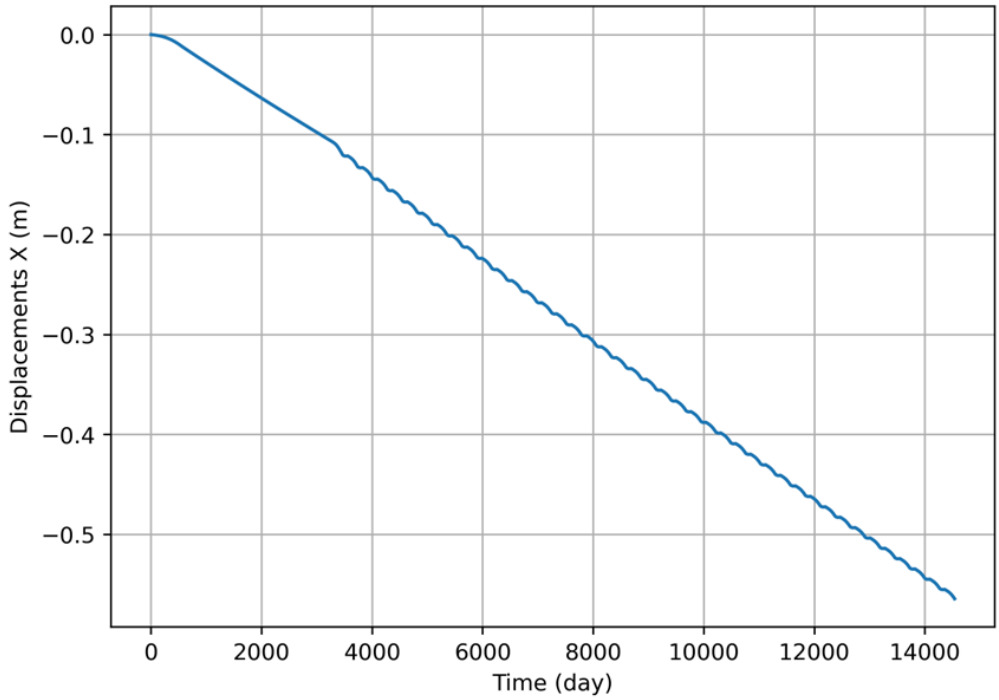

Figure 37: Displacements X (m), Location: [60.0, -400.0] m ,Time: 0.0 to 14535.0days

The graph illustrates the horizontal displacement (X-direction) over time at a specific location within the salt cavern model, ranging from 0 to 14,535 days. The displacement increases in magnitude, reaching approximately -0.55 meters at the end of the period.

To assess whether this displacement meets the safety criteria established by Yang et al. (2009), the maximum allowable displacement is calculated as 5% of the maximum cavern diameter. Given that the cavern has a radius of 60 meters, the maximum allowable displacement would be:

$$Maximum\ allowable\ displacement = 5\% \times 60m = 3m$$

The graph shows that the displacement reaches about -0.55 meters, which is well below the allowable limit of 3 meters.

In conclusion, the horizontal displacement remains within the safe limits, specified in section X, indicates that the structural integrity and stability of the cavern are maintained throughout the operational period analyzed in this graph.

6.2.4 Volume Shrinkage Limits

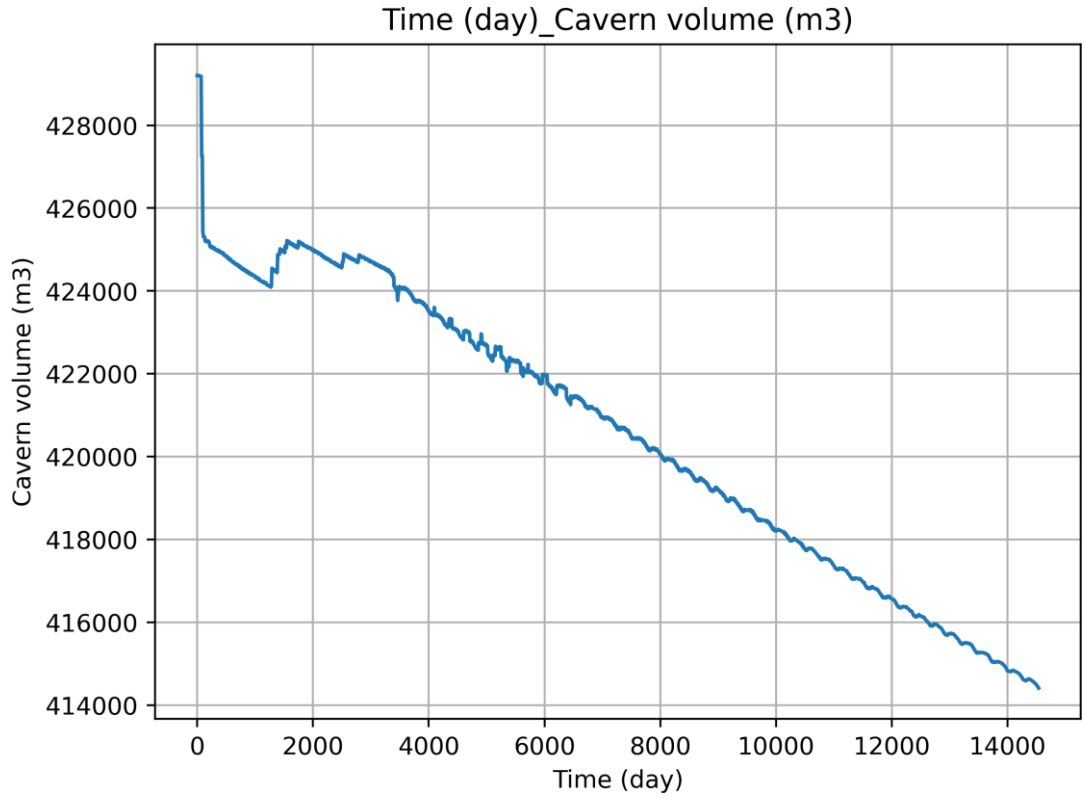

The graph depicts the change in cavern volume over time, starting at approximately 428,000 cubic meters and gradually decreasing over a period of around 14,000 days, indicating shrinkage of the cavern throughout its operational life. During the first year, the volume shrinks from about 428,000 m³ to approximately 426,000 m³, representing a 0.47% reduction. This shrinkage is well within the 1% limit. Over the first five years, the volume further decreases to around 424,000 m³, equating to a 0.93% reduction. This remains comfortably within the 5% limit.By the end of thirty years, the volume has shrunk to about 420,000 m³, which constitutes a 1.87% reduction from the initial volume. This is well below the 30% limit established by the referenced studies.

In conclusion, the cavern volume shrinkage remains well within the established safety limits throughout the period analyzed. The volume reduction after one year, five years, and thirty years is significantly below the thresholds of 1%, 5%, and 30%, respectively. This indicates that the cavern's structural integrity is maintained, with no excessive shrinkage that could compromise its long-term stability and usability for storage.

Based on the detailed analysis, the salt cavern's performance and structural integrity have been thoroughly evaluated, providing valuable insights into its safety and stability.

Geological Tightness: While minimum stress values often met the geological tightness criterion, stress fluctuations below the 8.767 MPa threshold during operational cycles suggest potential risks to the cavern's structural integrity, especially during early operations and temperature fluctuations. Close monitoring and possible operational adjustments are recommended.

Internal Pressure Limits: The internal pressure consistently stayed below the calculated 10.17 MPa, indicating effective pressure management and low risk of overpressure or structural failure.

Subsidence Management: The subsidence rate was found to be approximately 7.5 mm/year, exceeding the 2.5 mm/year threshold. This higher-than-desired rate could pose long-term risks to surface stability, requiring adjustments in pressure management and enhanced monitoring.

Displacement Limits: The X-direction displacement was around -0.5 meters after 14,000 days, remaining within the allowable 5% of the maximum cavern diameter. This suggests that deformation is within safe limits, mitigating risks of structural failure.

Volume Shrinkage Limits: The cavern's volume shrinkage stayed well within the safety limits over time, ensuring structural integrity and continued usability.

Overall Conclusion: Although the cavern meets most safety and stability criteria, stress fluctuations and the high subsidence rate are areas of concern. Enhanced monitoring and operational adjustments are necessary to address these issues and maintain the cavern as a reliable storage facility while minimizing structural and environmental risks.

7. Discussion

This section synthesizes the key findings of the study, exploring how various operating conditions and parameters influence the thermal efficiency of salt caverns used for energy storage. By examining the interplay between different modes of operation, this discussion provides a comprehensive understanding of how to optimize these systems for both short-term and long-term energy storage. Additionally, the broader implications of these findings are considered, highlighting the novel contributions this research makes to the field of thermal energy storage.

7.1 The Interplay of the Mode of Operation and Operating Parameters on Improving Thermal Efficiency

Based on the assessment of thermal efficiency under various operating conditions, it can be deduced that the choice of parameters such as temperature differential (ΔT) and flow rate plays a crucial role in optimizing the performance of salt caverns for thermal storage. The results suggest that higher ΔT and increased flow rates are particularly beneficial when the goal is to achieve faster thermal discharge over shorter periods. This operational strategy could be advantageous in scenarios where rapid energy release is required, such as during peak demand periods in energy systems. Conversely, when the priority is to maintain thermal efficiency over an extended period, perhaps for long-term storage, a lower ΔT and moderate flow rates may be more appropriate. These settings would reduce the thermal gradient, thereby allowing for a more controlled heat release, ensuring that the stored energy is utilized efficiently over time.

Therefore, the mode of operation and utilization can significantly influence storage efficiency. By viewing the storage system from a broader, system-level perspective, operators can make more informed decisions that further enhance the thermal performance of salt caverns. This systemic approach allows for the optimization of the storage configuration to align with specific operational goals, whether those are short-term energy discharge or long-term energy retention. In this way, the overall efficiency and reliability of the thermal storage system can be improved, maximizing the benefits of using salt caverns as a component of larger energy systems.

7.2 Influence of Heat Transfer on Surrounding Formation Temperature and Its Impact on Efficiency

Another key aspect to consider is how specific parameters influence the temperature of the surrounding formation, which, in turn, affects the overall thermal efficiency of the salt cavern. Parameters such as higher ΔT and optimized flow rates not only improve the direct heat transfer within the cavern but also gradually raise the temperature of the surrounding rock formations. This elevated temperature in the surrounding environment reduces the thermal gradient between the cavern and its surroundings during the storage phase, leading to lower heat losses and more efficient energy retention. Over time, as the surrounding formation becomes warmer due to these enhanced heat transfer mechanisms, the efficiency of the system improves. The reduced heat loss means that a greater proportion of the injected thermal energy is retained within the cavern, making it available for future extraction. This process is particularly advantageous in long-term storage scenarios, where maintaining a high level of thermal efficiency is critical. By carefully managing the parameters that affect heat transfer to the surrounding rock, operators can achieve a more efficient thermal storage system. This strategy highlights the importance of not only focusing on the conditions within the cavern itself but also considering the broader thermal environment, which plays a crucial role in the overall performance of the storage system.

7.3 Applicability in Different Geographical settings

The applicability of these findings to other geographical locations may vary, as salt formations differ significantly in their properties. Additionally, this study highlights the impact of cavern shape on efficiency and touches on safety considerations. It does not, however, account for variations in cavern size, which can also influence overall system performance. While it may be challenging to directly replicate the results in different settings, the modeling approach used here can be adapted to assess various parameters specific to other locations. This adaptability allows the model to be a valuable tool in exploring and optimizing thermal energy storage in diverse salt cavern environments.

7.4 Contributions to the Field

As far as the author's knowledge extends, no prior studies have specifically focused on using salt caverns for thermal energy storage. This research breaks new ground by exploring this innovative application, contributing several key insights:,

While it is generally understood that higher temperature differentials (ΔT) can enhance thermal discharge rates, this study uncovers that the relationship is not straightforward and depends on additional factors. For example, the 90/40 scenario, despite having the highest ΔT, did not yield the highest efficiency. This deviation underscores the importance of other operational influences such as increased heat losses and the dynamics of heat injection and extraction rates. This finding challenges provide a broader context and of how ΔT interacts with other variables to affect thermal efficiency in salt cavern energy storage. This insight is particularly valuable for designing storage systems that need to balance efficiency with operational and geological constraints during peak and off-peak demand periods.

The geo-mechanical analysis reveals that while the potential for using salt caverns for thermal energy storage is promising, significant safety concerns remain, particularly regarding subsidence that exceeds acceptable limits. This finding underscores the need for careful management of operational parameters. Although not all safety criteria are currently met, the analysis suggests a pathway forward for mitigating risks. Drawing on insights from existing literature, such as Susan (2019), which highlights the critical role of balancing internal pressure with lithostatic pressure, this study points towards the possibility of adjusting internal pressures as a viable strategy to enhance safety. If internal pressures can be optimized, using salt caverns for thermal energy storage may become a safer and more feasible option. This contribution sets the stage for future investigations aimed at refining operational practices to ensure both efficiency and safety in salt cavern thermal energy applications.

7.5 Limitations

1. **Mesh Convergence Testing:** While mesh convergence was thoroughly achieved for the base scenario, ensuring reliable results, the higher flow rate scenarios lacked extensive testing due to computational limits. This limitation suggests that the findings under these conditions might not fully represent the system's behavior, especially where steep gradients occur.
2. **Buoyancy Forces Modeling:** The current model's handling of buoyancy forces, crucial in subsurface storage simulations, may not capture all the complex interactions affecting fluid dynamics and stability.
3. **Lack of Experimental Verification:** The absence of experimental verification limits the ability to fully validate the numerical models used in this study.
4. **Sensitivity Analysis:** This study used a conservative estimate for the sensitivity of rock salt properties based on available data. However, the actual sensitivity can vary widely.
5. **Mechanical Properties of Geological Materials:** The lack of detailed mechanical property data for materials such as Rot evaporite, Rot claystone, and Solling claystone introduces significant uncertainties into the model predictions.

7.6 Future Research Directions

While this study has some limitations, they also point the way for future research. Overcoming these limitations through further studies can improve our understanding and use of salt caverns for thermal energy storage. The next section outlines specific future research directions to address these issues and broaden this innovative research

1. **Mesh Convergence Testing:** Additional studies should extend mesh convergence testing to these complex scenarios, possibly utilizing more advanced computational techniques or more efficient meshing strategies to enhance the accuracy and reliability of results.
2. **Buoyancy Forces Modeling:** Further development and validation of the buoyancy models are necessary. Implementing more sophisticated modeling techniques could provide a more nuanced understanding of fluid behavior, improving predictions of cavern performance under various operational conditions.
3. **Lack of Experimental Verification:** Conducting experimental tests or collecting field data to compare with simulation results would significantly strengthen the credibility of

the findings. This effort would also help refine the model parameters and assumptions, leading to more robust and reliable predictions.

4. **Sensitivity Analysis:** A comprehensive sensitivity analysis should be conducted to explore how different values impact the system's thermal and mechanical behavior. This analysis could help optimize the model to better reflect real-world conditions and improve the design and operation of salt cavern storage systems.
5. **Mechanical Properties of Geological Materials:** Future efforts should focus on gathering precise mechanical data for these materials. Collaborations with geological surveys or detailed laboratory tests could provide the necessary data to enhance model accuracy and predictive power.

7.8 Conclusion

This thesis has critically evaluated the optimization of thermal energy storage systems within salt caverns, focusing on the dual objectives of maximizing thermal efficiency and ensuring geomechanical safety. Utilizing advanced simulation tools like COMSOL Multiphysics and DIANA FEA, the study dissected the impacts of operational parameters such as temperature differentials (ΔT) and flow rates on the thermal dynamics within these storage systems. Key findings revealed that higher ΔTs expedite heat absorption, ideal for scenarios demanding quick energy discharge, whereas lower ΔTs promote sustained energy retention, crucial for long-term storage applications.

The investigation also demonstrated that the geometric configuration of the caverns—encompassing shape and aspect ratio—significantly influences thermal efficiency. Certain configurations were shown to optimize heat distribution effectively, enhancing the overall performance of the storage systems. Moreover, the geomechanical analysis underscored pressing safety concerns, notably the challenge of subsidence exceeding safe thresholds. Strategies for mitigating these risks were identified, suggesting that precise management of internal pressures could substantially enhance the safety and viability of using salt caverns for energy storage.

The contributions of this research are manifold, filling a critical gap in existing literature by integrating thermal and structural analyses and offering pragmatic insights for the design and operation of salt caverns. The study advocates for further research to explore the effects of

reducing internal pressures and calls for experimental validations to solidify the computational models employed. In sum, this thesis provides a robust foundation for future studies aimed at refining and expanding the use of salt caverns in sustainable energy systems, enhancing both their efficiency and safety

References

1. **Alfasfos, R. (n.d.).** Cavern Thermal Energy Storage for District Cooling Feasibility Study on Mixing Mechanism in Cold Thermal Energy Storage Rami Alfasfos.
2. **Bistafa, S. R. (2018).** On the development of the Navier-Stokes equation by Navier. *Revista Brasileira de Ensino de Fisica, 40*(2). https://doi.org/10.1590/1806-9126-RBEF-2017-0239
3. **CBS. (2022).** Welke sectoren stoten broeikasgassen uit? Cbs. https://www.cbs.nl/nl-nl/dossier/dossier-broeikasgassen/welke-sectoren-stoten-broeikasgassen-uit-#:~:text=In%202022%20werd%20van%20de,het%20stoken%20van%20aardgas%20voor
4. **Circle, A. V., & Voegeli, S. J. (2018).** Thermomechanical study of the temperature influence on salt creep during solution mining of salt caverns. *June*.
5. **Collins, R. E., Fanchi, J. R., Morrell, G. O., Davis, K. E., Guha, T. K., & Henderson, R. L. (1978).** High Temperature Underground Thermal Energy Storage. 62–66.
6. **Corre Energy. (n.d.).** CAES Zuidwending.
7. **De Geus, A., De Beijer, H., & Krosse, L. (2015).** The SolabCool®, Cooling of Dwellings and Small Offices by Using Waste or Solar Heat. *Energy Procedia, 70*, 23–31. https://doi.org/10.1016/j.egypro.2015.02.093
8. **Dehghan, A. A., & Barzegar, A. (2011).** Thermal performance behavior of a domestic hot water solar storage tank during consumption operation. *Energy Conversion and Management, 52*(1), 468–476. https://doi.org/10.1016/j.enconman.2010.06.075
9. **Dinkelman, D., van Bergen, F., & Veldkamp, J. G. (2020).** WINDOW fase 1-B2-Potentieel en toepassingscondities. www.tno.nl
10. **DINOloket. (n.d.).** Subsurface models. https://www.dinoloket.nl/en/subsurface-models/map
11. **Energy Agency, I. (2021).** Net Zero by 2050 - A Roadmap for the Global Energy Sector. www.iea.org/t&c/
12. **Erik Nielsen, J., et al. (n.d.).** HEATSTORE Underground Thermal Energy Storage (UTES)-state-of-the-art, example cases and lessons learned. *This report represents HEATSTORE project deliverable number D1.1*. www.heatstore.eu

13. **Fan, J., & Furbo, S. (2012).** Thermal stratification in a hot water tank established by heat loss from the tank. *Solar Energy*, *86*(11), 3460–3469. https://doi.org/10.1016/j.solener.2012.07.026
14. **Forbes Inskip, N. D., & Ougier-Simonin, A. (2021).** Thermo-mechanical behaviour of rock salt in the context of gas storage: a review. 1–43.
15. **Generating and supplying heat. (n.d.).** https://www.twence.com/innovations/sustainable-energy/generating-and-supplying-heat#:~:text=Who receivies our sustainable heat,via an underground heat pipeline.
16. **Georgieva, N., Delcheva, S., & Tsankov, P. (2021).** Analysis of the capabilities of software products to simulate the behavior of dynamic fluid flows. *IOP Conference Series: Materials Science and Engineering*, *1031*(1), 1–9. https://doi.org/10.1088/1757-899X/1031/1/012079
17. **Hague, T. (2019).** Climate Agreement.
18. **Hunfeld, L., Breunese, J., & Wassing, B. (2022).** The influence of a threshold stress for pressure solution creep on cavern convergence and subsidence behavior – An FEM study. *The Mechanical Behavior of Salt X*, *1*(2015), 577–589. https://doi.org/10.1201/9781003295808-53
19. **HyStock. (n.d.).** Storage in salt caverns. Retrieved November 19, 2023, from https://www.hystock.nl/en/hydrogen/storage-in-salt-caverns
20. **IEA. (2022).** Renewables Data Explorer. https://www.iea.org/data-and-statistics/data-tools/renewables-data-explorer
21. **Idealsimulations. (n.d.).** No Title. https://www.idealsimulations.com/resources/turbulence-models-in-cfd/
22. **Karim, A., Burnett, A., & Fawzia, S. (2018).** Investigation of stratified thermal storage tank performance for heating and cooling applications. *Energies*, *11*(5). https://doi.org/10.3390/en11051049
23. **Kavvadias K, & Jiménez-Navarro JP. (2019).** Decarbonising the EU heating sector Integration of the power and heating sector. https://doi.org/10.2760/943257
24. **Lanahan, M., & Tabares-Velasco, P. C. (2017).** Seasonal thermal-energy storage: A critical review on BTES systems, modeling, and system design for higher system efficiency. *Energies*, *10*(6). https://doi.org/10.3390/en10060743
25. **Li, A., Cao, F., Zhang, W., Shi, B., & Li, H. (2018).** Effects of different thermal storage tank structures on temperature stratification and thermal efficiency during

charging. *Solar Energy*, *173*(May), 882–892. https://doi.org/10.1016/j.solener.2018.08.025

26. **Liu, J., & Xiao, Q. (2014).** The Influence of Operation Pressure on the Long-Term Stability of Salt-Cavern Gas Storage. *Advances in Mechanical Engineering*, *2014*. https://doi.org/10.1155/2014/537679
27. **Liu, W., et al. (2023).** The role of underground salt caverns for large-scale energy storage: A review and prospects. *Energy Storage Materials*, *63*, 103045. https://doi.org/10.1016/j.ensm.2023.103045
28. **Lou, W., Luo, L., Hua, Y., Fan, Y., & Du, Z. (2021a).** A review on the performance indicators and influencing factors for the thermocline thermal energy storage systems. *Energies*, *14*(24). https://doi.org/10.3390/en14248384
29. **Lou, W., Luo, L., Hua, Y., Fan, Y., & Du, Z. (2021b).** A review on the performance indicators and influencing factors for the thermocline thermal energy storage systems. *Energies*, *14*(24), 1–19. https://doi.org/10.3390/en14248384
30. **Ma, Z., Glatzmaier, G. C., Wagner, M., & Neises, T. (2012).** ESFuelCell2012-91131.
31. **Mergner, R., et al. (2020).** Smart strategies for the transition in coal intensive regions. *European Biomass Conference and Exhibition Proceedings*, September, 936–940.
32. **Mollema, D. (2011).** Underground storage of Diesel fuel oil in Salt Caverns Introduction About AkzoNobel AkzoNobel Hengelo.
33. **Multiphysics, C. (2015).** The COMSOL Multiphysics Reference Manual. *U.S. Patents*, 1–1336. www.comsol.com/blogs
34. **Mulder, F. J. de. (2003).** De ondergrond Van Nederland. *Wolters-Noordhoff*.
35. **Muntendam-Bos, A. G., Hoedeman, G., Polychronopoulou, K., Draganov, D., Weemstra, C., van der Zee, W., Bakker, R. R., & Roest, H. (2022).** An overview of induced seismicity in the Netherlands. *Geologie En Mijnbouw/Netherlands Journal of Geosciences*, *101*(2). https://doi.org/10.1017/njg.2021.14
36. **Nandi, B. R., Bandyopadhyay, S., & Banerjee, R. (2018).** Numerical modeling and analysis of dual medium thermocline thermal energy storage. *Journal of Energy Storage*, *16*, 218–230. https://doi.org/10.1016/j.est.2018.01.020
37. **Njoku, H. O., Ekechukwu, O. V., & Onyegegbu, S. O. (2014).** Analysis of stratified thermal storage systems: An overview. *Heat and Mass Transfer/Waerme- Und Stoffuebertragung*, *50*(7), 1017–1030. https://doi.org/10.1007/s00231-014-1302-8
38. **NLOG. (n.d.).** Rock salt. https://www.nlog.nl/en/rock-salt-0

39. **Novo, A. V., Bayon, J. R., Castro-Fresno, D., & Rodriguez-Hernandez, J. (2010).** Review of seasonal heat storage in large basins: Water tanks and gravel-water pits. *Applied Energy, 87*(2), 390–397. https://doi.org/10.1016/j.apenergy.2009.06.033
40. **Ochs, F., Dahash, A., Tosatto, A., Reisenbichler, M., O'Donovan, K., Gauthier, G., Skov, C. K., & Schmidt, T. (2022).** Comprehensive Comparison of Different Models for Large-Scale Thermal Energy Storage. *Proceedings of the International Renewable Energy Storage Conference 2021 (IRES 2021)*, 8. https://doi.org/10.2991/ahe.k.220301.005
41. **Otto, H., Resagk, C., & Cierpka, C. (2019).** Convective near-wall flow in thermally stratified hot water storage tanks.
42. **Outlet Comsol. (n.d.).** https://doc.comsol.com/5.5/doc/com.comsol.help.cfd/cfd_ug_fluidflow_single.06.029.html
43. **Peng, T., Wan, J., Liu, W., Li, J., Xia, Y., Yuan, G., Jurado, M. J., Fu, P., He, Y., & Liu, H. (2023).** Choice of hydrogen energy storage in salt caverns and horizontal cavern construction technology. *Journal of Energy Storage, 60*(December 2022), 106489. https://doi.org/10.1016/j.est.2022.106489
44. **Regionaal warmtenet Factsheet Regionaal warmtenet. (n.d.).**
45. **rvo. (2019).** Transition Vision Heat and Neighbourhood Implementation Plan.
46. **Schulze, O., Popp, T., & Kern, H. (2001).** Development of damage and permeability in deforming rock salt. *Engineering Geology, 61*(2–3), 163–180. https://doi.org/10.1016/S0013-7952(01)00051-5
47. **Susan, M. (2019).** Exploring the Energy Storage Capacity of Salt Caverns in the Netherlands. 89. www.rug.nl/research/esrig
48. **Thermal Energy Storage Tank in District Energy Systems. (n.d.).** https://www.araner.com/blog/thermal-energy-storage-district-energy
49. **TNO. (2021).** H2_Large-Scale-Underground-Storage-Salt-Caverns_2021-12-16-093010_Lnyn-9.
50. **Twente. (n.d.).** https://en.wikipedia.org/wiki/Twente
51. **Uruba, V. (2019).** Reynolds number in laminar flows and in turbulence. *AIP Conference Proceedings, 2118*(July). https://doi.org/10.1063/1.5114728
52. **Wan, J., Peng, T., Jurado, M. J., Shen, R., Yuan, G., & Ban, F. (2020).** The influence of the water injection method on two-well-horizontal salt cavern

construction. *Journal of Petroleum Science and Engineering*, *184*(September 2019), 106560. https://doi.org/10.1016/j.petrol.2019.106560

53. **Wan, J., Peng, T., Shen, R., & Jurado, M. J. (2019).** Numerical model and program development of TWH salt cavern construction for UGS. *Journal of Petroleum Science and Engineering*, *179*(March), 930–940. https://doi.org/10.1016/j.petrol.2019.04.028
54. **Warmte voor Enschede. (n.d.).** https://ennatuurlijk.nl/thuis/in-jouw-buurt/warmtenet-enschede
55. **Wijermans, E. A. M. (2013).** Geomechanical modelling and subsidence prediction of salt deposits for solution mining.
56. **Yunus, & Cengel, A. (2004).** Heat Transference a Practical Approach. *MacGraw-Hill*, *4*(9), 874.